

AD-A094 186

SCIENCE APPLICATIONS INC MCLEAN VA  
RADIATION FROM HIGH TEMPERATURE PLASMAS. (U)  
SEP 80 J APRUZESE, E KANE, P VITELLO

UNCLASSIFIED

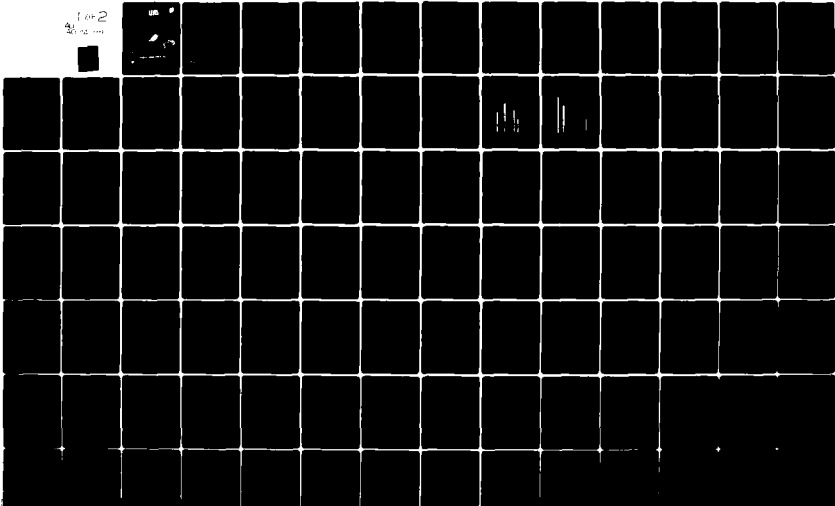
SAI-81-239-W/A

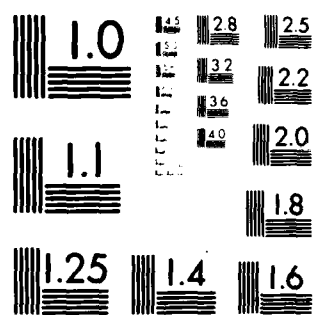
F/G 20/9

N00173-79-C-0448

NL

for 2





MICROCOPY RESOLUTION TEST CHART  
NATIONAL BUREAU OF STANDARDS

AD A094186

2

RADIATION FROM HIGH TEMPERATURE PLASMAS

FINAL REPORT

SAI-81-239-WA



DISTRIBUTION STATEMENT A

Approved for public release;  
Distribution Unlimited



ATLANTA • ANN ARBOR • BOSTON • CHICAGO • CLEVELAND • DENVER • HUNTSVILLE • LA JOLLA  
LITTLE ROCK • LOS ANGELES • SAN FRANCISCO • SANTA BARBARA • TUCSON • WASHINGTON

RADIATION FROM HIGH TEMPERATURE PLASMAS

FINAL REPORT

SAI-81-239-WA

9 September 1980

Submitted to:

Plasma Physics Division  
Naval Research Laboratory  
Washington, D.C. 20375

Prepared Under:

Contract #N00173-79-C-0448

Prepared by:

John Apruzese, Edward Kane, Peter Vitello,  
Dwight Duston and Adam Drobot

SCIENCE APPLICATIONS, INCORPORATED

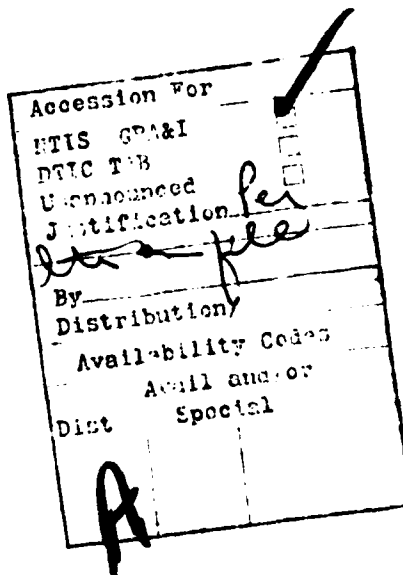
1710 Goodridge Drive, P.O. Box 1303, McLean, Virginia 22102

REPORT DOCUMENTATION PAGE		READ INSTRUCTIONS BEFORE COMPLETING FORM
1. REPORT NUMBER	2. GOVT ACCESSION NO.	3. RECIPIENT'S CATALOG NUMBER
4. TITLE (and Subtitle)		5. TYPE OF REPORT & PERIOD COVERED
RADIATION FROM HIGH TEMPERATURE PLASMAS		Final Report 26 Jun 79 - 26 Aug 80
6. PERFORMING ORG. REPORT NUMBER		
7. AUTHOR(s)	8. CONTRACT OR GRANT NUMBER(s)	
John Apruzese, Edward Kane, Peter Vitello & Dwight Duson <del>and</del> Adam Drobot	(13) N00173-79-C-0448	
9. PERFORMING ORGANIZATION NAME AND ADDRESS	10. PROGRAM ELEMENT, PROJECT, TASK AREA & WORK UNIT NUMBERS	
	(12) 157	
11. CONTROLLING OFFICE NAME AND ADDRESS	12. REPORT DATE	
(14) SAI I-81-131-W/A	(11) 9 September 1980	
14. MONITORING AGENCY NAME & ADDRESS (if different from Controlling Office)	15. SECURITY CLASS. (of this report)	
	Unclassified	
16. DISTRIBUTION STATEMENT (of this Report)	18a. DECLASSIFICATION/DOWNGRADING SCHEDULE	
<div style="border: 1px solid black; padding: 5px; text-align: center;"> <b>DISTRIBUTION STATEMENT A</b>            Approved for public release;            Distribution Unlimited         </div>		
17. DISTRIBUTION STATEMENT (of the abstract entered in Block 20, if different from Report)		
18. SUPPLEMENTARY NOTES		
19. KEY WORDS (Continue on reverse side if necessary and identify by block number)		
exploding wires, gas puffs, line radiation, continuum radiation, radiation hydrodynamics, imploding discharge, ionization model, spectroscopic diagnosis		
20. ABSTRACT (Continue on reverse side if necessary and identify by block number)		
This report presents analyses of the detailed physical processes of importance in imploding wire and gas puff plasmas. Accurate treatment of the atomic physics and radiation transport underlying the x-ray exchange and output is emphasized. Feedback coupling of radiation and hydrodynamics are examined through use of coupled radiation hydrodynamics codes and analysis of motional Doppler broadening of line radiation.		

402407

TABLE OF CONTENTS

<u>SECTION</u>	<u>PAGE</u>
I. TECHNICAL DISCUSSION . . . . .	1
1. Introduction . . . . .	1
2. Ionization, Excitation and Radiation Transport Modeling . . . . .	3
3. Radiation Hydrodynamics Modeling . . . . .	17
II. REFERENCES . . . . .	30
APPENDIX A - Self-Absorption of Heliumlike Satellite Lines in High-Density Fusion Plasmas	
APPENDIX B - Line Emission from Hot, Dense Aluminum Plasmas	
APPENDIX C - Soft X-Ray and XUV Radiation from High Density Aluminum Plasmas	
APPENDIX D - Correspondence with Maxwell Laboratories	
APPENDIX E - Direct Solution of the Equation of Transfer Using Frequency- and Angle-Averaged Photon Escape Probabilities, with Application to a Multistage, Multilevel Aluminum Plasma	



## I. TECHNICAL DISCUSSION

### 1. Introduction

During the performance period of the contract reflected by this final report (26 June 1979 to 26 August 1980) SAI personnel addressed two broad areas of importance in understanding radiation from high temperature plasmas.

The first area of investigation is the detailed atomic physics and radiation transport which determines the radiating efficiency of a plasma. To accurately compute or predict such radiation, it is clear that the fundamental rates of emission from all the significant energy levels as well as the photons' probability of escape from the plasma must be known. During the performance period, SAI's efforts were concentrated on: 1) adding additional and necessary (as shown by experimental spectra) detail to the energy level models of various radiating elements and mixtures of elements 2) Obtaining more computationally efficient techniques to calculate the probability that a photon escapes the plasma without reabsorption once emitted. The results of these efforts are detailed in the next section and in the appendices.

The second, equally important area of technical activity which SAI was engaged in is the development of hydrodynamics models which realistically take into account the feedback between plasma motion and plasma radiation. When a plasma

is compressed, the resulting heating obviously increases the plasma's resistance to further compression. However, radiative cooling processes - via x-rays for a high temperature plasma - will mitigate this effect. Just how strong the mitigating effect is will determine in large measure the evolution of the plasma and thus its radiative response to higher power generation. Progress made by SAI in understanding this crucial problem is detailed in Section 3.

## 2. Ionization, Excitation, and Radiation Transport Modeling

### a) Spectroscopy and Atomic Physics

The excitation, ionization, and radiation physics of a dense, high temperature plasma is of importance for two fundamental reasons. First, the emitted radiation alters the energetics and thus influences the evolution of the plasma. Second, ratios of spectroscopically detected lines are a valuable tool for diagnosing plasma temperature and density. Appendix A, "Self-absorption of heliumlike satellite lines in high density fusion plasmas"<sup>(1)</sup> details studies of the density dependence of argon, neon and aluminum satellite lines in two-electron (heliumlike) ions taking into account the temperature and opacity variation. Appendix B<sup>(2)</sup>, "Line emission from hot, dense aluminum plasmas" focuses on the behavior of K-shell x-ray lines in aluminum as diagnostic indicators of the plasma temperature and density.

In many cases, most of the radiative output of high temperature aluminum plasmas appears as softer x-rays from the L-shell. Appendix C, "Soft x-ray and XUV radiation from high density aluminum plasmas" describes and quantifies the radiative output of aluminum cylinders (imploded wires) as a function of electron temperature, ion density, and opacity (related to radius) over a wide energy range, for the free-bound continuum as well as lines. A multicell escape probability model was

used to transport both lines and the continuum. This appendix contains numerous predictions of experimental spectra of cylindrically symmetric imploded wire arrays.

One result of SAI's effort during the performance period was a prediction that boron, radiating optimally, is not as efficient a radiator as aluminum radiating optimally. Appendix D contains the text of a letter to the spectroscopy group at Maxwell Laboratories, Inc. detailing this calculation and its implications for experimenters.

b) Radiation Transport Modeling

The work of the performance period was aimed at the achievement of primary objectives of direct relevance to wire and Baccarat goals. First, to develop a quantitative analysis of the effects of plasma motion on escape of line radiation from exploded-wire plasmas. Second, to develop a capability to treat plasma mixtures, and thus provide analyses of the effect of one plasma's radiation on another plasma. The final objective was to continue the synthesis of previous work on the exact transfer equation on the one hand and on probabilistic photon escape on the other. The purpose of this third effort was to enable exact calculations to be performed economically on the myraids of spectral lines which are observed to emanate from exploded-wire plasmas. This would enable more accurate and physically realistic simulations of how closely line radiation may be expected to approach black-body values.

These objectives were accomplished, and the separate sections below set out in detail the methods used and results obtained.

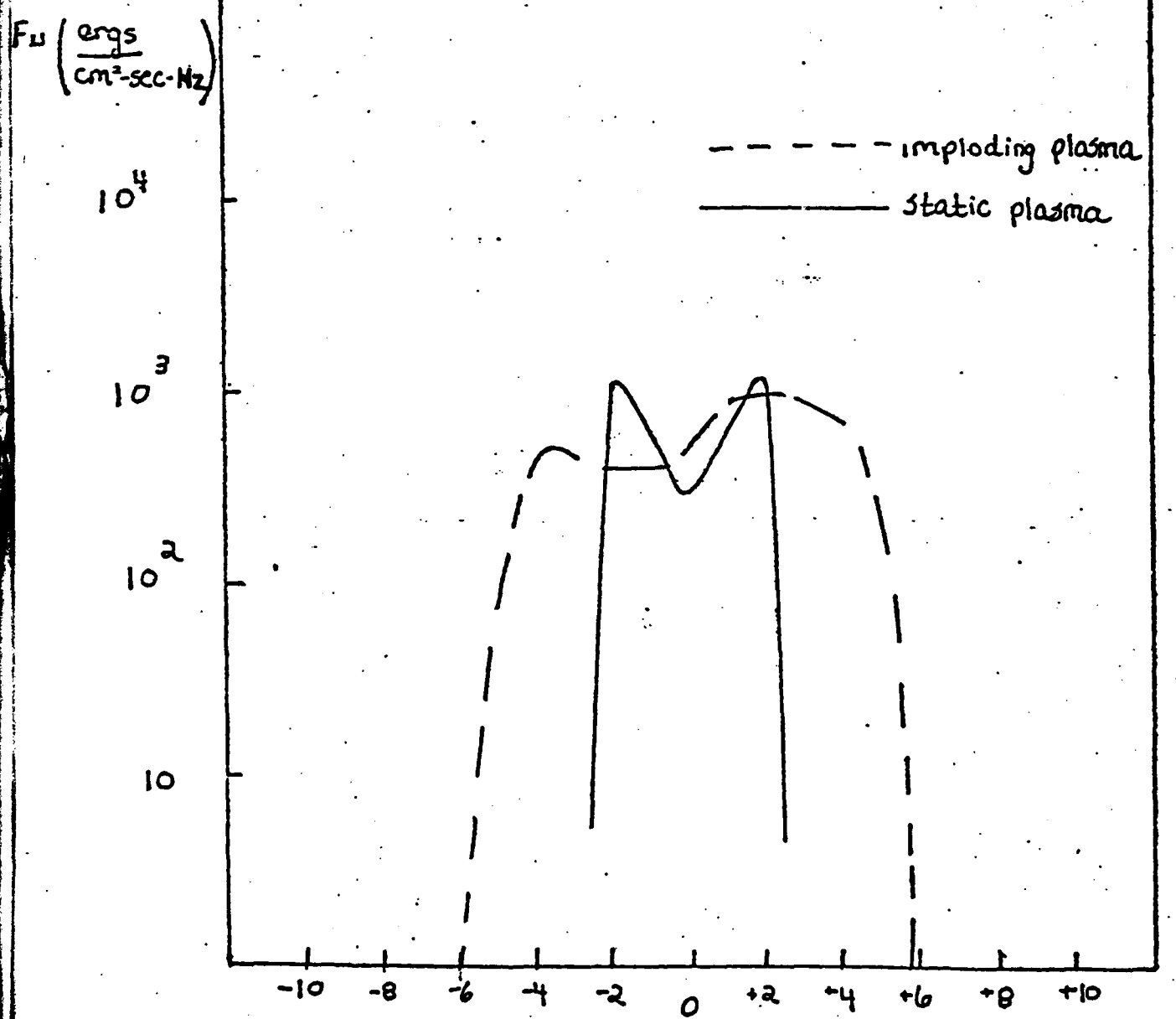
i. Effects of Plasma Motion on Yield and Diagnostics

Since plasmas in general can be characterized by both expanding and compressing regions, it was essential that algorithms developed to treat the effects of motion on radiative output be capable of solving the transfer equation for such non-monotonic velocity fields. The result of the effort was that a computer code containing such an algorithm was written and successfully benchmarked against previously published line profile results of Kunasz and Hummer<sup>(3)</sup>. The set of subroutines which compute the motional broadening effects have been interfaced with our existing large multi-ionization radiative transfer model.

The fundamental physical effect of line broadening by plasma mass motions is that the line photons are more easily able to escape the plasma because they are shifted away from local line center, where the absorption is highest. Thus, an optically thick plasma is turned in the direction of being an optically thin one. This affects the emitted power of an exploded-wire plasma in a positive direction - increasing the power. Some photons which would be bottled up near line center and quenched in a static plasma will instead escape and thus increase the yield.

To gauge the effect of plasma implosion on line radiation we select one of the strongest single lines emitted in typical exploded-wire plasmas, the helium-like  $1s^2 - 1s2p^1P$  line. An inward-directed velocity profile  $V(z) = V_0 z/z_0$  has been chosen, where  $V_0 = 1.3 \times 10^7$  cm/sec,  $z_0$  = plasma half-width (750 microns), and the temperature and density are typical of a wire plasma (600 eV,  $1 \times 10^{19}$  cm $^{-3}$ ) at 600 eV,  $1.3 \times 10^7$  is exactly twice the thermal velocity. Of course, as  $V_0 \rightarrow \infty$ , the plasma would become thin. Much smaller velocities would produce essentially the results for a static plasma.

In Fig. 1 are plotted the profiles for the static case and the imploding case described above. Line power output (i.e., the integral under the profile) does not change because the plasma in this case is effectively thin, that is, the photons generally escape after many scatterings, at this density. The profile, however, changes quite dramatically. The static plasma produces a self-absorbed line with symmetrical blue and red peaks, as expected. The imploding plasma line profile's blue peak far exceeds its red in intensity. This is due to the fact that, in a contracting plasma, every emitted photon is blueshifted relative to the rest of the plasma. Thus photons emitted on the blue side of the line center are 'seen' as even bluer by the rest of the plasma and thus escape easily. Photons emitted on the red side, however, are shifted blueward



$N_e = 1 \times 10^{19}$ ,  $T_e = 600 \text{ eV}$       Figure 1       $(\Delta\nu)$ , Doppler Widths

to line center where they are largely absorbed due to the high opacity at line center. Hence the domination of the blue peak for the imploding case.

Results at a total ion density of  $10^{20}$  have been obtained using the same total mass ( $75\mu$  plasma) and temperature (600 eV). The line profile phenomenology is the same as that described at  $10^{19}$ . However, at  $10^{20}$  the line energetics are significantly altered. The Al XII  $1s^2 - 1s2p^1P$  line remains unchanged in output by motional effects. Since the decay probability is so high ( $2.8 \times 10^{13} \text{ sec}^{-1}$ ), the probability that excitation of the 2p level is not followed by spontaneous decay to the ground state is extremely low. Hence, most photons in this line continue to escape even in the static case and motions have no effect. However, there are effects on other lines. The following table gives the ratio of various lines' output to that of the  $1s^2 - 1s2p$ , for the static and imploding cases at  $N_I = 10^{20}$ ,  $T_e = 600$  eV, and plasma half-width of  $75\mu$ .

<u>Line</u>	<u>Static</u>	<u>Imploding</u>
$1s^2 - 1s2p^1P$ (Al XII)	1.000	1.000
$1s^2 - 1s3p^1P$ (Al XII)	0.093	0.141
$1s^2 - 1s4p^1P$ (Al XII)	0.037	0.053
$1s^2 2p - 1s2p^2 2D$ (Al XI)	0.046	0.057
$1s^2 - 1s2p^3P$ (Al XII)	0.071	0.099
$1s - 2p$ (Al XIII)	1.226	2.102
$1s - 3p$ (Al XIII)	0.156	0.237
$1s - 4p$ (Al XIII)	0.175	0.210

Clearly, every line but the  $1s^2 - 1s2p^1P$  of Al XII has increased in output, with the very strong  $1s-2p$  hydrogen-like resonance line nearly doubling because motional broadening renders the line thinner than it would be in the static case.

ii. Analysis of Plasma Mixtures

Developing an understanding of how radiation from one plasma affects another is important in analyzing the effects of dissimilar plasmas upon each other and in developing a diagnostic capability for wire or puff shots when two or more different plasma elements are actually present. Figure 2, taken from NRL Memorandum Report 3934, by P. Burkhalter and J. Davis, shows a mixed silicon-aluminum spectrum from PITHON shot PI 6. Line ratios from both aluminum and silicon can be used to firm up the diagnostic information obtained from such a spectrum.

A part of the contract's work, a capability to analyze silicon-aluminum mixtures using our detailed radiation transport-multiplication dynamics code was established. The model was built in the following manner. First, a rate table for silicon transitions precisely analogous to the existing aluminum table was set up. Eight prominent spectral lines (the ones listed in the table contained in the preceding section) are fully self-consistently transported. The model includes, of course, the effects of plasma motion as described in Section II. Second, the emitted spectrum, angle-by-angle, can be stored on the

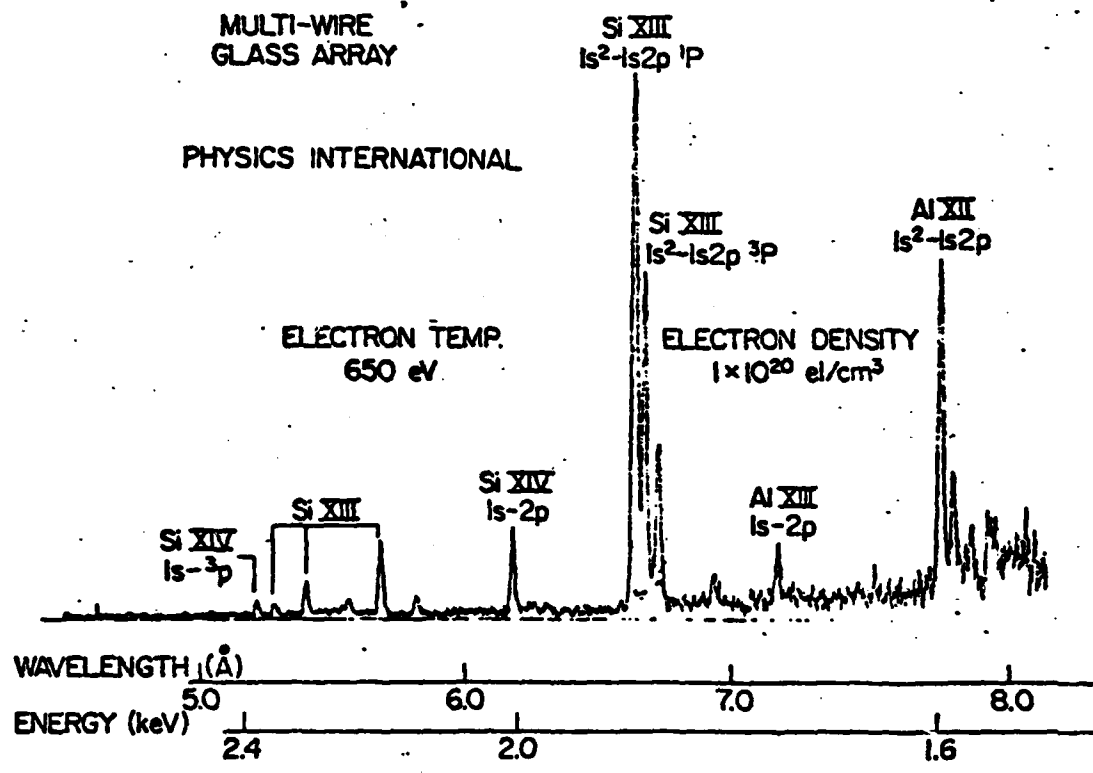


Figure 2

TI/ASC's disk files for either silicon or aluminum. Third, when the silicon or aluminum model is run, any stored spectrum on the disk from either element can be read and self-consistently transported through the element being run using the disk spectrum as a boundary condition. The total spectrum from both elements is outputted, and thus the effect of mixture can be gauged.

A dramatic example of how radiation from a silicon plasma affects the state and emitted spectrum of an aluminum plasma can be seen by comparing the next two figures. Figure 3 is the spectrum emitted by an aluminum plasma at a temperature of 100 eV, total ion density of  $5 \times 10^{19}$ , and half-width of  $5.56\mu$ . The lines are labelled, and the slanted line above the spectrum is the emission from a 100 eV blackbody. The peaks of all the lines are comfortably under the Planck curve. By contrast, Fig. 4 illustrates the spectrum emitted by the same aluminum plasma when it is irradiated by a silicon plasma surrounding it in a 'sandwich' configuration. The silicon plasma is at a temperature of 400 eV and total ion density of  $8 \times 10^{19}$ . There is assumed a  $1500\mu$  layer of silicon on each side of the aluminum. The spectrum emitted by the embedded aluminum (with the silicon lines removed for clarity) is radically different from that of the bare aluminum. In this case we have assumed that the silicon exterior of the plasma sandwich is imploding toward the aluminum at a velocity of  $3 \times 10^7$  cm/sec. The aluminum lines now are far above the 100 eV blackbody curve in intensity.

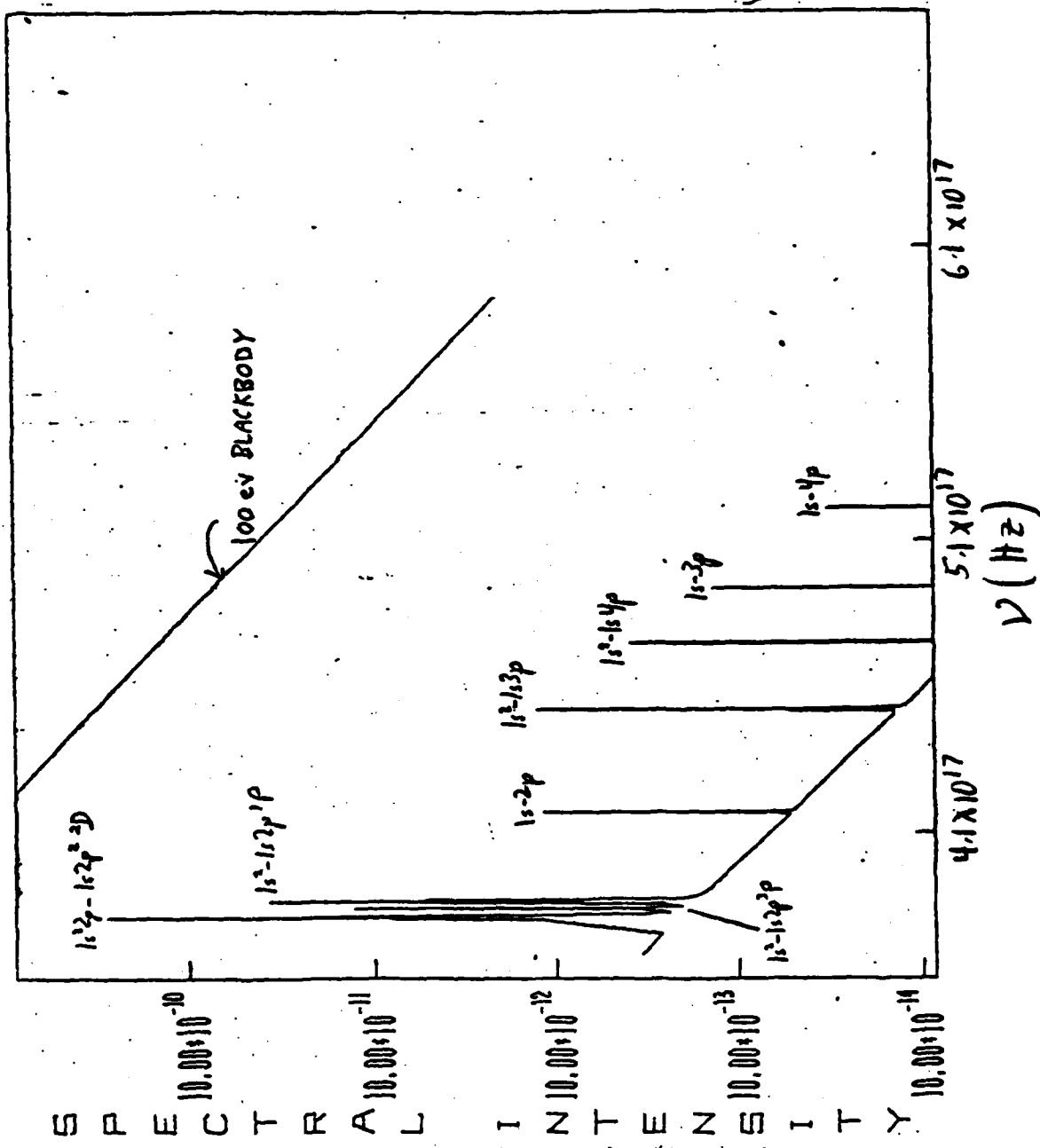


Figure 3

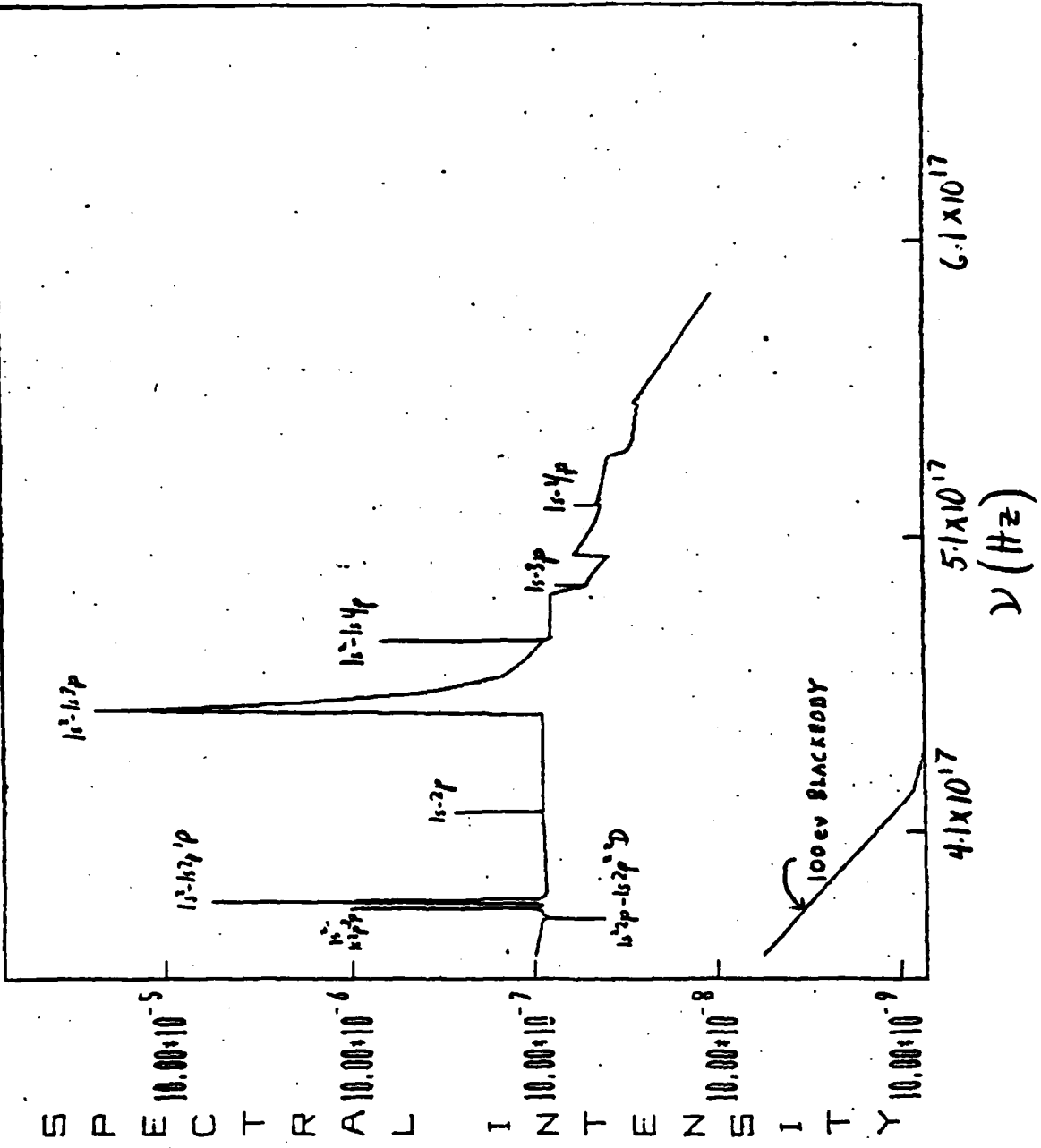


Figure 4

even though the kinetic temperature of the aluminum plasma is 100 eV. This effect is of course due to the fact that the silicon radiation, both lines and continuum, photoionizes and photoexcites bound levels of the aluminum plasma. This raises the state of excitation of the aluminum plasma far above what is obtained from a "bare" 100 eV aluminum plasma - in fact even far above that of an LTE 100 eV aluminum plasma. The ratios of lines are quite significantly changed also, with the satellite line actually seen in absorption in the pumped plasma. The pumped plasma also exhibits an ultra-strong Al XII  $1s^2$  -  $1s3p$  line (at  $6.635\text{\AA}$ ). This effect is due to the fact that the Si XIII  $1s^2$  -  $1s2p$  line lies at  $6.650\text{\AA}^\circ$ , and therefore photons emitted in this line by the outer silicon region are intercepted in the Al XII  $1s^2$  -  $1s3p$  transition, greatly augmenting its output. The lesson is clear - when two plasmas are interacting, the photons from one can drastically affect the excitation state and thus the diagnostic interpretation of radiation emitted by the other plasma.

The pumping of the Al XII  $1s^2$  -  $1s3p$  line by the Si XIII  $1s^2$  -  $1s2p$  line referred to above is also useful in principle as a diagnostic of exploding - wire plasma mixtures. Under certain conditions, the Al XII 3-2 states may become inverted in population, resulting in the lasing of the  $44\text{\AA}^\circ$  lines coupling these states. The establishment of a population inversion, and hence the strength of this line, is sensitively

dependent on properties of the plasma mixture. As an example of this, Figs. 5 and 6 display the gain coefficient of the Al XII  $1s2p^1P - 1s3d^1D$  line (the strongest lasing line) as a function of aluminum plasma density and size. Such variations with size and density reflect the extent to which Si XIII pumping photons are able to penetrate the aluminum region, as well as the collisional quenching of the gain by electron impact processes occurring in the aluminum region. Our studies of these pumping effects also indicate considerable sensitivity of the gain to aluminum plasma temperature. The silicon plasma's radiation tends to over-ionize the aluminum plasma and thus little or no gain is observed at temperatures in the 1 Kev range. It is to be emphasized that the degree of gain present in the 3-2 transitions will be sensitively reflected in the experimentally observed strength of the  $44 \text{ } \overset{\circ}{\text{A}}$  lines. In turn, this experimental quantity reflects the state of the component silicon and aluminum plasmas. Much remains to be understood on the extent to which such pumping effects are usable as plasma mixture diagnostics.

### iii. Probabilistic Radiation Transport

As reported previously,<sup>(4)</sup> SAI has developed an efficient escape probability technique for transporting line radiation. In the performance period of the present contract, the technique was used to analyze effects of optically thick lines arising from excited states in an aluminum plasma. A copy of the completely updated report on this method,<sup>(5)</sup> "Direct Solution of the

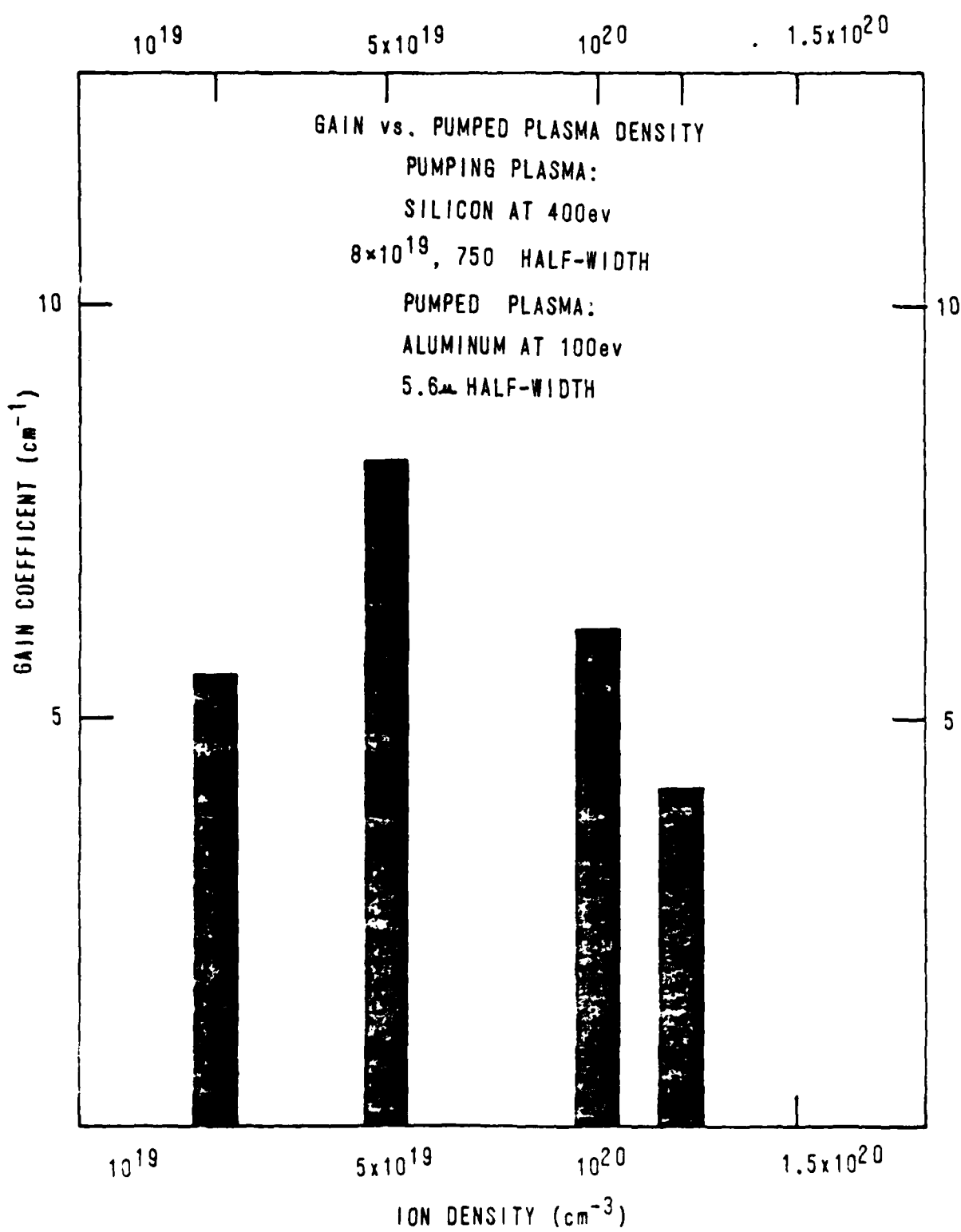


Figure 5

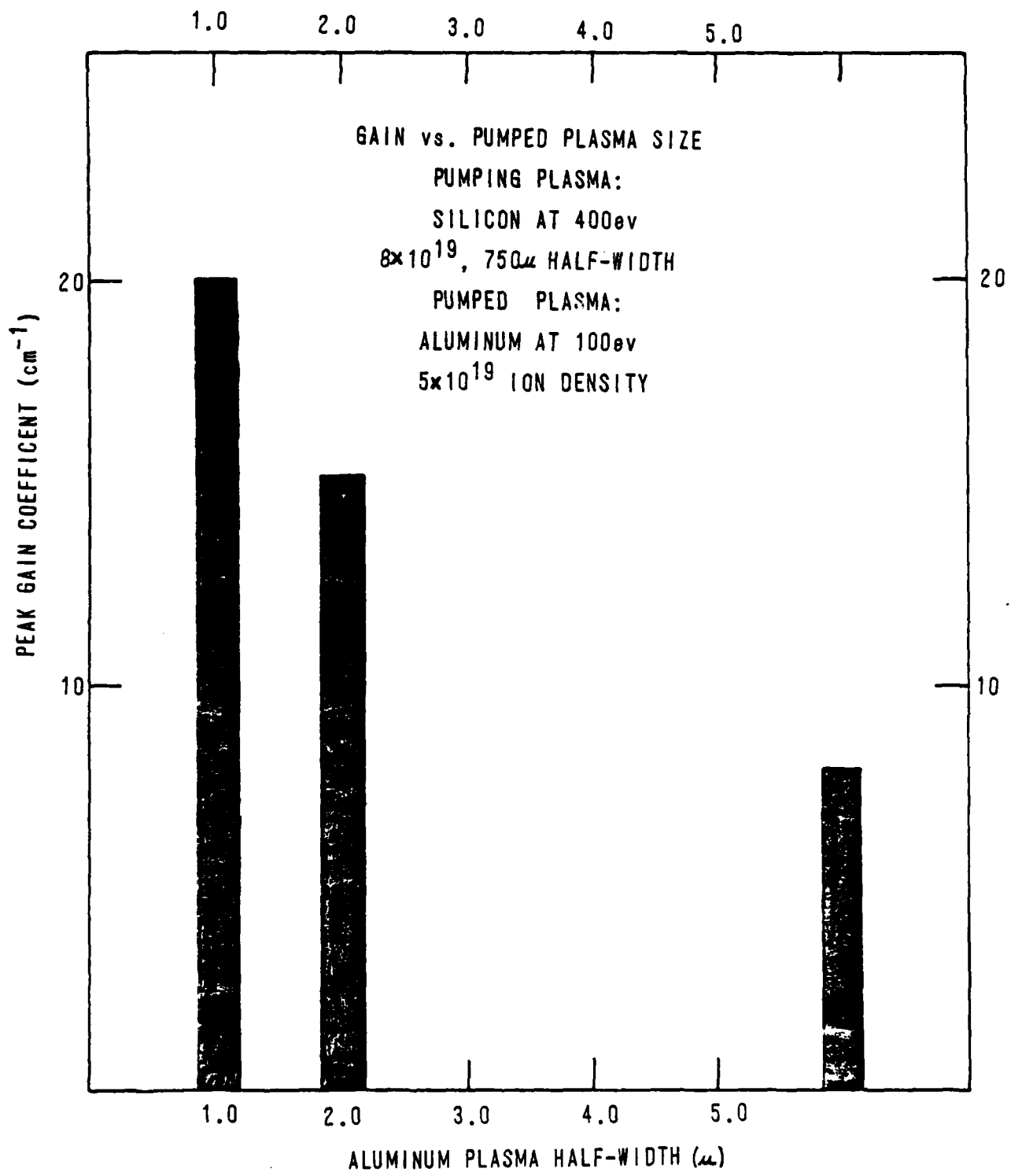


Figure 6

Equation of Transfer Using Frequency - and Angle - Averaged Photon Escape Probabilities, with Application to a Multistage, Multilevel Aluminum Plasma", is included as Appendix E.

iv. Effect of Experimental Resolution on Spectra

One of the best ways to diagnose the properties of wire-like and imploding pellet plasmas is the analysis of various spectral features. Every experimentally measured spectrum is affected, to a greater or lesser degree, by instrumental and source broadening which is generally assumed to be Gaussian in character. To provide a quantitative and detailed capability to gauge the effects of experimental broadening, a program was established to catalog all the spectra calculated theoretically and convolute them with Gaussian broadening functions. The convoluted spectrum is then suitable for direct comparison with experiment. Our results graphically illustrate the evolution of a "pure theoretical" spectrum into an observed spectrum as the experimental broadening increases. This evolution is seen in the next section for the case of an opacity and velocity-broadened aluminum spectrum. This spectral convolution capability will provide a much more direct connection of our theoretical models with experiment and thus aid in the determination of the basic properties of both wire and pellet plasmas.

v. Analysis of Motional Broadening in an Aluminum Wire Plasma Spectrum

The principal resonance line of helium-like Al XII,  $1s^2 - 1s2p^1P$ , as observed during Maxwell Laboratories' shot 159, exhibited an interesting feature on the red side of the line profile, as seen in Fig. 7. As discussed above, such a red wing can be produced by plasma implosion when the line is optically thick enough to be self reversed. In the case of implosion, the blue wing exceeds the red in intensity. Using both a simplified probability-of-escape model and a detailed ray-trace aluminum plasma model, a radius of  $250\mu$ , temperature of 500 ev, and total ion density of  $8 \times 10^{18} \text{ cm}^{-3}$  were obtained as characteristic plasma parameters from the various spectral line ratios. The detailed model agreed very well with the simpler code in this case, since the plasma is "effectively thin". The table gives the measured and modeled line ratios for the above parameters.

$$r = 250\mu, T_e = 500 \text{ ev}, N_i = 8 \times 10^{18} \text{ cm}^{-3}$$

<u>Ratio</u>	(Spherical) <u>Measured</u>	<u>Modeled</u>
$L_\alpha   1s^2 - 1s2p^1P$	0.14	0.12
$L_\beta   1s^2 - 1s2p^1P$	0.04	0.031
$1s^2 - 1s3p^1P   1s^2 - 1s2p^1P$	0.015	0.011
$1s^2 - 1s4p^1P   1s^2 - 1s2p^1P$	0.007	0.007

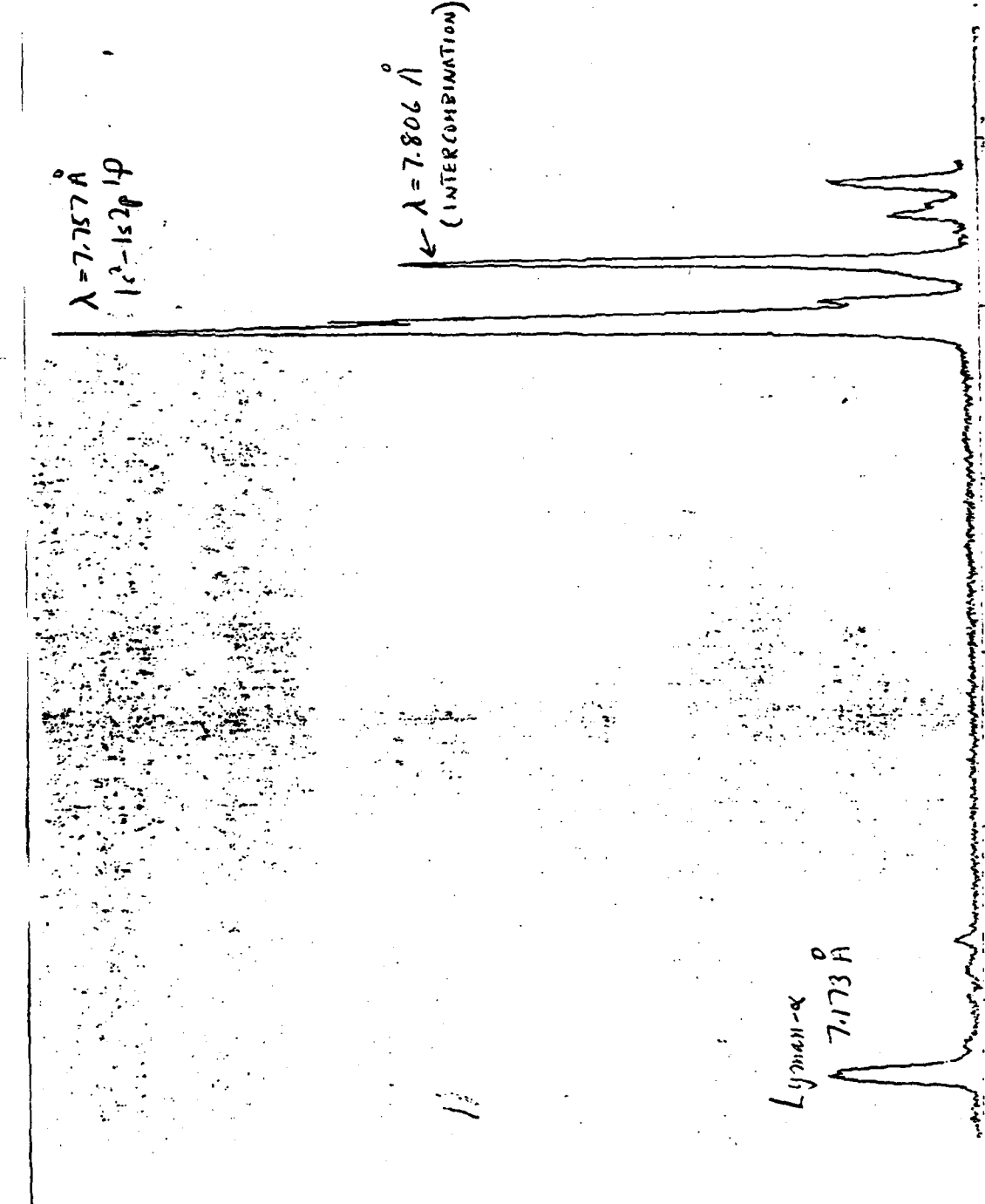


Figure 7

Given these plasma properties, a series of computations with different implosion velocities were performed to attempt to diagnose the characteristic velocity in shot 159 from the resonance line profile. An implosion velocity of  $4 \times 10^6 \text{ cm sec}^{-1}$  at the outer radius (linearly ramping from  $r = 0$ ) was found to reproduce quite well the observed profile. This velocity, which is obviously quite important to know in order to understand the conversion of plasma kinetic energy to x-rays, agrees quite well with theoretical hydrodynamic calculations. The major uncertainty in the analysis is the amount of experimental broadening in the spectrum in Fig. 7. The amount of experimental broadening,  $\Delta\lambda_e$ , in  $\text{\AA}^\circ$  (full-width-half-maximum) is given by

$$\Delta\lambda_e = \sqrt{(\Delta\lambda)_m^2 - (\Delta\lambda)_i^2}$$

where  $(\Delta\lambda)_m$  and  $(\Delta\lambda)_i$  are the measured and intrinsic line FWHM's. The measured FWHM of the Al XII intercombination line is  $6.2 \pm 1.5 \text{ m \AA}^\circ$ . The intrinsic line width, obtained from a radiative transfer calculation is approximately  $4 \text{ m \AA}^\circ$ . Clearly, the widths are consistent with very little ( $\sim 1 \text{ m \AA}^\circ$ ) or quite a bit ( $\sim 7 \text{ m \AA}^\circ$ ) of broadening. The effect of broadening on the observed spectrum is dramatically illustrated in Figs. 8-11 where the spectrum with broadening of 0., 1., 1.59, and  $2.73 \text{ m \AA}^\circ$ , respectively, is shown. The "washing-out" of the motional-broadening feature is clearly seen.

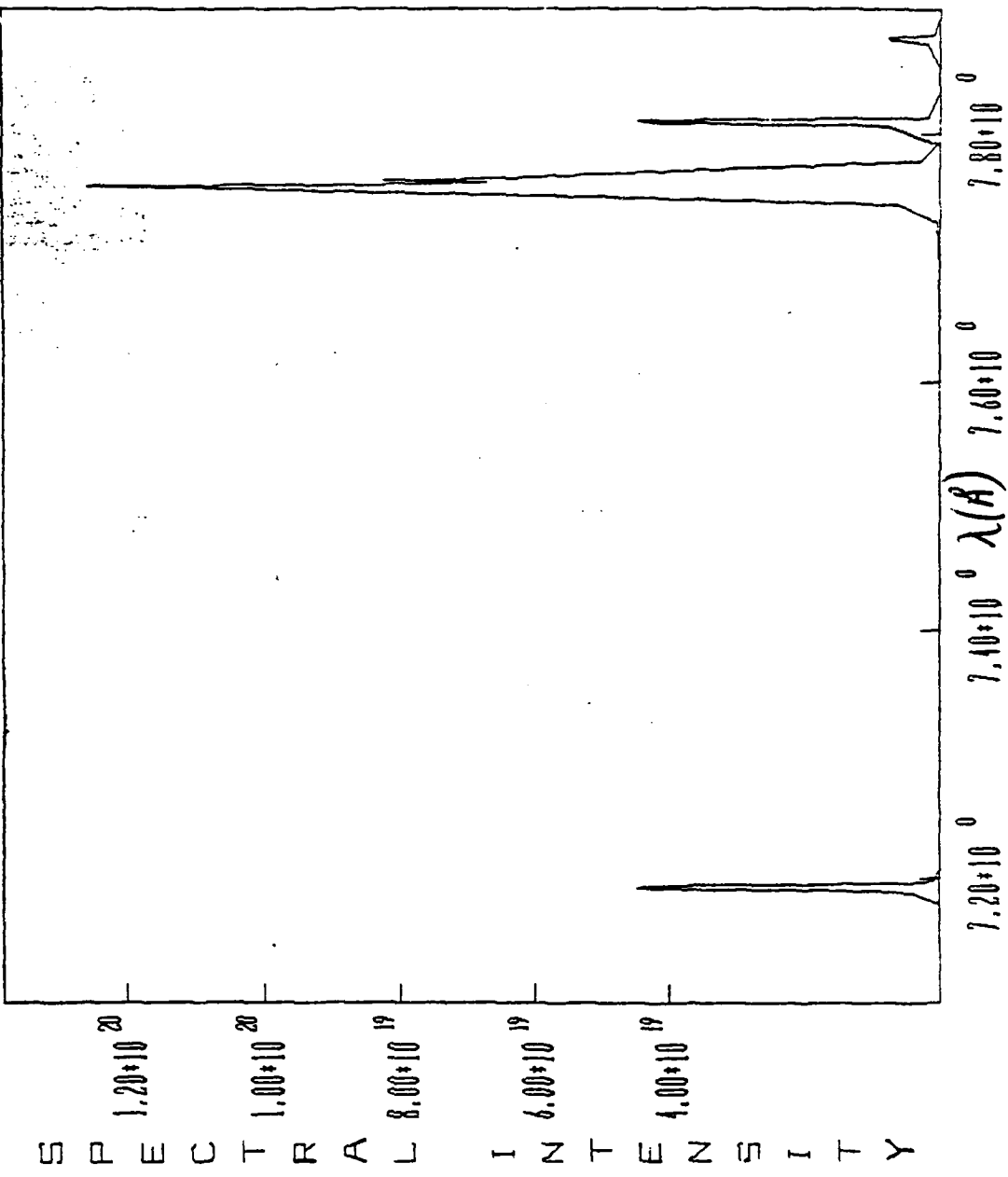


Figure 8

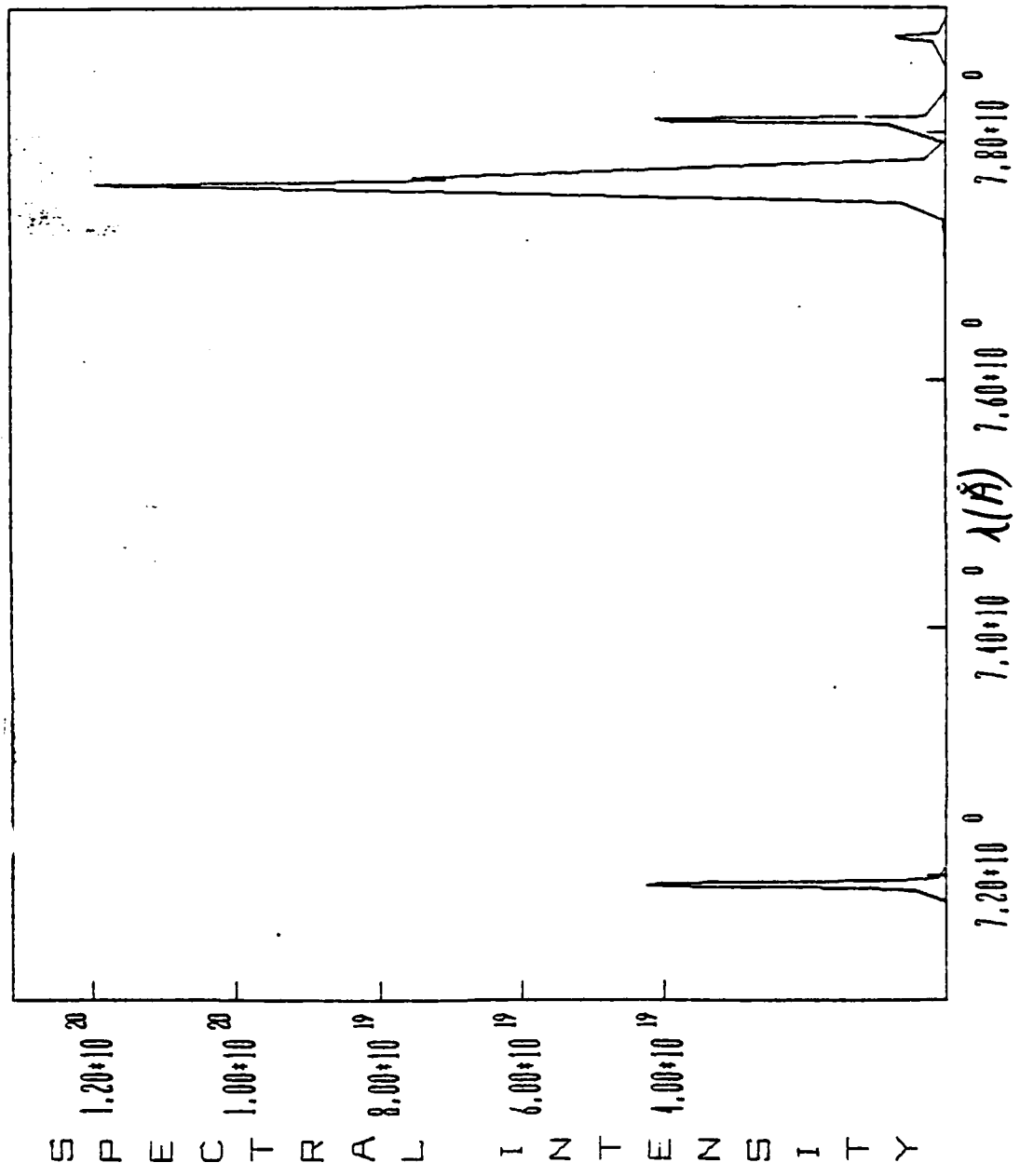


Figure 9

→ 3.1

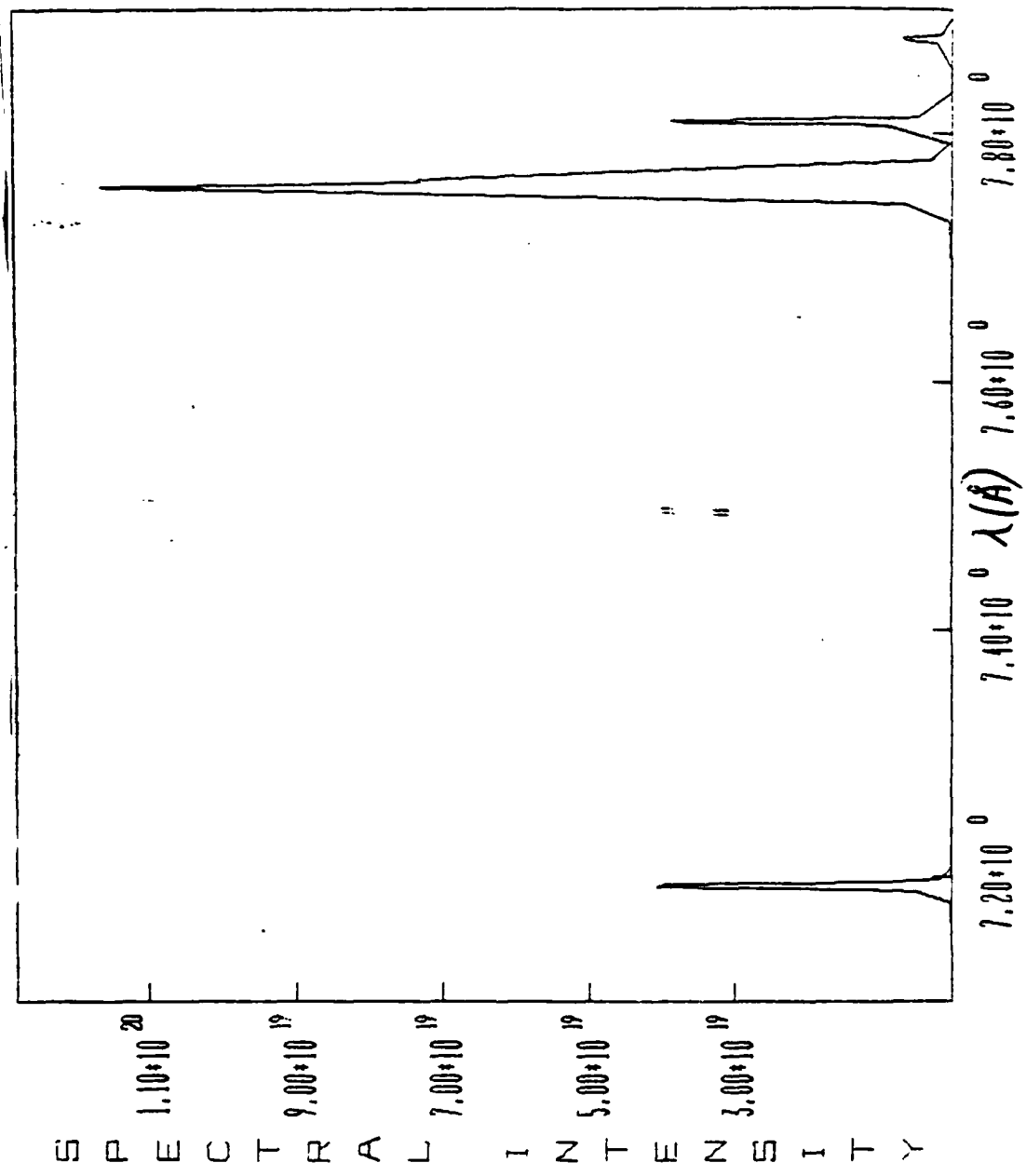


Figure 10

-3.5.10

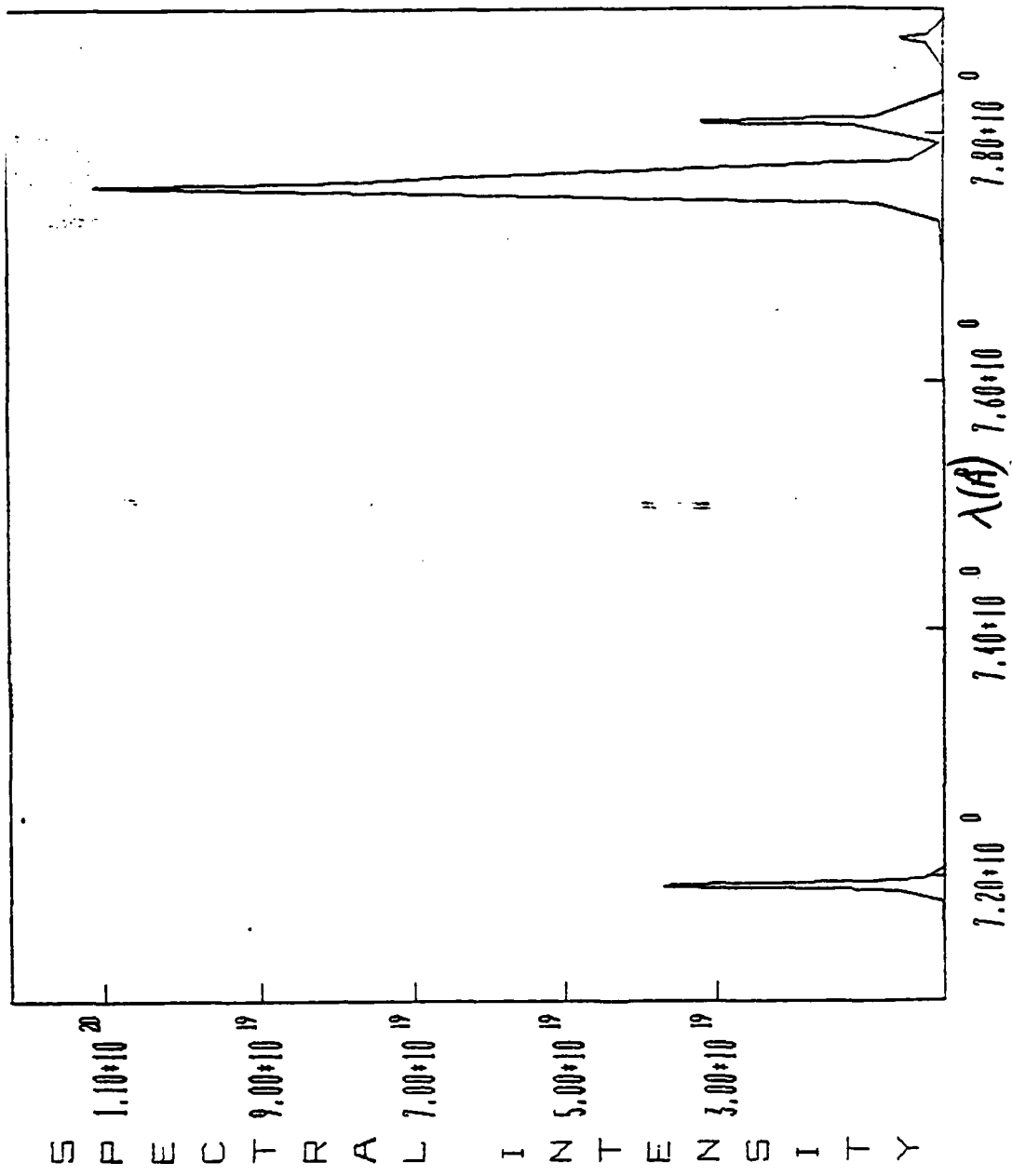


Figure 11

Interestingly, the most dramatic agreement of the line profile is seen for no assumed experimental broadening. The fact that this feature is observed would appear to indicate that the source and instrumental broadening were indeed quite low in this case. It should also be pointed out that the Ly  $\alpha$  modeled width is smaller than the experimental width because the fine structure is not modeled. However, the integrated intensity of this line agrees quite well with the experiment.

vi. Properties of an Imploded Neon Plasma

One technique which has been successfully used to obtain information characterizing imploded pellets is to utilize an inert filler gas such as argon or neon, and analyze the filler spectrum. To aid in such analysis, a multi-stage, multi-level neon model was constructed for use in our large radiative transfer code. Self-consistent Stark profiles supplied by P.C. Kepple were used as the line opacity contour. To benchmark this study, we have reproduced remarkably well with the model an experimental spectrum previously obtained at Rochester. We obtain as a fit for this spectrum a density of  $4.5 \times 10^{21}$  ions  $\text{cm}^{-3}$  and temperature of 385 ev. By contrast, the original Rochester analysis yielded  $T_e = 300$  ev and  $N_i = 7.8 \times 10^{21} \text{ cm}^{-3}$ . Figure 12 displays the experimental spectrum at the top, followed by the "best fit" theoretical spectrum. The lowest spectrum on the graph is that which would be emitted by a plasma characterized by the conditions

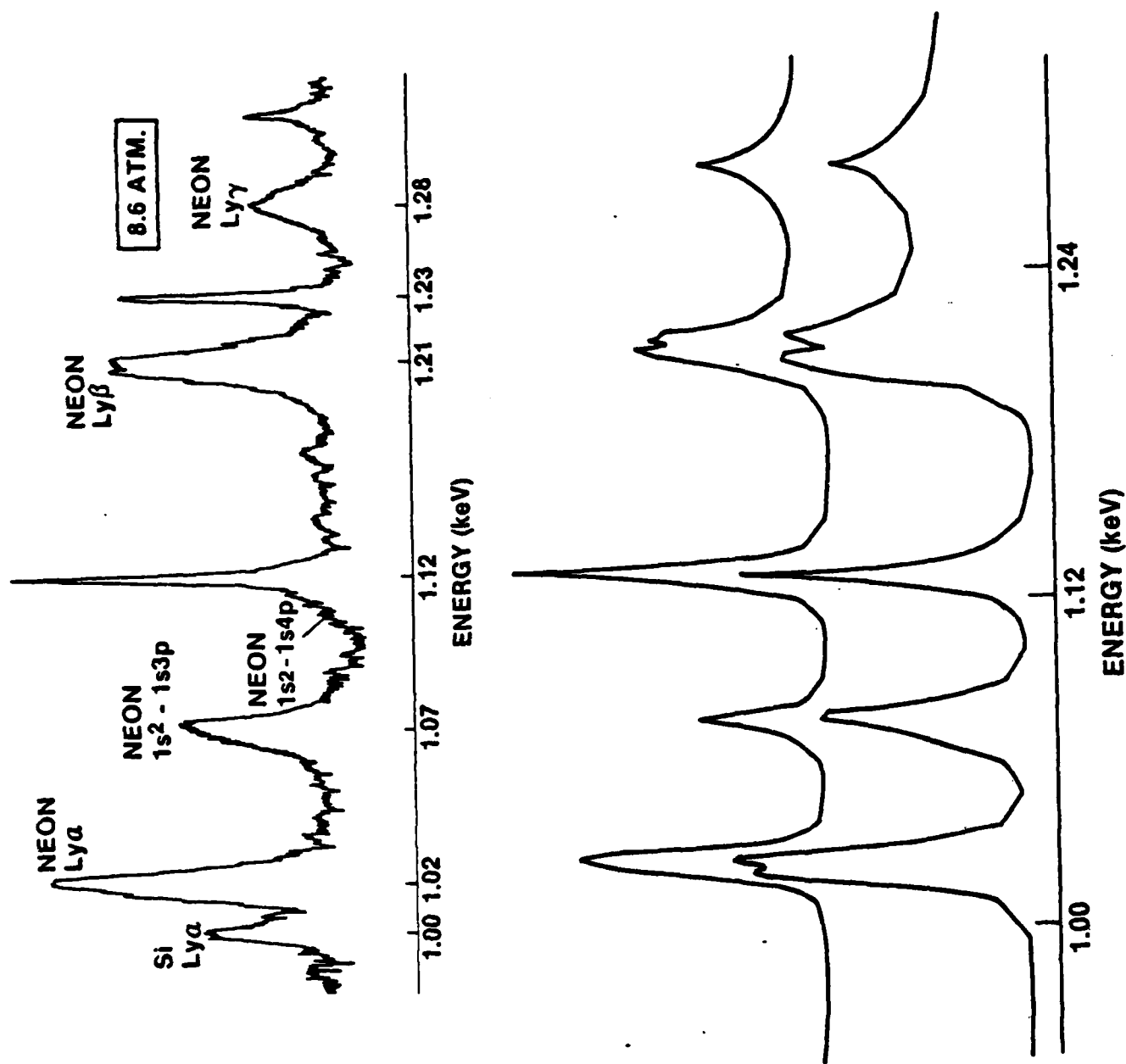


Figure 12

of the Rochester analysis. The increase in temperature to 385 ev is necessary to remove the prominent helium continuum feature which would occur at 300 ev and is not observed. The reduction in density (from  $7.8$  to  $4.5 \times 10^{21} \text{ cm}^{-3}$ ) is necessitated by the fact that at  $7.8 \times 10^{21} \text{ cm}^{-3}$ , opacity broadening renders the predicted line widths greater than those experimentally observed. This benchmark analysis strikingly illustrates the great value of analyzing all the features in a given spectrum to obtain precise plasma parameters.

3. Radiation Hydrodynamics Modeling

a) Cylindrical Geometry

It is generally accepted that cylindrical geometry is the most realistic simple geometry for modeling collapsing z-pinches. Significant effort has been performed on the establishment of a collapsing z-pinch hydrodynamics code WHYRAD, initialized by wires, gas puffs, or annular foils, employing a variety of ionization physics-radiation input subroutines. A wide variety of initial radial distributions of particle number density and temperature, timewise variation of machine discharge voltage, and anomalous resistivity functions may be employed; in addition, operational flexibility due to general re-start and subroutine vectorization as well as spectral and radial distribution plotting routines is also available.

i. One-Dimensional z-Pinch Model

Analysis of the dynamics of an imploding z-pinch plasma depends on magnetohydrodynamic coupling of the time-dependent equations of mass, momentum, electron and total specie energy, magnetic flux and the thermal and caloric

equations of state, as well as the specification of appropriate transport processes. Solution of these equations is also dependent on the coupling into the driving discharge circuit, which in turn is altered by the changing plasma conditions. The appropriate equations are assumed to be one dimensional, and cylindrically symmetric. The energy density of the plasma involves an adiabatic exponent which contains the potential ionization energy that is calculated from a selected ionization-radiation package. Thermal flux coefficients are determined from the expressions listed in Braginski;<sup>(6)</sup> thermally perfect plasma species and charge neutrality are also assumed.

Magnetic field diffusion within the z-pinch involves  $\eta_1$ , a cross-field resistivity having a limiting classical value of<sup>(7)</sup>

$$\eta_1^{\text{cl}} = 1.15 \times 10^{-14} Z_I \ln \lambda (T_e)^{-3/2} \text{ (sec)} \quad (1)$$

where  $Z_I$  is the ionic charge,  $\ln \lambda$  is the Coulomb logarithm and  $T_e$ , the electron temperature, is in eV. Experimental results indicate that non-classical anomalous turbulent values of some of the transport processes, in particular the resistivity, are required for suitable correlation. Plasma turbulence would be strongly influential in the outer lower density coronal region of the discharge and for tens of nanoseconds and above time scales. As a first model it is assumed that only the resistivity is affected by anomalous

turbulence levels, the other transport properties retaining their classical magnitudes. The empirical quadratic relation of the form

$$\eta_1^{an} = \eta_1^{cl} \left\{ 1.0 + (g(t) - 1.0) (r/R)^2 \right\} \quad (2)$$

is chosen, where R is the outer discharge radius and the growth factor g is

$$g(t) = 1.0 + A (t/t_{pulse})^B \quad (3)$$

where A and B are empirical coefficients and  $t_{pulse}$  is the total pulse time. The core limit of  $\eta_1^{an} \rightarrow \eta_1^{cl}$  as  $r \rightarrow 0$  is maintained as well as the initial condition  $\eta_1^{an} \rightarrow \eta_1^{cl}$  as  $t \rightarrow 0$  for any r.

Solution of the equation system, except for the magnetic flux relation and the thermal diffusion is by application of the explicit flux corrected transport (FCT) method.<sup>(8)(9)</sup> This method effectively transports steep fluid gradients and does not require the incorporation of artificial viscosity. Initial condition distributions of the dependent variables are specified at all finite difference radial locations either at  $t = 0$  or at an appropriately chosen restart time. The magnetic field and thermal diffusion equations are solved by an implicit tridiagonal (Gaussian elimination) algorithm. The radial finite difference representation is incrementally uniform with zero gradients of

dependent variables assumed at the discharge centerline and outer plasma boundary.

The discharge plasma within its return current cage is modeled as a plasma cylinder in contact at one end with a grounded perfectly conducting metal return current path and at the other end with an electrode at voltage  $V_{pl}(t)$ . Specification of Ohm's law and Faraday's equation within the discharge yields the radial electric field distribution in terms of  $V_{pl}$  and the  $\partial B_\theta / \partial t$  flux of the azimuthal magnetic field.

The ionization-radiation packages employed are ATPHYS, a relatively simple ground state only ion balance with optically thick radiation, and MCELL, a package which solves for the ground and excited state population densities. Line, radiation recombination and Bremsstrahlung radiation transport are considered, with the ionization balance determined by a number of distinct processes within the collisional-radiation equilibrium method.<sup>(1)</sup> Radiation transport is modeled with emission and absorption balanced out over the multi-cell radial increment zones.

To check the feasibility of the WHYRAD-MCELL linkage, a series of optically thin aluminum k-shell computations were performed. While physical validity may be questioned, especially for 10 eV initial wire plasma temperatures,

useful information regarding parameter dependencies, such as due to anomalous resistivity, may be obtained. The first series of runs assume a representative model voltage-time distribution illustrated in Figure 13, having a maximum value of  $1.5 \times 10^6$  V and symmetric within a pulse time of  $2 \times 10^{-7}$  sec. The radial extent is broken up into 33 increments, and 300 time steps are employed with an initial Gaussian distribution of ion number density

$$N_I = N_{I, \max} \exp \left\{ -\frac{(r-r_0)^2}{R^2} \right\} \quad (4)$$

where  $N_{I, \max} = 5.0 \times 10^{18} \text{ cm}^{-3}$ ,  $r_0$ , the initial wire radius being 0.75 cm and  $R = 0.25$  cm. This combination of parameters together with a discharge length of 3.0 cm and an outer plasma edge of 1.32 cm yields a total mass of  $4.72 \times 10^{-4}$  gm. This is of the same order of magnitude as experimental multi-wire configurations. Initial ion and electron temperatures are assumed to be 10 eV; as the optically thin radiation quickly cools the plasma to values below 1 eV, which is in a range with poor representation of continuum radiation, the radiation power feedback from MCELL to WHYRAD is cutoff for an initial limited number of time steps (30 or 10% of the total). Such a procedure seems to be adequate for the various input data.

Figure 14 illustrates  $T_e$  at four different times

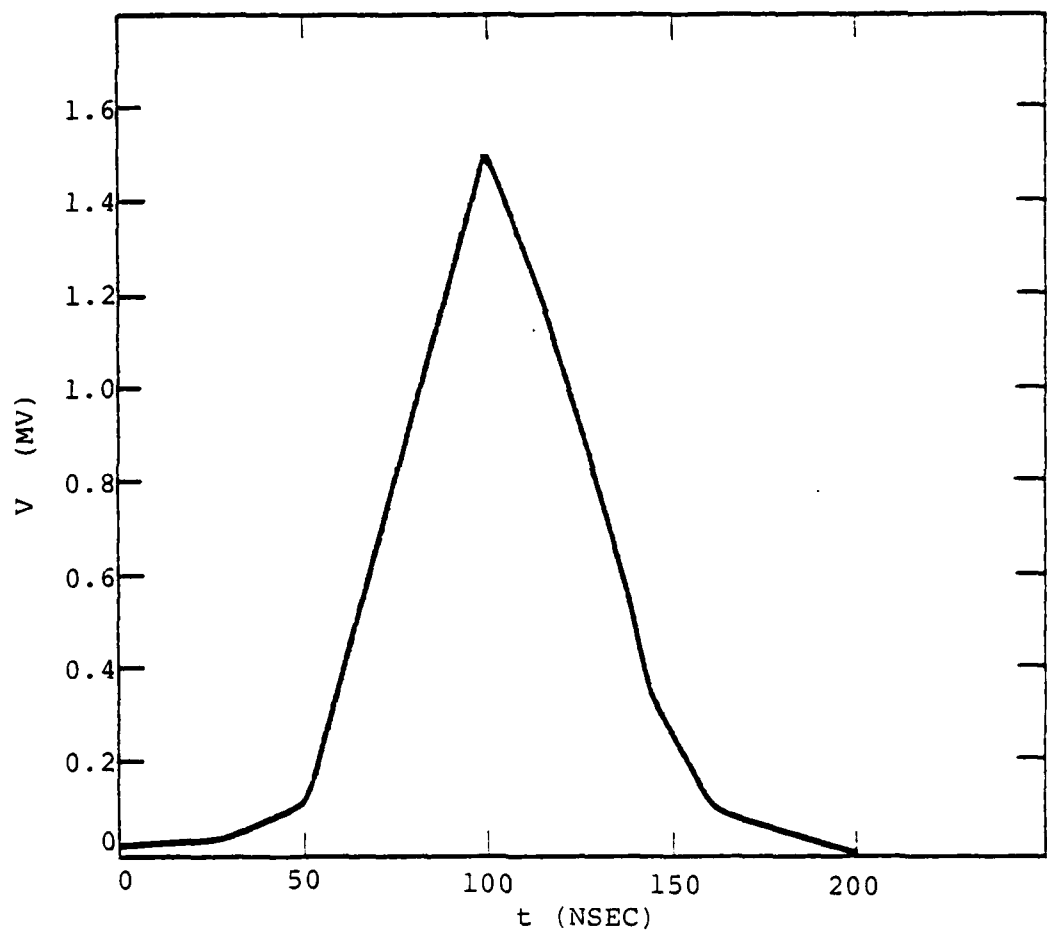


FIGURE 13: Model Voltage - Time Distribution

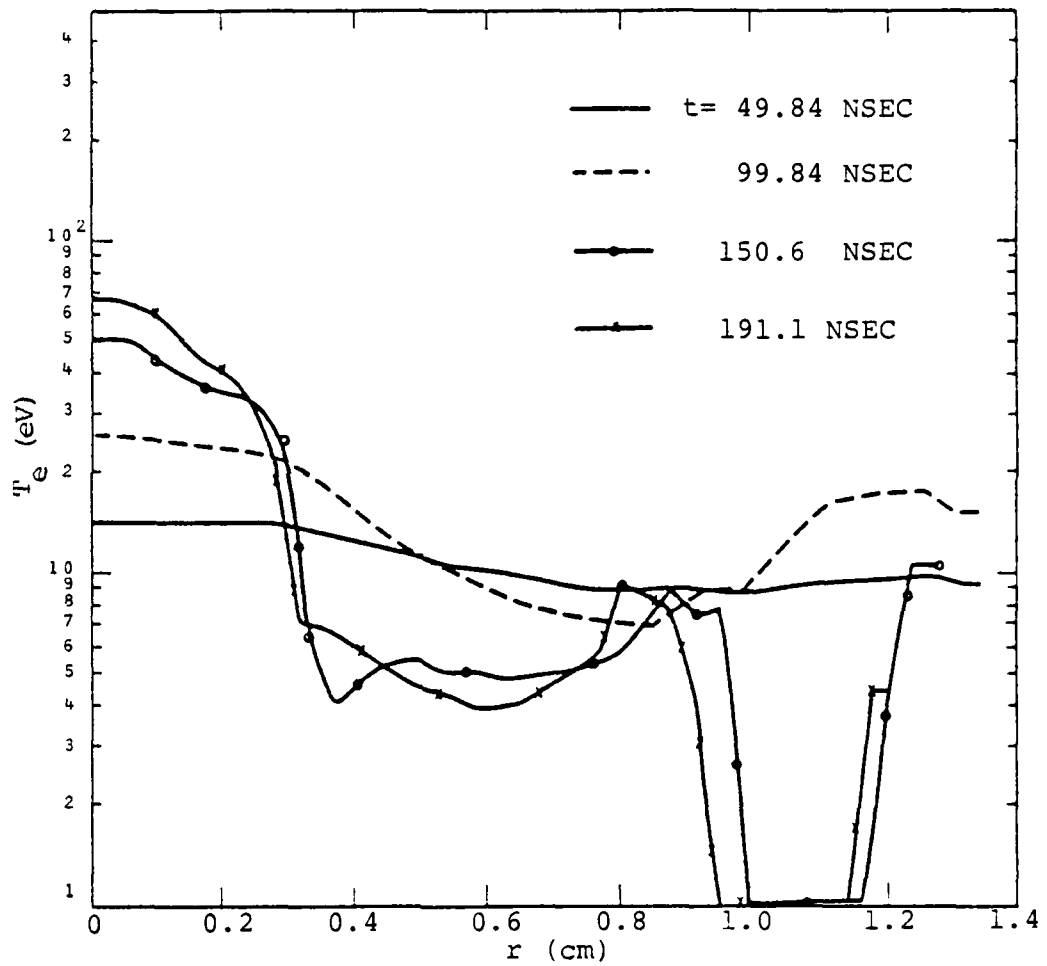


FIGURE 14: Optically Thin, K-Shell  
 $\text{Al}$   $T_e(r,t)$  Distribution.  $B=10^{-4}$ ,  
 Radially Uniform  $\eta$

with  $A = 99.0$  and  $B$ , the timewise resistivity power factor in Eq. (3), equalling  $10^{-4}$ , essentially the always completely turbulent extreme. The radial dependency of  $\eta_1$ , given by Eq. (2), is suppressed by letting  $r = R$  so as to emphasize the timewise influence. It is seen that for later times and larger radii the electron temperature drops below the 1.0 eV cutoff. It is to be noted that there is a minimum amount of radial compression through the run period due to the lack of radiant absorption. Figure 15 shows  $T_e$  at essentially the same four times with  $B = 1.0$ , modelling a linear increase between the classical and 100 times classical limits. The  $T_e$  distributions fall off, radially, somewhat more steeply than the previous case beyond the maximum voltage point (at  $10^{-7}$  sec.); up to there the distributions are virtually identical. This illustrates an interesting transient effect due to the resistivity magnitude; when there is a factor of 4 and 2 in resistivity difference, respectively, at 50 and 100 nsec the temperature distributions are very similar. However, at later times, when the resistivities are closer in magnitude, the temperatures are much farther apart. Accurate representation of the resistivity growth rate is therefore important. Analogous effects on the radial distribution of axial current and azimuthal magnetic field should also be noted.

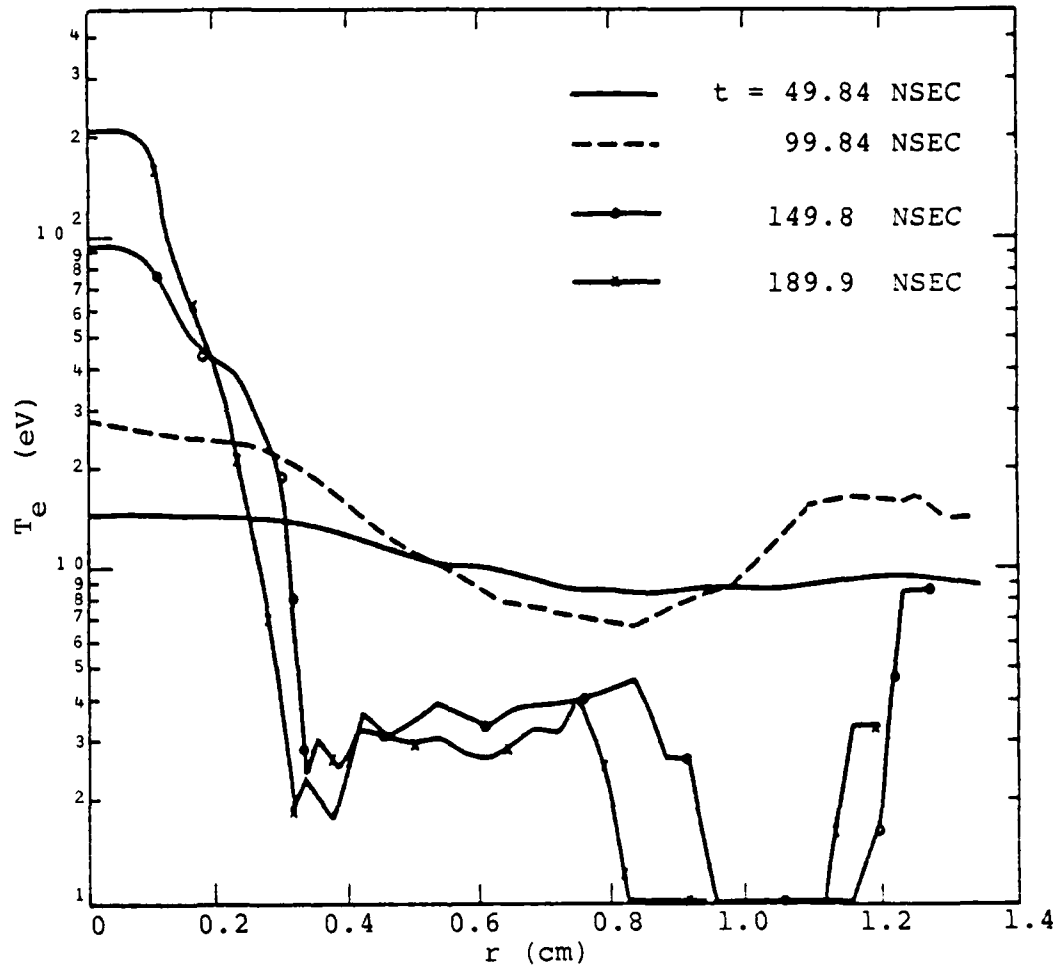


FIGURE 15: Optically Thin, K-Shell Al  $T_e(r,t)$   
Distributions  $B = 1.0$  Radially Uniform  $n$

The more complete  $n_1$  representation, involving a radial dependency (Eq. (2)) with a laminar core-turbulent corona is tested by correlation with a set of Ar gas puff data, shot #1440 at Physics International. The ionization-radiation option is the ATPHYS ground state model. Even though good correlation of the magnitude of the radiant emission as well as any information regarding the spectral line distribution cannot be made with the simple radiation option, it is informative to compute the timewise variation of the line and continuum radiant emission versus the external circuit tube voltage distribution and compare with the data. Furthermore, the initial ion radial number density distribution furnishes a superior estimate than the usual Gaussian.

Figure 16 shows the timewise voltage distribution employed; linear fits over 26 time segments closely model the experimental input out to the 400 nsec cutoff. Figure 17 illustrates the  $N_I(r) @ t = 0$  distribution; values at radial distances beyond 1.7 cm is a linear estimate. Cathode to anode discharge length is 5.0 cm; it is also assumed that initial radially uniform  $T_e$  and  $T_I$  magnitudes of 2.0 eV are suitable. Figures 18 and 19 illustrate the electron temperature and average Ar ion number density at 4 separate time steps over a 390 time step calculation, with the flow field divided into 39 radial increments. It is assumed

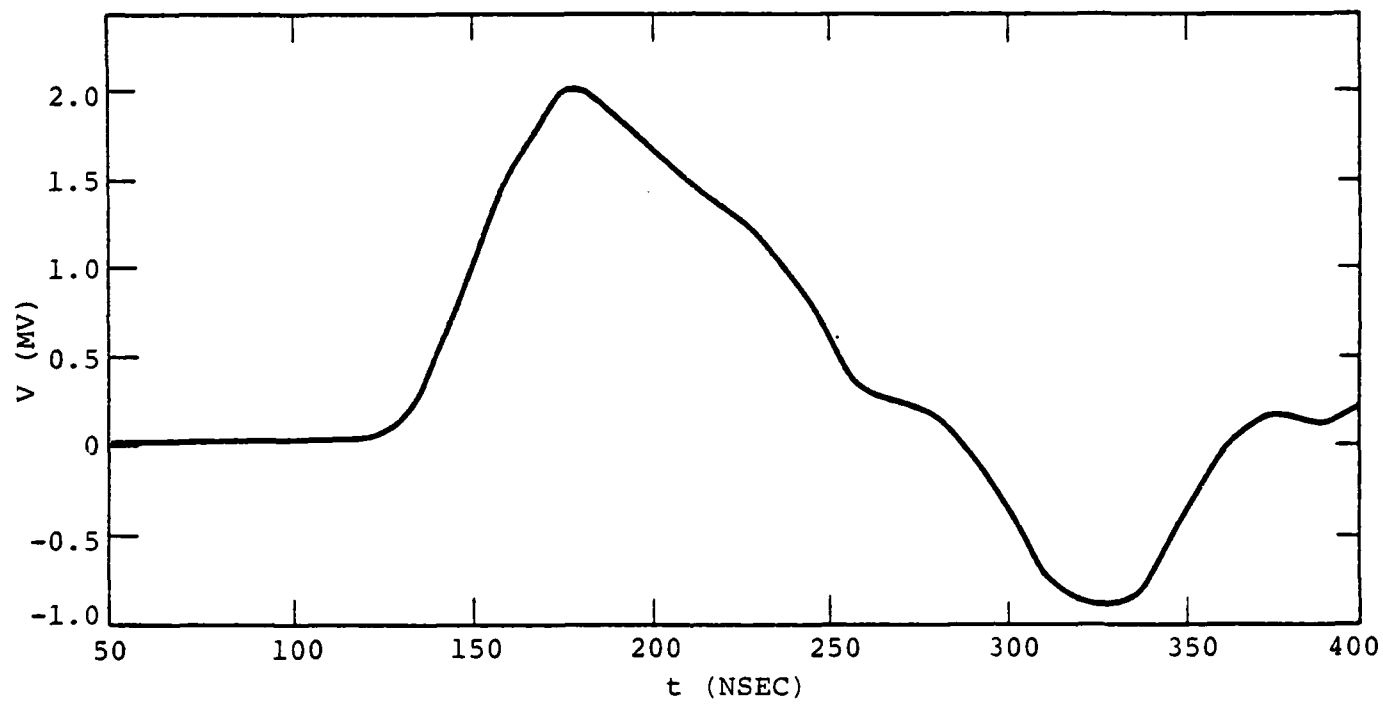


FIGURE 16: Physics International Shot No. 1440  
Voltage - Time Distribution

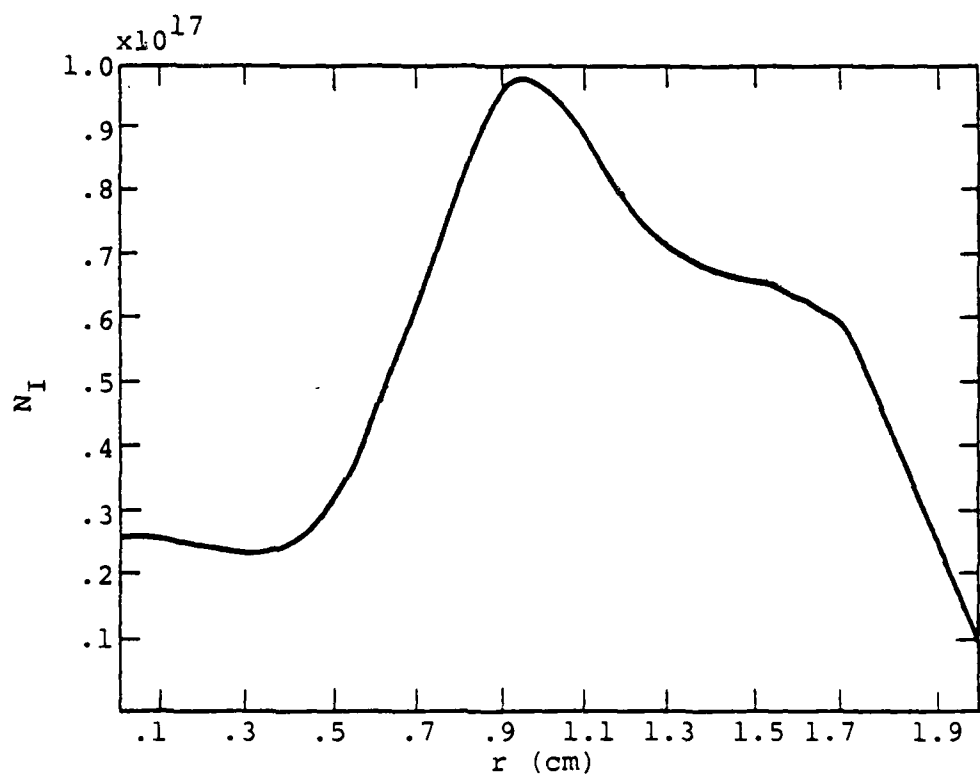


FIGURE 17: Initial Ar Gas-Puff Atom Number Density Distribution

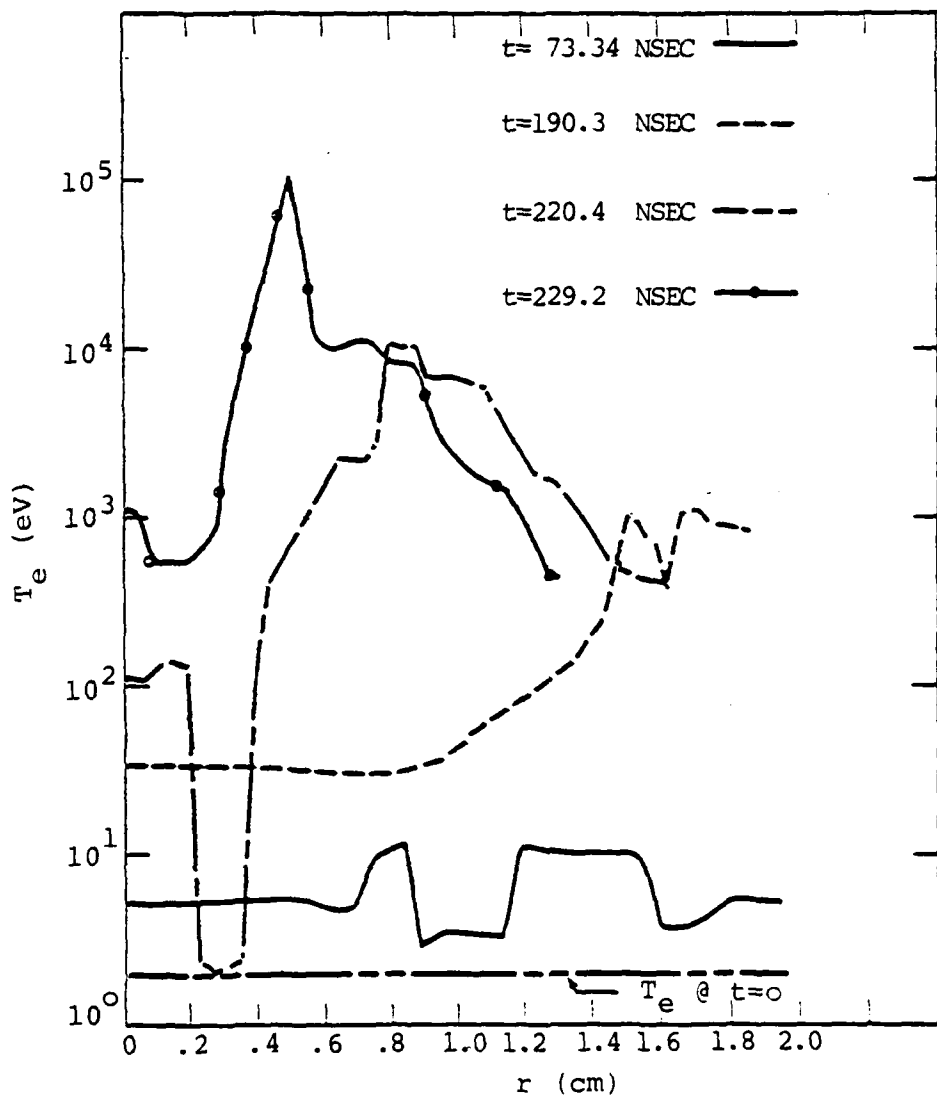


FIGURE 18: Radial Distribution of Ar Electron Temperature

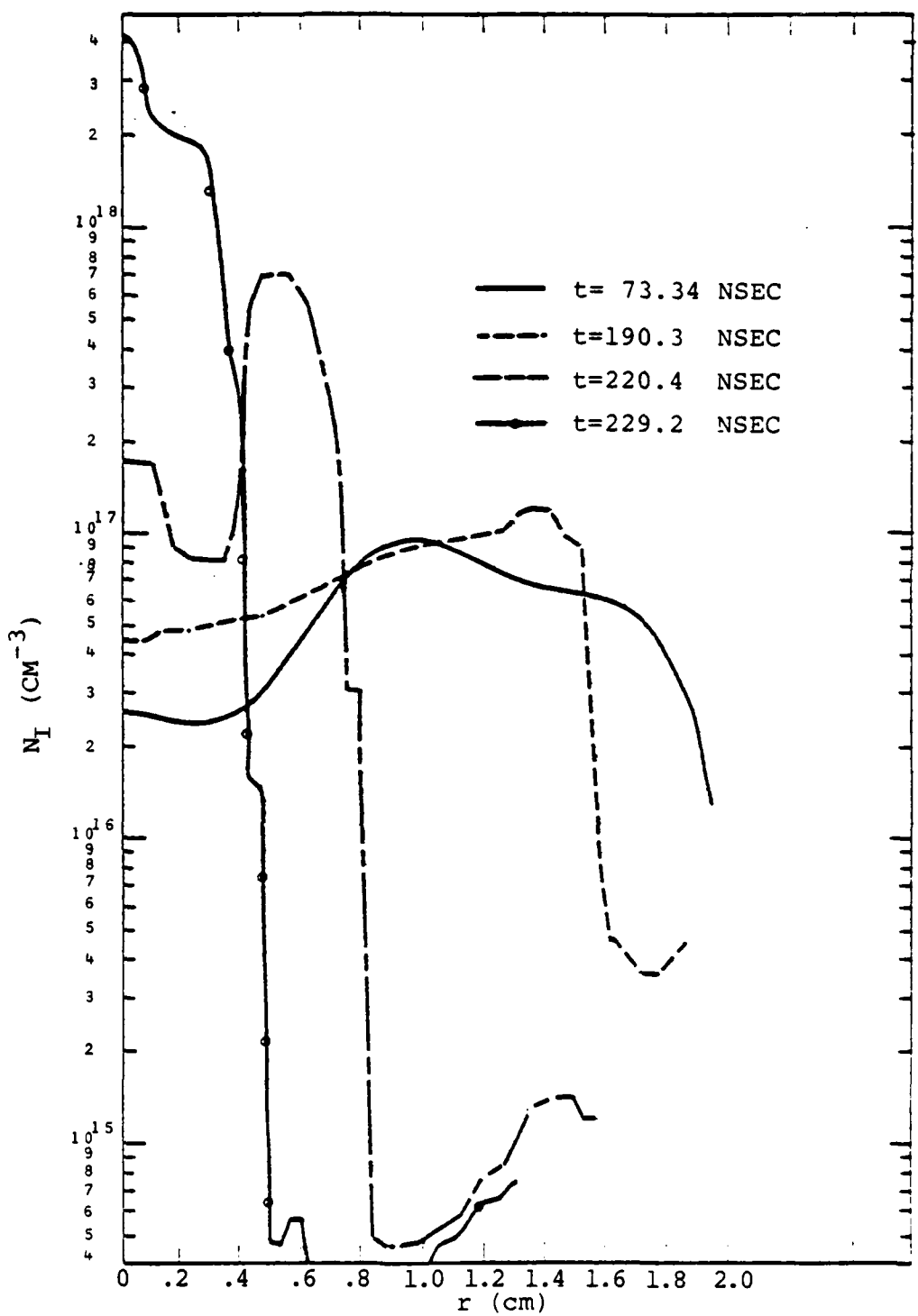


FIGURE 19: Radial Distribution of Ar ION Number Density

that the maximum time step over the first 170 nsec is 2.0 nsec and after this the timestep re-adjusts to accomodate local changes proportional to the net radial plasma velocity, plasma sound speed, etc. Indeed, time steps near the region of maximum beam collapse can get to as low as  $10^{-11}$  sec.

As is seen from Figure 18 the total zonal width decreases somewhat with time; a maximum electron temperature of over  $10^5$  eV is achieved at  $\sim 230$  nsec which is close to the initial collapse time. The illustrated temperatures are high due to the neglect of higher ionization states in the radiation-chemistry subroutine; nevertheless, reference to the  $N_I$  distributions illustrated in Figure 19 show that the temperature peaks are close to the steep density dropoff regions. This is representative of a core-corona model with the high density, somewhat cooler region surrounded by a higher temperature, strongly radiating, lower density annular zone. The radially quadratic  $\eta_1$  distribution (here with B, the time factor, equalling  $10^{-4}$ ) is seen to have some physical validity. Maximum  $N_I$  density levels exceeding  $10^{18} \text{ cm}^{-3}$  correspond to  $\eta_e$  values between  $10^{19}$  and  $10^{20} \text{ cm}^{-3}$ , which seem to be present in the P.I. experiment (private communication from P. Burkhalter).

Figure 20 illustrates the simple Ar model radiative power (in arbitrary units), versus time results with separate distributions for line, continuum, and  $h\nu > 1 \text{ keV}$  line

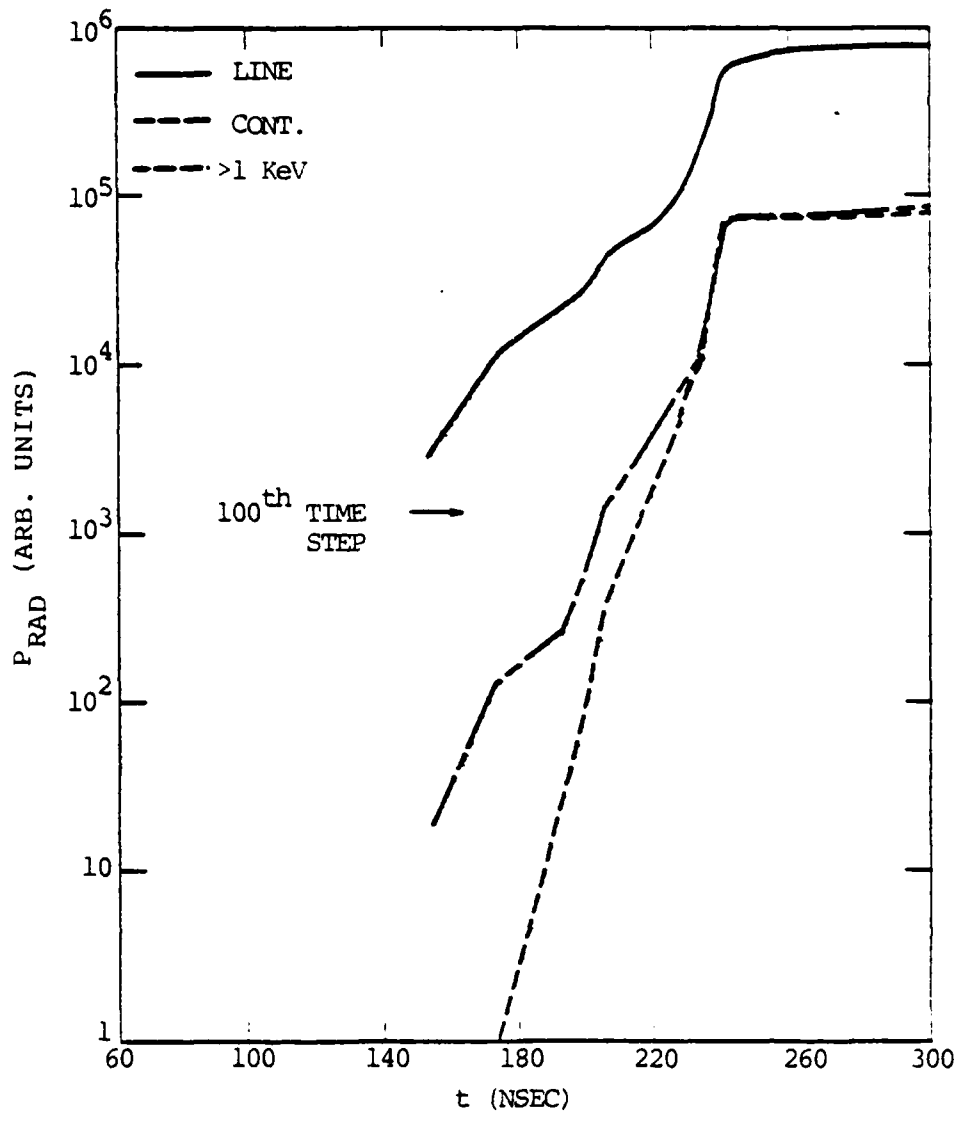


FIGURE 20: Radiative Power Outputs

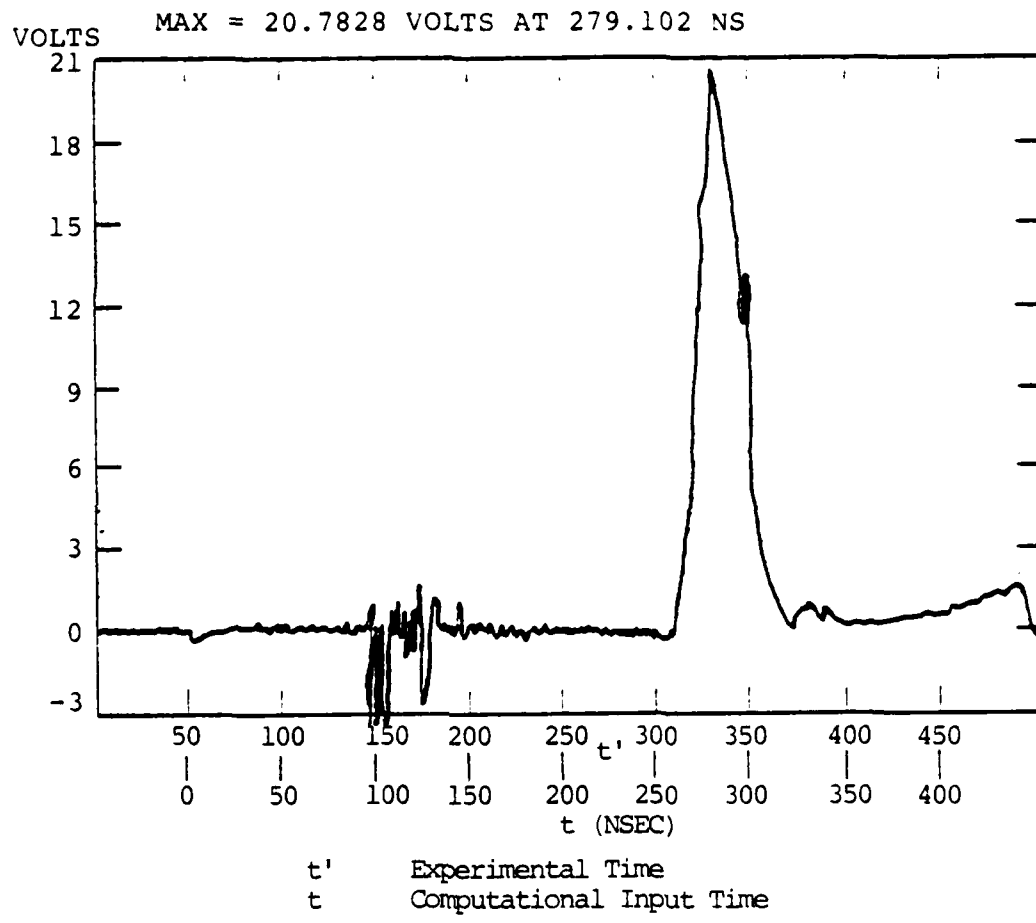


FIGURE 21: Experimental K-Radiation  
Time - Dependent Output

radiation. Computation of these values initiate at the one hundredth time step. The timewise distribution of the radiative power can be compared with experimental  $\gamma$ -radiation emission, as shown in Figure 21. It is seen that the numerical results occur somewhat earlier than the experimental output; furthermore, the numerical distributions flatten out for over 50 nsec, which is not found experimentally. In reality, plasma dynamic instabilities may serve to break up and therefore extinguish the radiating pinch at times much beyond the maximum collapse point; WHIRAD is hydrodynamically insufficiently sophisticated to account for this.

The latest employment of WHIRAD is the coupling to a full L-shell representation of Ar within the MCCELL routines: 140 ground and excited electronic states with 12 possible ions are considered. Line radiation transport between all the ionic states, balanced across the radial cells as is seen from the above solutions using the more approximate ATPHYS package employed for Ar, about 40 spatial increments are necessary to adequately represent the collapsed discharge steep radial gradients) requires a formidable amount of computation. As an example, inclusion of full line and continuum transport costs about \$10 per time step on the Texas Instruments ASC vectorized computer, while an entire 500 time step computation using the ATPHYS ground state

radiation-ionization package costs around \$40. We feel that, at present, it is more cost effective to consider the appreciable simplifications of local radiation transport, i.e., line radiation is either locally absorbed within the same emission cell or completely escapes the plasma, or employ a simpler restricted excited state version of the MCCELL package. Effort has therefore been expended on a somewhat limited package that omits a number of the excited Z-shell states but adequately represents the bound-bound transport at the z-pinch plasma densities and at temperatures above 300 eV. It is assumed that continuum radiation dominates at lower temperatures. Similar considerations have been initiated with argon so that gas puff solutions can be made with a form of the MCCELL package.

#### ii. Conclusion

The combination of numerically coupled z-pinch and multi-cell radiation codes together with close correlation with available experimental data is well underway. The work is also closely integrated with other hydrodynamic-multi-cell combined codes so that significant commonality is present within the Plasma Radiation Group.

#### b Spherical Geometry

For pellet implosions, as opposed to z-pinches, spherical geometry is clearly preferable as a choice for a simple geometry which also provides realistic modelling of the physical processes. Extensive progress has been made during the performance period on the development of

a self-consistent spherical numerical radiation-hydrodynamic model for use in predicting emission from a moving, high density plasma. The advances in the radiation-hydrodynamic model include the capability to treat opacity effects, the creation of an argon plus DT model, the extension of the aluminum model to lower ionization stages, and a restart and graphics ability.

The radiation hydrodynamics model solves the time dependent hydrodynamic equations for the conservation of matter, momentum, and energy for a single temperature, single fluid plasma using a flux-corrected transport (FCT) algorithm, with electron thermal conduction effects being taken into account through a time-splitting of the energy equation. The energy equation also includes the effects of heating-cooling due to radiation transfer. The plasma is assumed to be in ionization equilibrium, with the ground and excited levels being calculated with a collisional-radiative equilibrium (CRE) model. During the performance period the ionization model for aluminum was extended from its original level structure containing excited states only for hydrogen-like, helium-like and lithium-like ions to include excited states, and hence line emission, from all K-shell and L-shell ions. In addition, an ionization model for argon, including excited states and line emission for hydrogen-like, helium-like, and lithium-like ions was developed.

The ability to take opacity effects into account has been incorporated into the model. Radiation transfer of both line and continuum photons are treated with the escape probability model of reference 5. This model allows for radiation interactions between all grid points used in the code. The escape probability model gives an accurate description of radiation transfer and is much faster than an angle and frequency dependent radiation transfer scheme.

The original numerical escape probability code was vectorized and optimized with a resulting increase in speed on the ASC computer of roughly a factor of 10. The run time for the code has been further reduced by treating only selected lines with the escape probability model, leaving the other lines to be treated in the optically thin limit. For lines which are always optically thin or for lines which are not important energetically or for diagnostic purposes, this is a reasonable procedure. For comparison purposes, a model for the continuum transport using a Rosseland mean opacity was also developed.

Numerous model calculations have been made during the course of the year for both aluminum and argon plus DT. One example of this is the study of the implosion and blow-off of a spherical solid aluminum shell. Figure 22 shows the aluminum K and L shell lines used. For this problem, line cooling was insignificant due to the high densities,

Figure 22

ATOMIC LEVEL STRUCTURE

<u>A1 XIII</u>	<u>A1 XII</u>	<u>A1 XI</u>	<u>A1 X</u>	<u>A1 IX</u>
$n = 2$	$2s^3S$	$2p$	$2s2p^3P$	$2s2p^24P$
$n = 3$	$2p^3P$	$3s$	$2s2p^1P$	$2s2p^22S, 2P, 2D$
$n = 4$	$2s^1S$	$3p$	$2p^23P$	$2s^23s^2S$
$n = 5$	$2p^1P$	$3d$	$2p^21D$	$2s^23p^2P$
	3 (sing)	4 (doub)	$2p^21S$	$2s^23d^2D$
	4 (sing)	5 (doub)	$2s3s^3S$	$2s2p3d^4P, 4D$
	5 (sing)	6 (doub)	$2s3p^3P$	$2s2p(3P)3d^2P, 2D, 2F$
	$2s2p^3P$	$1s2p^22D$	$2s3d^3D$	$2s2p(1P)3d^2P, 2D, 2F$
	$2p^23P$		$2s3s^1S$	$2s2p4d^4P, 4D$
			$2s3p^1P$	
			$2s3d^1D$	

<u>A1 VIII</u>
$2p^21S, 1D$
$2s2p^35S$
$2s2p^33S, 3P, 3D$
$2s2p^31P, 1D$
$2s^22p3d^3P, 3D, 3F$
$2s^22p3d^1P, 1D, 1F$
$2s2p^2(2D)3s^3D$
$2s2p^23d^5P$
$2s2p^2(4P)3d^3P, 3D, 3F$
$2s2p^2(2D)3d^3S, 3P, 3D, 3F$

<u>A1 VII</u>
$2s^22p^32P, 2D$
$2s2p^44P$
$2s2p^42S, 2P, 2D$
$2s^22p^23s^4P$
$2s^22p^23s^2D$
$2s^22p^23d^4P, 4D$
$2s^22p(3P)3d^2P, 2D, 2F$
$2s^22p(1D)3d^2S, 2P, 2D, 2F$

<u>A1 VI</u>
$2s^22p^41S, 1D$
$2s2p^53P$
$2s2p^51P$
$2s^22p^33s^3S, 3P, 3D$
$2s^22p^33s^1P, 1D$
$2s^22p^3(4S)3d^3D$
$2s^22p^3(2D)3d^3S, 3P, 3D, 3F$
$2s^22p^3(2D)3d^1P, 1D, 1F$
$2s^22p^3(2P)3d^3P, 3D, 3F$
$2s^22p^3(2P)3d^1P, 1D, 1F$

<u>A1 V</u>
$2s2p^62S$
$2s^22p^43s^2P$
$2s^22p^43s^2D$
$2s^22p^43s^2S$
$2s^22p^4(3P)3d^2P, 2D, 2F$
$2s^22p^4(1D)3d^2S, 2P, 2D, 2F$

<u>A1 IV</u>
$2s^22p^53s^3P$
$2s^22p^53s^1P$
$2s^22p^53p^1D$
$2s^22p^53p^3P$
$2s^22p^53d^3P, 1P$
$2s^22p^53d^3D$
$2s^22p^54s^3P$
$2s^22p^54s^1P$

<u>A1 III</u>
$2s^22p^63s^2S$
$2s^22p^63p^2P$
$2s^22p^64s^2S$
$2s^22p^64p^2P$
$2s^22p^64d^2D$
$2s^22p^64f^2F$

and line emission was post-processed. Figures 23 and 24 show temperature and density profiles respectively at various times. Figure 25 shows net cooling profiles. The solid shell compressed the low density aluminum filler in this calculation to a peak central density of roughly five times solid aluminum. Figures 26 and 27 show spectra at  $T = 4.4 \times 10^{-11}$  s (early in the evolution of the system before the shell has significantly been affected by the radiation absorbed) and Figures 28 and 29 show spectra at  $T = 2.34 \times 10^{-9}$  s (peak compression). It is clear from the comparison of Figure 26 and 28, and of 27 and 29 that the peak compression temperature is considerably higher than that for the earlier time. The figures highlight the great amount of detail carefully included in the model of the radiation field.

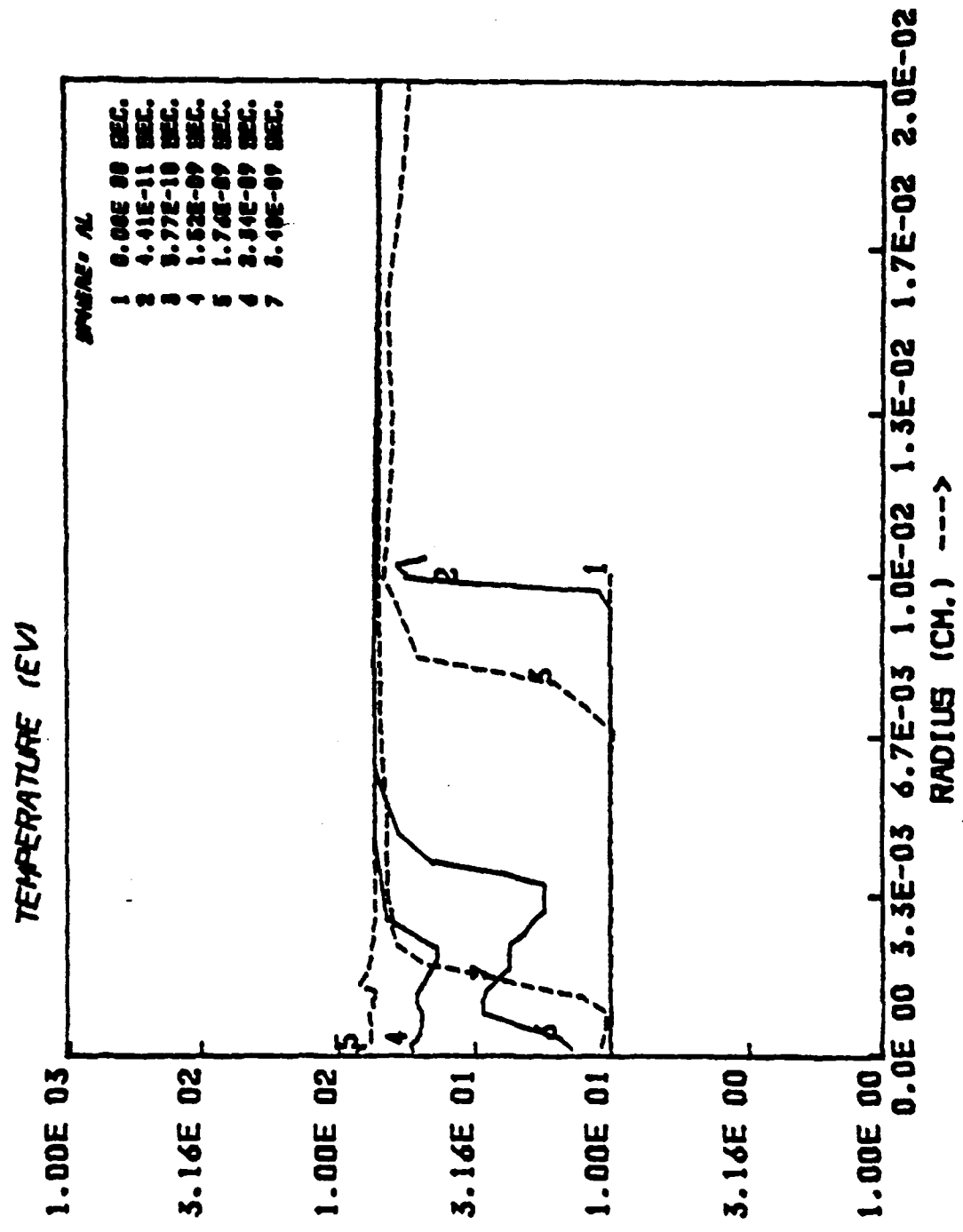


Figure 23

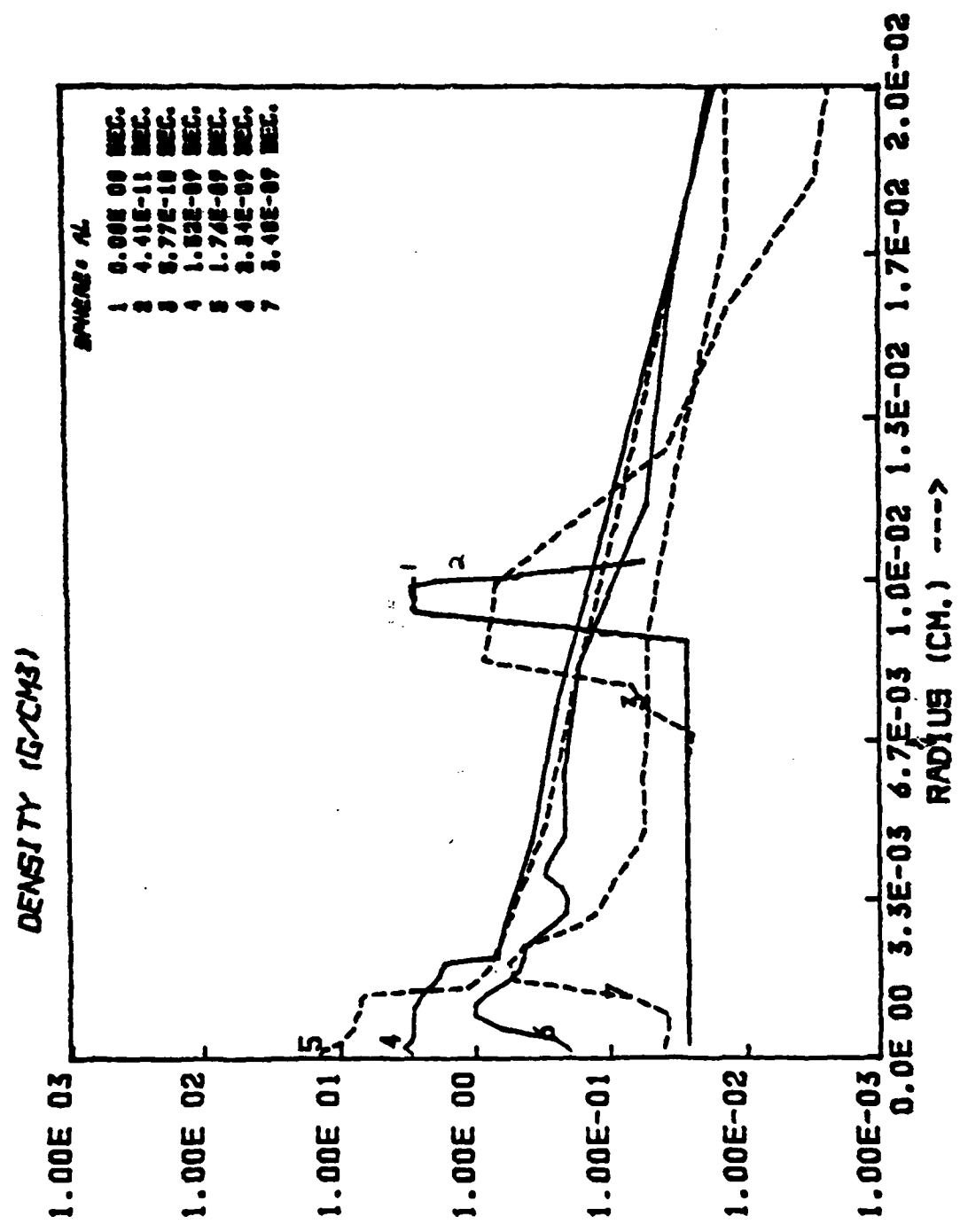


Figure 24

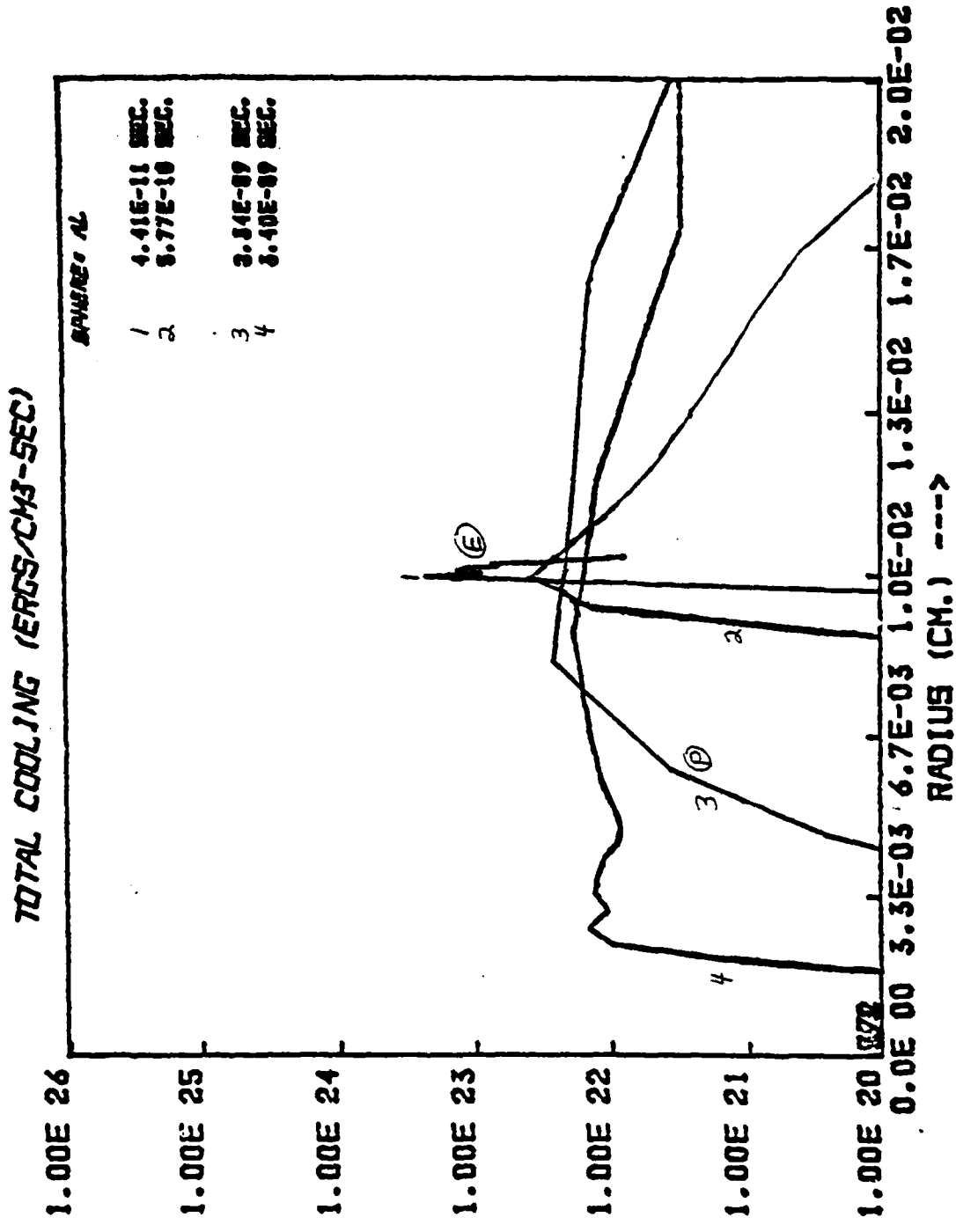


Figure 25

ALUMINUM SPECTRUM      INSTR. BROAD= 30 MA

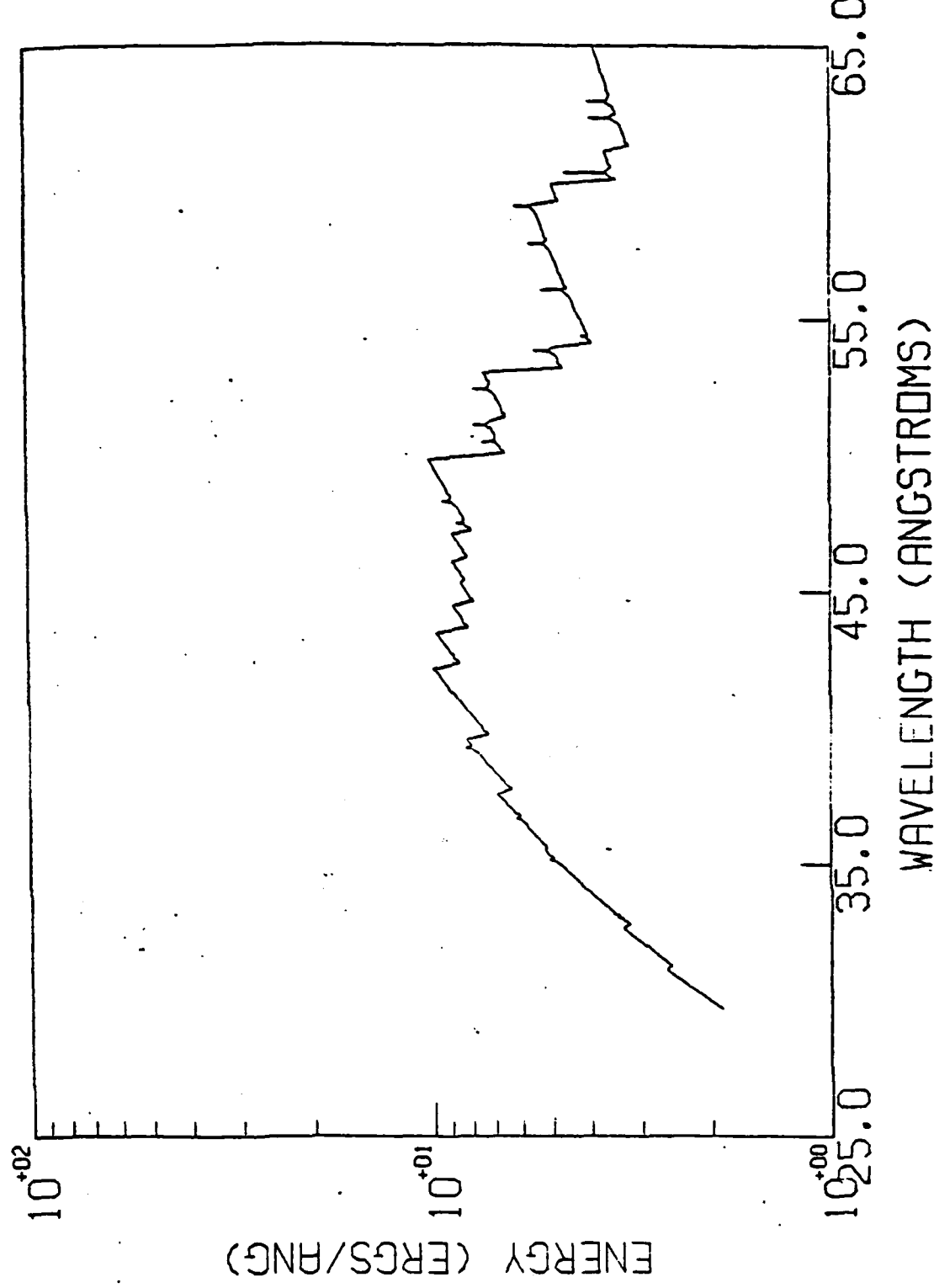


Figure 26

ALUMINUM SPECTRUM      INSTR. BROAD= 30 MA

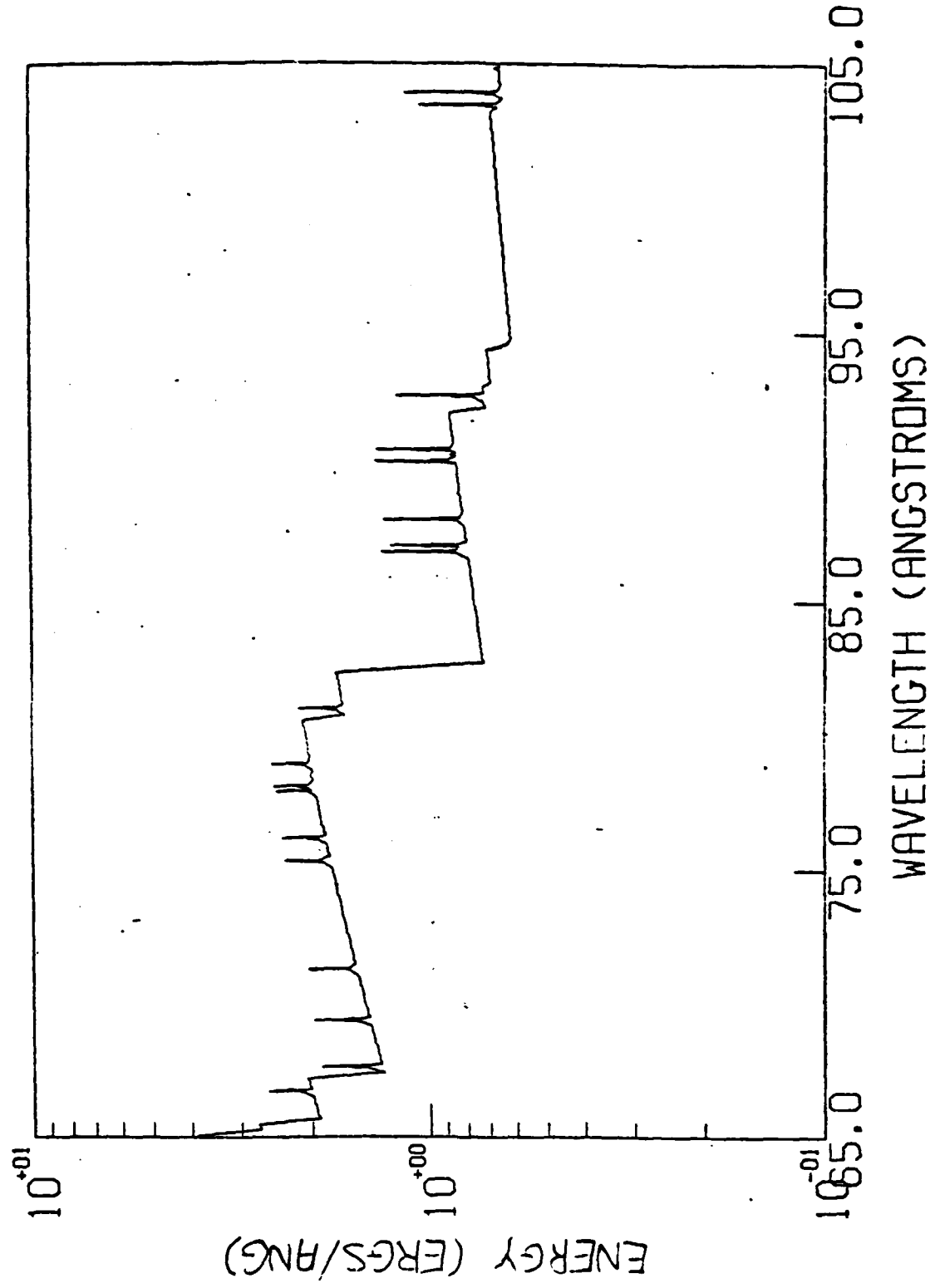


Figure 27

ALUMINUM SPECTRUM  
INSTR. BROAD= 30 MA

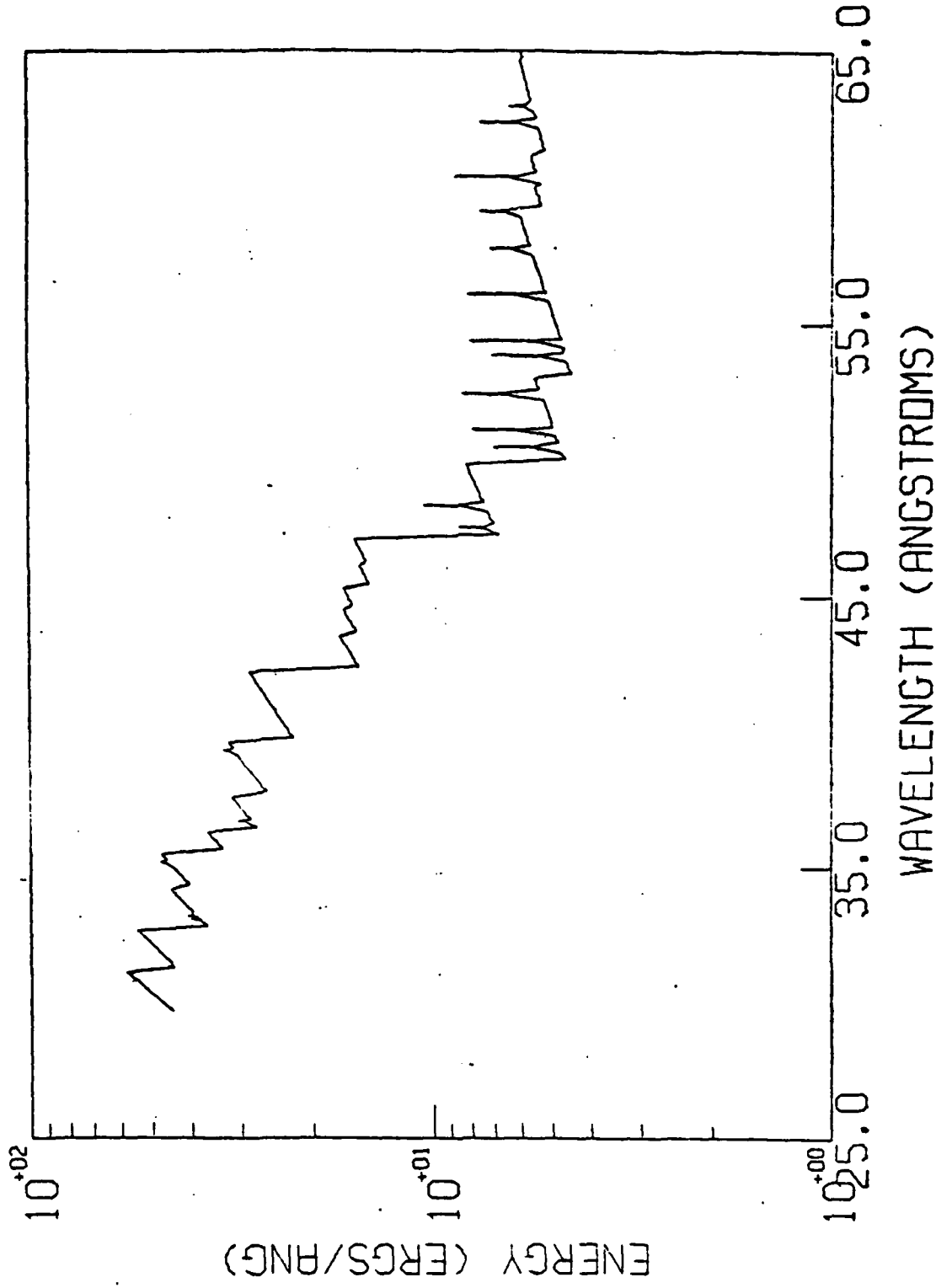


Figure 28

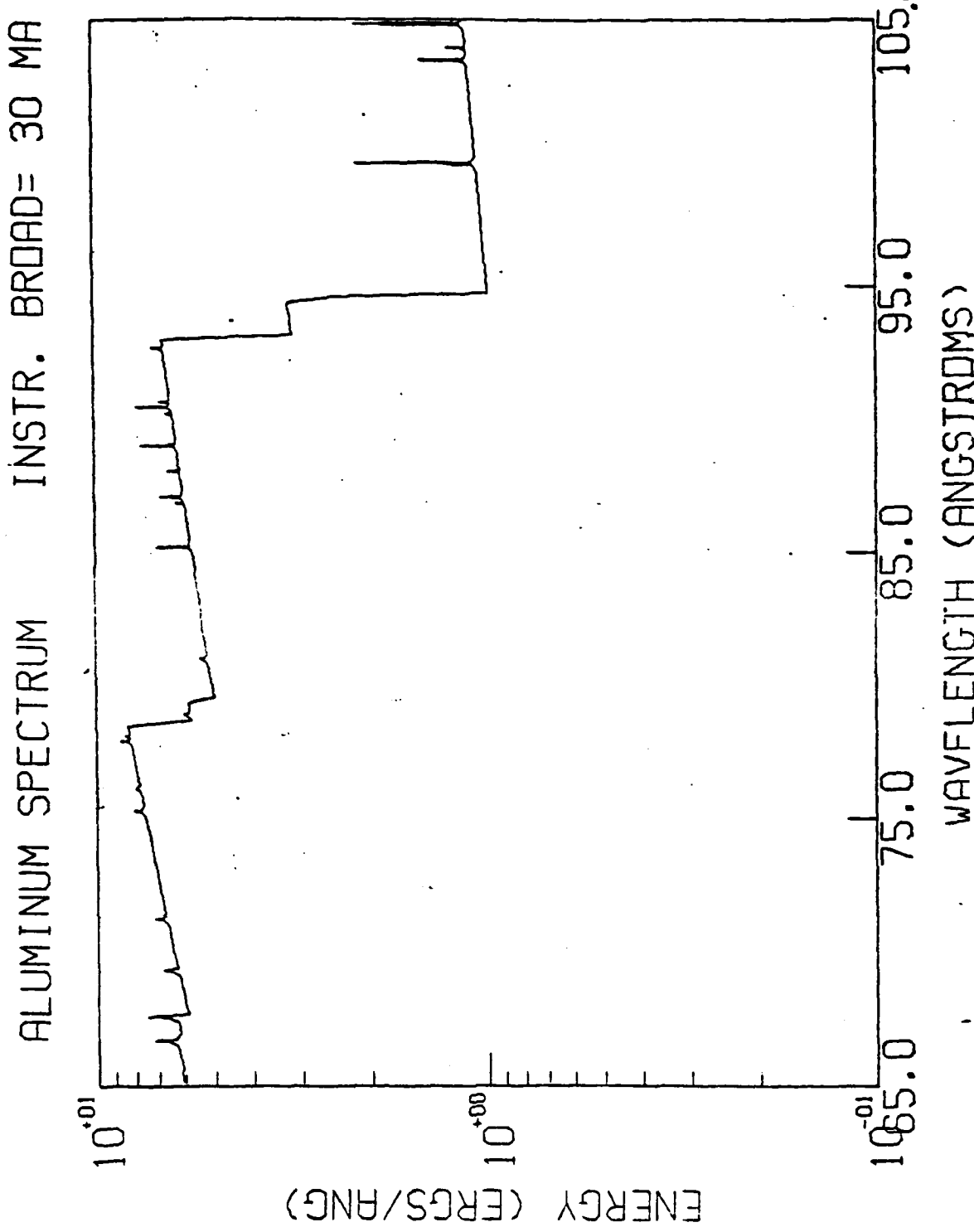


Figure 29

## II. REFERENCES

1. D. Duston and J. Davis, Phys. Rev. A, p 932 (1980).
2. D. Duston and J. Davis, Phys. Rev. A., p 1664 (1980)
3. P. B. Kunasz and D. G. Hummer, M.N.R.A.S. 166, p 57 (1974).
4. "Analysis of High Temperature Plasmas", SAI Report No. SAI-80-997-WA, 26 October 1979.
5. J. P. Apruzese, J. Davis, D. Duston and K. G. Whitney, J.Q.S.R.T. 23, p 479 (1980).
6. S. I. Braginskii, in Reviews of Plasma Physics, edited by M.A. Leontovich (Consultants Bureau, New York, 1965), page 205.
7. D. L. Book, Revised and Enlarged Collection of Plasma Physics Formulas and Data, NRL Memorandum Report 3332, May 1977.
8. J. P. Boris and D. L. Book, J. Computational Physics 11, p 38 (1973).
9. J. P. Boris, NRL Memorandum Report 3237, March 1976.

APPENDIX A

## Self-absorption of heliumlike satellite lines in high-density fusion plasmas

D. Duston\* and J. Davis

*Plasma Radiation Group, Plasma Physics Division, Naval Research Laboratory, Washington, D. C. 20375*

(Received 14 September 1979)

The high densities obtained in recent laser fusion experiments have created a need for additional plasma density diagnostics. The ratio of two heliumlike satellite lines, the  $1s2p\ 1P_1 - 2p\ 1P$  and  $1s2s\ 1S_0 - 2s2p\ 1P$  transitions, has shown promise as a spectral diagnostic when laser-imploded microballoons are seeded with medium-atomic-weight gases. In this study results are presented from a collisional-radiative ionization-dynamics model with photoexcitation processes included that indicate that the emission from these satellite lines is strongly affected by opacity in density and temperature regimes common to plasmas to which this diagnostic could be applied effectively. The radiation emission attenuated by photon reabsorption is presented for neon, aluminum, and argon plasmas and compared with results predicted when the calculation is undertaken in an optically-thin-plasma approximation. The opacity effects are seen to cause multivaluedness in the line ratio at several temperatures, and an overall loss of sensitivity if the ratio with density is predicted.

In recent years much work has been devoted to understanding radiation spectra emitted from dense high-temperature plasmas. Although most of the available experimental spectra have been obtained in the past from laser-produced plasmas,<sup>1</sup> exploding-wire plasmas,<sup>2</sup> or gas-puff Z pinches,<sup>3</sup> data have recently been obtained by seeding glass microballoons with a medium-Z gas to produce x rays from bound-bound transitions occurring during a high-temperature compression of an imploded pellet.<sup>4,5</sup> The purpose of these experiments is to make full use of the x-ray lines as diagnostic indicators of the temperature and density history of the plasma contained by the laser-imploded glass shell. Unfortunately, the densities being attained at present, typically  $10^{22}$ – $10^{23}$  electrons per cubic centimeter, are in a somewhat difficult regime for their determination. Several techniques are available to the experimentalist, e.g., Stark broadening of selected lines,<sup>6</sup> merging of the series limit,<sup>7</sup> and such selected line-intensity ratios as the intercombination-to-resonance line ratio in heliumlike ions.<sup>8</sup> In the past, these techniques have been applied to laboratory plasmas under the assumption that these lines are optically thin. However, the validity of the density determinations strongly depends on whether these high-density plasmas are indeed optically thin and, if not, whether opacity effects vitiate their usefulness as density diagnostics.

In this paper, a study is made of the radiation emitted by two doubly excited levels of the heliumlike ion which show up as satellite lines to the hydrogenlike resonance line, and the line ratio formed by them as used to determine the plasma density. The sensitivity range of this diagnostic extends over several orders of magnitude in ion

density, but is centered at approximately  $10^{21}$  ions/cm<sup>3</sup> for materials presently used for microballoon seeding, making it a logical candidate for application in density determinations of compressed-laser-pellet experiments. A theoretical calculation of this line emission as it is generated in optically thin neon, aluminum, and argon plasmas is performed. In addition, this line emission is also calculated in plasmas where photoexcitation is at least equally important as collisional excitation in order to assess the effect of opacity on the line-intensity ratio at high density.

### I. THEORETICAL MODEL

It has been shown from recent work<sup>1,2</sup> that, in the optically thin approximation, the line ratio under consideration is independent of the hydrogenlike ground-state population and depends only on the electron density, electron temperature, and atomic parameters associated with the levels being studied. We define an abbreviated level structure as shown in Fig. 1, and analytically calculate the line ratio in terms of the populations of the two doubly excited states of the heliumlike ion, the  $2s2p\ 1P$  and  $2s2p\ 3P$  levels, and their radiative transitions,  $1s2s\ 1S_0 - 2s2p\ 1P$  and  $1s2p\ 1P - 2p\ 3P$ .

First, the atomic rate equations for each of the doubly excited states are written

$$\begin{aligned} \frac{dN_1}{dt} &= C_1 N_e N_e + Y N_e N_2 - (\Gamma_1 + A_1 + X N_2) N_1, \\ \frac{dN_2}{dt} &= C_2 N_e N_e + X N_e N_1 - (\Gamma_2 + A_2 + Y N_1) N_2. \end{aligned} \quad (1)$$

Here,  $N$  denotes the state density,  $C$  is the electron-capture rate coefficient,  $\Gamma$  is the autoioniza-

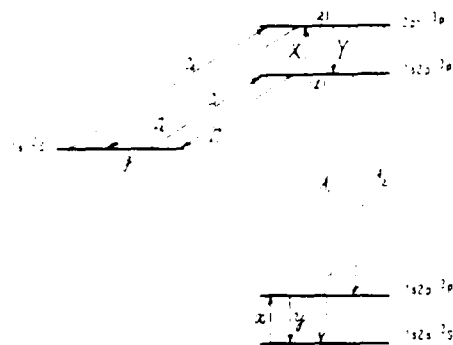


FIG. 1. Simplified level structure for analytic treatment of the satellite line emission from heliumlike ions.

zation rate,  $A$  is the spontaneous decay rate,  $X$  is the electron-excitation rate coefficient,  $Y$  is the deexcitation rate coefficient,  $N_e$  is electron density, and the subscripts  $g$ , 1, and 2 indicate the  $1s$ ,  $2s2p$ , and  $2p^2$  states, respectively. Note that at the densities under consideration here, the electron and ion collisional rates coupling the individual  $j$  components of each of the two doubly excited levels are sufficiently large that it is assumed that they will each be populated according to their statistical weights, allowing for their representation as the two  $n$  levels in Fig. 1 (the  $j$  degeneracy has been removed). Under the assumption that the atomic rates are faster than the typical hydrodynamic time scale of the plasma [collisional-radiative equilibrium (CRE) model], the time derivatives in Eq. (1) are set to zero and the solutions for  $N_1$  and  $N_2$  are given by

$$\begin{aligned} N_2 &= \frac{N_1 \theta_1 - N_e N_e C_1}{N_e Y}, \\ N_1 &= \frac{N_e N_e^2 C_2 Y + N_e N_e C_1 \theta_2}{\theta_1 \theta_2 - N_e^2 X Y}, \end{aligned} \quad (2)$$

where  $\theta_1 = A_1 + \Gamma_1 + X N_e$ , and  $\theta_2 = A_2 + \Gamma_2 + Y N_e$ . The line intensity is now given by  $N A \Delta E$ , where  $\Delta E$  is the transition energy. Forming the line ratio and solving from Eq. (2), one can readily show that

$$\begin{aligned} R &= \frac{N_2 A_2 \Delta E_2}{N_1 A_1 \Delta E_1} = \frac{A_2 \Delta E_2}{A_1 \Delta E_1} \frac{1}{Y N_e} \\ &\times \left( \theta_1 - \frac{\theta_1 \theta_2 - X Y N_e^2}{Y N_e (C_1/C_2) + \theta_2} \right) \end{aligned} \quad (3)$$

and hence the ratio is independent of  $N_e$ .

For this study, we have chosen to use the radiative decay and autoionization rates of Vainstein and Safronova<sup>11</sup> and average over the individual  $j$  components so as to be applicable to our

model. The electron-capture rate coefficient is obtained by detailed balance of the autoionization rate, giving, for example, for state 2.

$$C_2 = \Gamma_2 (g_2/2g_1) (2\pi\hbar^2/m_e kT_e)^{3/2} e^{-E_2/kT_e}, \quad (4)$$

where  $g$  is the statistical weight and  $E_2$  is the energy of the doubly excited state above that of the hydrogenlike ground state. The electron collisional excitation rate coefficient coupling the two levels has been calculated by the method of distorted waves,<sup>12</sup> and the deexcitation rate coefficient also obtained from detailed balance of the excitation rate coefficient

$$Y = X (g_1/g_2) e^{\Delta E/kT_e}, \quad (5)$$

where  $\Delta E$  is the energy separation of the two doubly excited states.

As a theoretical check on the calculation, approximations can be made in Eq. (3) to obtain the values for the ratio in the local thermodynamic equilibrium (LTE)<sup>13</sup> and corona limits.<sup>14</sup> In the LTE (high-density) limit, it is expected that collisional rates will dominate over competing radiative rates. Setting the  $A$ 's and  $\Gamma$ 's to zero in the large parentheses in Eq. (3), we obtain the LTE limit (noting that  $g_1 = g_2$ ),

$$R_{\text{LTE}} = \frac{A_2 \Delta E_2}{A_1 \Delta E_1} \frac{X}{Y} = \frac{A_2 \Delta E_2}{A_1 \Delta E_1} e^{-\Delta E/kT_e}. \quad (6)$$

In the corona limit, radiative processes are dominant over competing collisional rates. If we form the ratio  $N_2/N_1$  from Eq. (2) and let  $\theta_1$  go to  $\alpha_1 = A_1 + \Gamma_1$  and  $\theta_2$  go to  $\alpha_2 = A_2 + \Gamma_2$ , we get

$$\frac{N_2}{N_1} \cong \frac{\alpha_1}{N_e Y} - \frac{C_1}{Y} \frac{\alpha_1 \alpha_2 - N_e^2 X Y}{N_e^2 C_2 Y + N_e C_1 \alpha_2}. \quad (7)$$

Ignoring the  $N_e^2 XY$  term in the numerator, factoring out an  $\alpha_1/N_e Y$  term from the bracket, combining, and expanding out, assuming that  $C_1 \alpha_2 \gg N_e C_2 Y$ , we obtain the following expression in the corona limit:

$$R_{\text{cor}} \cong \frac{A_2 \Delta E_2}{A_1 \Delta E_1} \frac{\Gamma_2 (A_1 + \Gamma_1)}{\Gamma_1 (A_2 + \Gamma_2)} e^{-\Delta E/kT_e}, \quad (8)$$

where we have eliminated  $C_1, C_2$  using Eq. (4). It is expected that Eq. (6) and (8) will define the high- and low-density limits of the optically thin line ratios studied here; comparisons will be made in Sec. III.

## II. IONIZATION-RADIATION MODEL

In Sec. I, it was determined that the  $1s2p^1P - 2p^2^3P$  to  $1s2s^1S - 2s2p^1P$  line-intensity ratio was independent of the populations of surrounding ground or singly excited levels. If opacity effects are included in the model, this is not the

case. When the optical depths of the two satellite lines exceed 1, photoexcitation is expected to significantly affect the populations of the doubly excited states, coupling them to the lower states of the satellite-line transitions, the  $1s2s^3S$  and  $1s2p^3P$  levels. Although previous authors<sup>9,10</sup> have discounted radiative absorption processes in forming this ratio with the argument that the lower states of the lines are excited states of the heliumlike ion and are expected to be well down in population from the ground state, and hence generate small optical depths for these lines, we have found this not to be the case at densities and temperatures where the line ratio is expected to be a valuable diagnostic. Hence some means must be included in the calculation to take account of radiative transfer and photoexcitation when the satellite lines become optically thick.

As a basis for these calculations, we use an atomic model based on rate equations describing the processes populating ground states and selected excited states for each element studied. The processes in this model include collisional ionization; collisional, radiative, and dielectronic recombination; collisional excitation; collisional and spontaneous radiative deexcitation; and stimulated absorption and emission. The equations are solved time independently for a homogeneous plasma of constant electron temperature and ion density to yield fractional populations of the states, electron density, and line-emission intensities self-consistently with the radiation-transport calculations.

The photon-absorption processes are taken into account by a phenomenological frequency-diffusion model which allows an emitted photon to escape an absorbing plasma by successive collisions with ions, eventually scattering into the optically thin wings of a broadened line profile and escaping the plasma. A photon-trapping factor can be calculated as a function of the optical depth through the plasma at a frequency corresponding to the line-center frequency of the photon transition. This factor can thus reduce the line source function depending on the opacity of the plasma. It is also included in the rate equations to allow for the optical pumping of the upper levels of thick lines. The optical depth of the line is defined as

$$\tau_\nu = \frac{\pi e^2}{m_e c} f_{1k} \frac{\bar{L}}{\sqrt{\pi}} \frac{N_L}{\Delta\nu_D} \varphi(\nu), \quad (9)$$

where the Doppler width is given by

$$\Delta\nu_D = (2 T_i / M c^2)^{1/2} \nu_0. \quad (10)$$

Here,  $f$  is the dipole oscillator strength,  $\bar{L}$  is the

effective photon path length through the plasma,  $N_L$  is the lower-state population,  $\varphi$  is the line profile function,  $T_i$  is ion temperature, and  $M$  is the ion mass. In order to accurately determine the  $N_L$ 's and hence, the optical depths, a number of excited states were included in the atomic model in addition to all the ground states: the  $n = 2, 3, 4, 5$  levels in the hydrogenlike ion, the  $2s^1S, 2s^3S, 2p^1P, 2p^3P$ , 3-singlet, 4-singlet, and 5-singlet levels in the heliumlike ion, and the  $2p, 3s, 3p, 3d$ , and  $4d$  levels in the lithiumlike ion. A complete discussion of the method of calculating rate coefficients, atomic structure, and the opacity model has been presented in previous studies.<sup>15,16</sup>

### III. RESULTS

#### A. Optically thin approximation

In order to obtain a clear understanding of the role played by collisions in determining this intensity ratio, and also to compare our predictions with previous work, an initial study of the formation of the level populations in the optically thin approximation was undertaken. Hence no reabsorption of photons and subsequent optical pumping was allowed in obtaining these first calculations. Since it has been shown in Sec. II that the line ratio is independent of all but the  $2s2p$  and  $2p^2$  populations in an optically thin plasma, the results are merely the solution to Eq. (3). The ratio is depicted graphically in Figs. 2-4 for neon, aluminum, and argon plasmas, shown at various temperatures over a wide range of ion densities. As can be seen from the figures, each plasma produces the same basic behavior in the line ratio: a relatively constant low- and high-density limit, connected by a rapidly ascending transition region over which the ratio provides its diagnostically valuable density dependence.

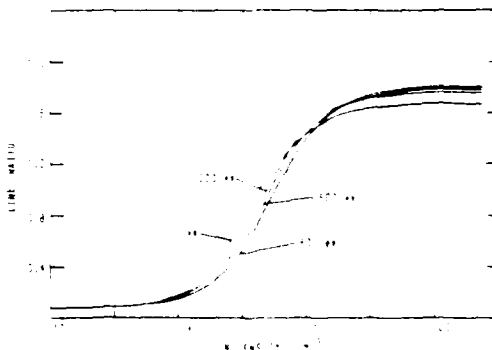


FIG. 2.  $(1s2p^3P \rightarrow 2p^1P) / (1s2s^3S \rightarrow 2s2p^3P)$  intensity ratio for a neon plasma in the optically thin approximation.

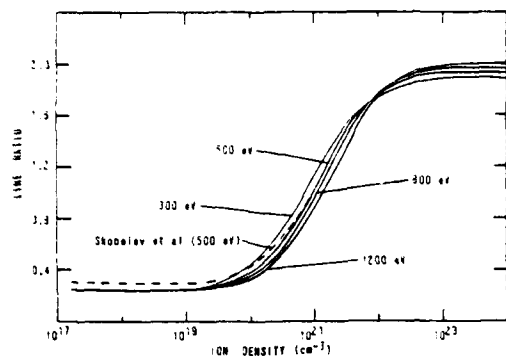


FIG. 3.  $(1s2p^3P - 2p^2^3P)/(1s2s^3S - 2s2p^3P)$  intensity ratio for an aluminum plasma in the optically thin approximation.

The  $2s2p$  level is preferentially populated over the  $2p^2$  level at low densities since the ratio of the radiative decay rate to the autoionization rate for the  $2s2p$  state is smaller than that of the  $2p^2$  state. However, the electron collisions coupling these two states become increasingly important in the redistribution of the populations as the plasma electron density increases, resulting in an increase in the  $2p^2$  level relative to the  $2s2p$  level and a corresponding increase in the line-intensity ratio. Finally, in the high-density limit, the two levels reach a state of statistical equilibrium relative to each other with the population ratio given by  $e^{-\Delta E/\Gamma_0}$  and the line ratio given by Eq. (6).

Note that for purposes of density diagnostics in laser-imploded pellets doped with a small amount of neon, the most effective region for density predictions is from  $3 \times 10^{19}$  to  $3 \times 10^{21}$  ions/cm<sup>3</sup>, while for argon-seeded pellets, the region is from  $5 \times 10^{20}$  to  $5 \times 10^{22}$  ions/cm<sup>3</sup>. Thus, with the ap-

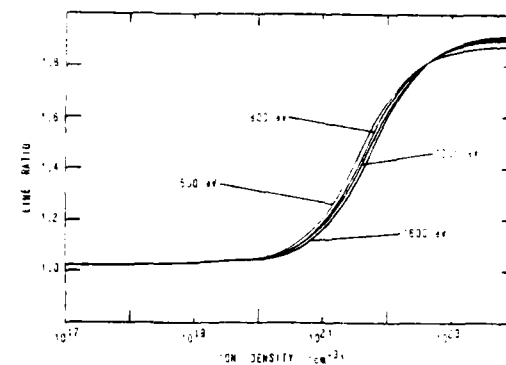


FIG. 4.  $(1s2p^3P - 2p^2^3P)/(1s2s^3S - 2s2p^3P)$  intensity ratio for an argon plasma in the optically thin approximation.

propriate gas doping, it is conceivable that this technique would be an effective diagnostic over three orders of magnitude in density, provided the pellet fuel can be heated sufficiently to attain temperatures where the satellite-line emission is intense enough to be measured.

Also shown in Fig. 3 are the results of an earlier work by Vinogradov *et al.*<sup>9</sup> The model used in Ref. 9 leading to their predicted line ratio was applied to an aluminum plasma and the ratio calculated for an electron temperature of 500 eV. In fact, Ref. 9 includes only the emission from four transitions in the  $2p^2-1s2p$  manifold ( $^3P_2-^3P_1$ ,  $^3P_2-^3P_0$ ,  $^3P_1-^3P_0$ ,  $^3P_1-^3P_2$ ) for experimental reasons, while our calculation includes all six of the components (the  $^3P_1-^3P_2$  and  $^3P_0-^3P_1$  in addition to the four above) from the  $2p^2$  state. The curve reflects the calculation from Ref. 9, however, with all six lines included, and is seen to be in excellent agreement with our CRE model predictions.

In order to verify that our calculations approach

TABLE I. Atomic parameters used in the collisional radiative model to analyze the heliumlike satellite-line structure.

Parameter	Neon	Aluminum	Argon
$\lambda_1$ (Å)	12.307	7.252	3.763
$\lambda_2$ (Å)	12.323	7.26	3.766
$\Delta E_1$ (eV)	1007.4	1709.6	3294.56
$\Delta E_2$ (eV)	1006.1	1707.8	3292.46
$\Delta E$ (eV)	8.64	11.7	18.74
$J_1$	0.3935	0.3974	0.4036
$J_2$	0.2390	0.2657	0.2639
$A_1$ (sec <sup>-1</sup> )	$5.776 \times 10^{12}$	$1.68 \times 10^{13}$	$6.347 \times 10^{13}$
$A_2$ (sec <sup>-1</sup> )	$1.05 \times 10^{13}$	$3.362 \times 10^{13}$	$1.241 \times 10^{14}$
$\Gamma_1$ (sec <sup>-1</sup> )	$1.353 \times 10^{13}$	$1.357 \times 10^{13}$	$1.387 \times 10^{13}$
$\Gamma_2$ (sec <sup>-1</sup> )	$4.287 \times 10^{11}$	$1.987 \times 10^{12}$	$1.352 \times 10^{13}$
$R_{LTE}$ (500 eV)	1.73	1.953	1.985
$R_{cor}$ (500 eV)	0.100	0.244	1.031

the correct limits, the values for the satellite-line ratio in the LTE and corona approximations were determined in accordance with the parameters given in Table I and Eqs. (6) and (8). Comparison between the values obtained in Table I at electron temperatures of 500 eV and Figs. 2-4 generated by our model also indicates good agreement.

### B. Optically thick plasma

At low plasma densities, optical depths of emission lines are small, as defined by Eq. (9), and, consequently, the photon-absorption effects are small relative to competing collisional and spontaneous radiative rates and can be neglected. As the plasma density increases, the photoexcitation rates become comparable or even exceed competing processes, resulting in significant changes in the population densities of the excited states and the subsequent bound-bound radiation emission from these levels. In previous studies, the effects of these processes on the determination of the hydrogenlike satellite-line ratio have been ignored with the justification that the lower state of each of the relevant transitions is itself an excited level, and hence the populations of these levels should not be large enough in the density range of interest to contribute to a large optical depth in plasmas of the physical dimensions commonly encountered in the laboratory.

In order to test the validity of this assumption, we performed calculations of the line ratio using our radiation-ionization dynamics model with frequency-diffusion radiation transport in a way similar to those for the optically thin approximation presented above. The implementation of an expanded level structure in the model is necessary if the population densities of the lower states of each transition are to be determined accurately, self-consistently with other states of the heliumlike ion, as well as with the excited and ground states of neighboring ions.

As was mentioned, the line source function in an opaque plasma is attenuated by a factor dependent on the optical depth and on the mechanism by which the emission line is broadened. In this study, we have chosen to describe the optically thick line shape by a Voigt line profile, taking into account the collisional and radiative broadening of both the upper and lower levels comprising the transition of interest. At very high densities, Stark profiles are necessary to describe the line shape accurately. This problem is currently being addressed by Jacobs and Davis, but no profiles have been calculated as of this writing.

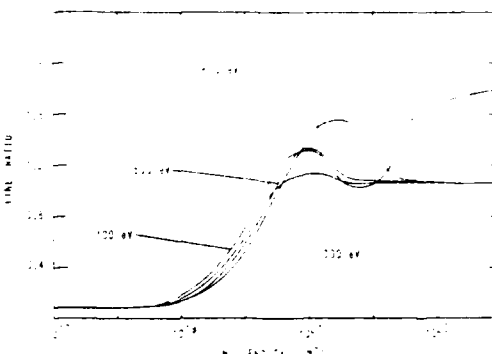


FIG. 5.  $(1s2p^3P - 2p^3P)/(1s2s^3S - 2s2p^3P)$  intensity ratio for a neon plasma of radius  $100 \mu\text{m}$ —with opacity effects.

The results of the calculations with opacity effects included are presented in Figs. 5-7 for a neon, aluminum, and argon plasma, respectively. The studies were performed for plasmas with a radius of  $100 \mu\text{m}$  over a range of ion densities and electron temperatures identical to those used for studying this line ratio in the optically thin approximation (Figs. 2-4).

Upon comparison of the three figures, certain aspects of the calculation for each different plasma are seen to be similar, and can be discussed in terms of a general plasma radiating in this temperature and density regime:

(i) The line ratio exhibits, initially, a decrease relative to the optically thin result, which occurs at an ion density somewhat higher than that at which departure from the coronal result takes place. Evidently, the  $1s2p - 2p^2$  line intensity must be affected by opacity at a lower density than the  $1s2s - 2s2p$  intensity, despite the fact that the former has an oscillator strength roughly two-thirds of the latter transition. This effect



FIG. 6.  $(1s2p^3P - 2p^3P)/(1s2s^3S - 2s2p^3P)$  intensity ratio for an aluminum plasma of radius  $100 \mu\text{m}$ —with opacity effects.

can be understood in terms of the lower-state population densities as determined by the collisional radiative model. At the densities at which the opacity effects first manifest themselves, the lower state of the former transition, the  $1s2p^3P$  level, is more populated than the lower state of the other transition, the  $1s2s^1S$  level, owing to the strong collisional mixing of these levels at these large electron densities. The ratio of the statistical weights is 3:1, but the ratio of these populations ranges, typically, from 2:1 to 3:1 above  $10^{19}$  ions/cm<sup>3</sup>, as is determined by the actual collisional and radiative rates employed in our model. Referring to Eq. (9), therefore, the optical depth at line center for the  $1s2p - 2p^2$  transition will be approximately 1.3–1.9 times greater than that of the  $1s2s - 2s2p$  transition, and, consequently, will experience photon reabsorption at a lower density, resulting in the initial decrease in the line ratio. Hence, accurate collisional and radiative rates are necessary for a model to accurately predict the ion density at which deviations from the optically thin approximation will first appear.

(ii) The line ratio will exhibit this initial decrease owing to opacity, in general, at a higher density for a higher-temperature plasma. For example, in Fig. 6, the aluminum plasma will yield a line ratio which begins to flatten out at  $10^{21}$  ions/cm<sup>3</sup> for the 300-eV case, but this doesn't occur until  $3 \times 10^{21}$  ions/cm<sup>3</sup> for the 800-eV plasma. This effect is simply a manifestation of the ion temperature dependence of the optical depth, which can be seen, in Eq. (9), to fall off as  $T_i^{1/2}$ . Deviations from this effect can occur at low temperature, however, as is seen in Fig. 5 for a neon plasma at 100 eV and in Fig. 7 for an argon plasma at 500 eV. The departure from the optically thin result occurs at higher densities than

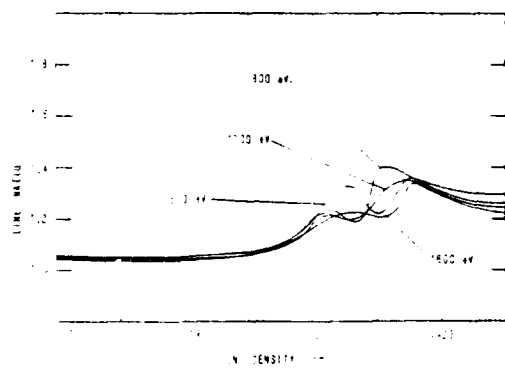


FIG. 7.  $(1s2p^3P - 2p^13P)/(1s2s^1S - 2s2p^1P)$  intensity ratio for an argon plasma of radius 100  $\mu\text{m}$ —with opacity effects.

it does for the higher-temperature plasmas. What is occurring at lower temperatures is a major change in the abundance of the heliumlike-ion populations. Over a wide range of temperature (at constant ion density) the heliumlike ion is the dominant ion population in the plasma<sup>16</sup>; hence the  $1s2s^1S$  and  $1s2p^3P$  densities will be large. At low temperatures, however, these densities fall rapidly, yielding to lower stages of ionization; consequently, the optical depths of the two transitions also decrease rapidly, delaying the onset of the opacity effects until higher densities, in spite of the lower-temperature plasma effect described above.

(iii) The line ratio will converge, at high densities, to an LTE limit significantly different from that predicted by the calculation when done in the optically thin approximation. Although the upper-state populations of the two transitions will eventually relax to the same LTE ratio (1:1) in the high-density limit regardless of the opacity effects (collision-dominated plasma regime), the radiation emission will be quite different from the optically thin prediction. This can be demonstrated by using an approximate analytic model,<sup>15</sup> in which the radiation is attenuated by a factor  $\gamma$ , where<sup>17,18</sup>

$$\gamma \propto (a/\tau_0)^{1/2}, \quad (11)$$

where  $a$  is the Voigt damping parameter, proportional to the sum of all collisional and radiative rates depopulating the upper and lower levels of the transitions. From Eq. (6) the LTE line ratio in the optically thick case now becomes

$$R_{\text{LTE}}(\text{thick}) = R_{\text{LTE}}(\text{thin})(\gamma_2/\gamma_1). \quad (12)$$

Now, from Eq. (9),  $\tau_0$  is proportional to the oscillator strength and the lower-state densities, giving

$$\gamma_2/\gamma_1 = (a_2 f_1 N_{1s2s} / a_1 f_2 N_{1s2p})^{1/2}, \quad (13)$$

where

$$f \propto (g_u/g_l) A \lambda^2 \quad (14)$$

( $u$  and  $l$  refer to upper and lower states) and, in the LTE limit,

$$N_{1s2s}/N_{1s2p} \approx g_{1s2s}/g_{1s2p}. \quad (15)$$

Noting that the wavelengths are approximately equal and inserting the appropriate statistical weights, one obtains

$$R_{\text{LTE}}(\text{thick}) = R_{\text{LTE}}(\text{thin}) (a_2 A_1 / a_1 A_2)^{1/2}. \quad (16)$$

At high densities, the parameter  $a$  is dominated by collisional rates; we have calculated the required electron-collisional excitation rates (de-

TABLE II. Electron collisional excitation and deexcitation rate coefficients which dominate the collision broadening of the satellite lines.

Transition		Neon ( $10^{-3}$ )	Aluminum ( $10^{-3}$ )	Argon ( $10^{-3}$ )
300 eV	X	5.7	2.7	1.43
	Y	5.87	2.81	1.52
	x	7.7	3.5	0.463
	y	2.6	1.24	0.173
500 eV	X	4.53	2.13	1.14
	Y	4.61	2.18	1.18
	x	6.1	2.82	0.47
	y	2.1	9.65	0.168
800 eV	X	3.63	1.71	0.914
	Y	3.67	1.73	0.936
	x	4.87	2.27	0.460
	y	1.64	7.70	0.16

excitation is obtained by detailed balance) using our distorted-wave approximation,<sup>13</sup> and the dominant rates are those depicted in Fig. 1 as X, Y, x, and y and are listed in Table II. Over the range of temperatures studied here, the ratio  $a_2/a_1$  is determined to be nearly constant at high densities (see Table II) with values of 0.63 for neon, 0.64 for aluminum, and 0.8 for argon. Using the values given in Table I and Eq. (16) we obtain, for the LTE line ratio in the optically thick case, 1.05 for neon, 1.105 for aluminum, and 1.2 for argon, which are seen to agree quite favorably with the model results in Fig. 5-7. Small discrepancies occur in the case of argon since (i) the ratio  $a_2/a_1$  is not strictly constant with temperature owing to the dominance of the doubly excited-state mixing rates (see Table II), and (ii) the argon plasma has not yet reached a state of complete LTE at  $10^{24}$  ions/cm<sup>3</sup> (see Fig. 7).

Although several features of the line ratio in the various plasmas are similar, there are still some contrasting features apparent in the optically thick results. The most obvious physical effect, although only a slight one, is the increase in the density at which opacity effects occur with atomic number Z, as seen in Fig. 5-7. This finds explanation in the actual scaling of electron collisional excitation rate coefficients, which decrease in magnitude at threshold with Z. A decrease in the populating rates at a given density corresponds to a decrease in excited-level densities and, consequently, the optical depths of the transitions of interest here. Thus at  $10^{21}$  ions/cm<sup>3</sup> and a nominal electron temperature of 800 eV, the  $1s2p\ ^3P$  state of aluminum will be more populated than the same state of a similar argon plasma. Hence, the optical depth of the  $1s2p\ ^3P - 2p^2$  transition will be "thicker" in the aluminum plasma

than in the argon plasma, and opacity effects will occur at a lower density.

In Fig. 5, the optically thick line ratio for the neon plasma at 100 eV displays rather anomalous behavior at high densities. What is occurring here is a high-density effect decreasing the abundance of the heliumlike neon ion until the satellite lines are no longer optically thick and the ratio rises to its optically thin LTE limit, an effect similar to the one described earlier due to low plasma temperature. Simply stated, an increase in ion density at constant temperature usually drives a plasma toward a state of lower ionization.<sup>15</sup> Once again, the heliumlike ion, owing to its "closed-electron-shell" configuration, maintains a relatively large population density over a wide range of densities. However, at high enough densities, particularly at low temperatures, the ion abundance shifts toward lower charge states rapidly, generating a corresponding drop in excited-state populations and resulting in a line-ratio behavior as seen in Fig. 5. The same behavior would be seen for aluminum and argon if curves for lower temperatures had been of interest in this work. However, the onset of this behavior in a laboratory plasma would usually be accompanied by a significant decrease in the line intensities, making this diagnostic inaccurate at these densities due to its weak appearance in the spectra.

The most striking difference between the optically thick results for the three plasmas, however, is seen as a single shoulder or "hump" in neon, the absence of a shoulder in aluminum, and a double shoulder in argon. Although many factors affect the line-ratio behavior as have been discussed in detail above, the Z scaling of the value of the LTE optically thick limit and the density at which LTE is reached are most important

in determining this shape. For the argon plasma, in Fig. 7, the "double hump" occurs as, first, the  $1s2p - 2p^2$  intensity is attenuated by opacity, decreasing the ratio; second, the  $1s2s - 2s2p$  transition becomes thick, attenuating that line intensity and thus increasing the ratio; third, the plasma becomes collision dominated, the line ratio tends toward its LTE limit, and this limit is lower than the value the ratio has attained before entering the LTE regime, causing the ratio to decrease and creating the second hump. In the aluminum plasma in Fig. 6, LTE is reached before the second shoulder can manifest itself, and the LTE value for the ratio is approximately equal to the value the ratio has attained before LTE is reached, allowing for only a very mild shoulder structure, most apparent at 1200 eV. For the neon plasma, in Fig. 5, the LTE state is also reached at relatively lower densities, but the LTE value of the line ratio is much lower than the value the ratio has attained before entering the LTE state, hence a single pronounced "hump" is evident.

Since the occurrence of these shoulders and the value of the LTE limit of the line ratio seem to be strongly dependent on the actual atomic parameters of the particular plasma of interest, prediction of a general shape would seem difficult in light of the many ways the parameters in Table I scale with  $Z$ . Unfortunately, this seems to indicate that each element requires, to a certain extent, individual treatment if this line ratio is to be applied successfully to diagnose laboratory plasmas in which photoexcitation is an important process.

#### IV. DISCUSSION

We have studied the heliumlike-satellite line-intensity ratio with our sophisticated collisional-radiative ionization-dynamics model in order to assess, within the context of an optically thick plasma, the value of this ratio as a plasma density diagnostic in the high-density, high-temperature plasma regime encountered in recent laser-pellet interaction experiments. The behavior of the line ratio was first examined under the assumption of an optically thin plasma. It was found that the density profile of the line ratio was independent of ion-state populations in this approximation. In addition, it was found that the density-sensitive range of the line ratio occurred at higher densities with increasing atomic number, extending the range of applicability of this diagnostic, depending on the choice of the fill gas. The results were compared with other independent work and with limiting values deter-

mined from simple analytic models, and in all cases the agreement was quite favorable.

Armed with confidence in the model and understanding gained from the optically thin analysis, we proceeded to investigate the effects of stimulated absorption and emission on these plasmas by "turning on" the opacity calculation. The most obvious result from this study was that, indeed, the satellite-line ratio from plasmas of this type was affected by opacity, despite the fact that the lower levels of the two transitions are excited states of the heliumlike ion. Not only did the deviations from the optically thin result occur at densities where the diagnostic is most sensitive and useful, but many of the line ratios were multiple valued with density, making accurate diagnostics difficult. As further analysis illustrated, the actual shape and overall behavior of the line ratio versus density was a sensitive function of the atomic parameters pertaining to the individual plasma. This finding led to two inescapable conclusions: (a) accurate theoretical modeling of this diagnostic in the "thick" case depends on a comprehensive level structure within the CRE model and accurately determined cross sections characterizing the collisional processes linking the level structure, and (b) owing to the complex interaction of the various atomic parameters in determining the level populations and radiation field, and the various  $Z$  dependencies of these parameters, simple  $Z$  scaling of the line-ratio behavior in a reabsorbing plasma is not likely; rather, each plasma will have to be characterized individually.

In light of the results obtained for the intensity ratio with photoexcitation processes included in the calculation, it would appear that opacity effects may cause some departure from optically thin results at densities presently encountered in pellet-fusion experiments. The extent of this departure, of course, will depend on the initial fill pressure of the admixture. By using very low fill pressures, the density of the additive gas at peak compression will be below the density at which opacity effects commence to affect the ratio; however, the trade-off is in the reduced number of emitting ions, resulting in emission lines with intensities which may be too low to measure accurately with existing spectroscopic methods.

To determine the degree of the self-absorption effects in typical microballoon experiments, a parameter study has been done for neon and argon where the source size has been scaled with the density as  $N^{-1/3}$ . Plasma radii were determined by using the law of mass conservation and a set of initial conditions chosen to model actual micro-

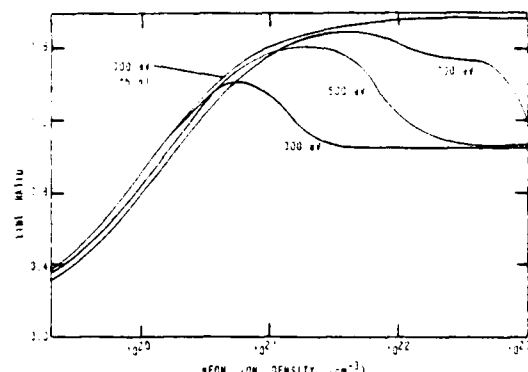


FIG. 8.  $(1s2p^3P \rightarrow 2p^23P)/(1s2s^3P)$  intensity ratio for a neon plasma corresponding to initial conditions of a  $180\text{-}\mu\text{m}$ -diam microballoon with 1 atm of neon and 9 atm of DT.

balloon experiments. For the neon study, a balloon diameter of  $180\text{ }\mu\text{m}$  and fill pressures of 1 atm of neon and 9 atm of deuterium-tritium (DT) (10% neon gas, by volume) were chosen as typical initial conditions.<sup>5</sup> The argon study was modeled after recent experiments<sup>19</sup> which employed  $230\text{-}\mu\text{m}$ -diam glass shells with fill pressures of 0.4 atm of argon and 30 atm of DT. While the DT gas does not affect the neon satellite-line radiation directly, the increase in electron density due to the ionization of the DT atoms will affect the collisional dynamics which determine the level populations of the impurity ions, and must be taken into account. This results in an increase in the electron density by factors of approximately 2 and 7 for neon and argon, respectively, compared to that of the seed gas alone at the temperatures for which the study was done.

In Fig. 8, the results of the neon study are shown for electron temperatures of 300, 500, and 700 eV, along with the optically thin result at 300 eV plotted versus neon-ion density. Similarly, the argon results at 600, 800, and 1200 eV with an optically thin curve for 600 eV are shown in Fig. 9 versus argon-ion density. The effect of photo-excitation is seen to cause departure from the

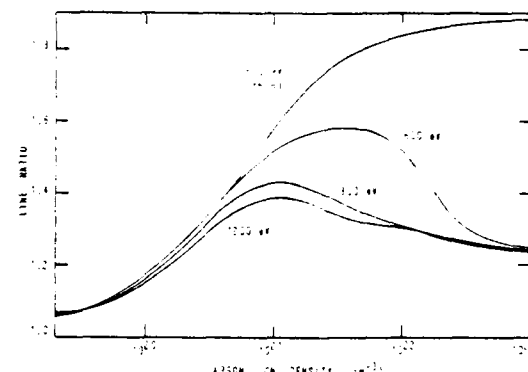


FIG. 9.  $(1s2p^3P \rightarrow 2p^23P)/(1s2s^3S \rightarrow 2s2p^3P)$  intensity ratio for an argon plasma corresponding to initial conditions of a  $230\text{-}\mu\text{m}$ -diam microballoon with 0.4 atm of argon and 30 atm of DT.

thin result at implosion diameters of between 20 and  $30\text{ }\mu\text{m}$  in the case of neon and at a diameter of about  $45\text{ }\mu\text{m}$  for argon, representative in both cases of compression volumes attainable by existing systems. Clearly, the optically thin results are not accurate at higher compressions.

The final point of this discussion which we would like to emphasize is the necessity for comprehensive, detailed calculations of spectral signatures when attempting to determine parameters from these laboratory plasmas. Opacity effects on the radiation emission need not render the spectrum useless for diagnostic purposes; multi-valuedness, as seen in Fig. 8 and 9, need not mitigate line-intensity ratios for applicability in deciphering the plasma-radiation signature. No single density or temperature indicator should be relied on, but rather, searching for consistency among several radiation diagnostics in the spectrum is required in order to draw accurate conclusions regarding the general plasma state.

#### ACKNOWLEDGMENTS

This work was supported by the Defense Nuclear Agency. One of us (D. D.) was supported by an NRC-NRL Resident Research Associateship.

<sup>\*</sup>Present address: Science Applications, Inc. McLean, Va. 22101.

<sup>†</sup>D. J. Nagel, P. G. Burkhalter, C. M. Dozier, J. F. Holzrichter, B. M. Klein, J. M. MacMahon, J. A. Stamper, and R. R. Whitlock, Phys. Rev. Lett. 33, 743 (1974).

<sup>‡</sup>P. G. Burkhalter, J. Davis, J. Rauch, W. Clark, G. DalBaca, and C. Stallings, J. Appl. Phys. 50, 705 (1979); P. G. Burkhalter, C. M. Dozier, and D. J.

Nagel, Phys. Rev. A 15, 700 (1977).

<sup>§</sup>P. G. Burkhalter, J. Shiloh, A. Fisher, and Robert D. Cowan, J. Appl. Phys. 50, 4532 (1979).

<sup>¶</sup>B. Yaakobi, D. Steel, E. Thorsos, A. Hauer, and B. Perry, Phys. Rev. Lett. 39, 1526 (1977).

<sup>||</sup>K. B. Mitchell, D. B. van Hulsteyn, G. H. McCall, Ping Lee, and H. R. Griem, Phys. Rev. Lett. 42, 228 (1979).

<sup>¶</sup>Hans R. Griem, Milan Blaha, and Paul C. Keppe,

- <sup>1</sup>Phys. Rev. A 19, 2421 (1979).
- <sup>2</sup>J. Davis, NRL Memorandum Report 2655, October 1973 (unpublished).
- <sup>3</sup>A. V. Vinogradov, I. Yu. Skobelev, and E. A. Yukov, Sov. J. Quantum Electron. 5, 630 (1975).
- <sup>4</sup>A. V. Vinogradov, I. Yu. Skobelev, and E. A. Yukov, Sov. Phys. JETP 35(5), 925 (1977); I. Yu. Skobelev, A. V. Vinogradov, and E. A. Yukov, Phys. Scr. 18, 78 (1978).
- <sup>5</sup>John F. Seely, Phys. Rev. Lett. 42, 1606 (1979).
- <sup>6</sup>L. A. Vainshtein and U. I. Safronova, At. Data Nucl. Data Tables 21, 50 (1978).
- <sup>7</sup>J. Davis, P. C. Kepple, and M. Blaha, J. Quant. Spectrosc. Radiat. Transfer 16, 1043 (1976).
- <sup>8</sup>J. Richter, in *Plasma Diagnostics*, edited by W. Lochte-Holtgreven (North-Holland, Amsterdam, 1968).
- <sup>9</sup>R. W. P. McWhirter, in *Plasma Diagnostic Techniques*, edited by R. H. Huddlestone and S. L. Leonard (Academic, New York, 1965).
- <sup>10</sup>D. Duston and J. Davis, NRL Memorandum Report 3846, September 1978 (unpublished).
- <sup>11</sup>D. Duston and J. Davis, Phys. Rev. A (to be published).
- <sup>12</sup>R. G. Athay, *Radiation Transport in Spectral Lines*, (Reidel, Dordrecht, Holland, 1974), Chap. 2.
- <sup>13</sup>J. P. Apruzese, J. Davis, and K. G. Whitney, J. Quant. Spectrosc. Radiat. Transfer 17, 557 (1977).
- <sup>14</sup>A. Hauer (private communication).

APPENDIX B

## Line emission from hot, dense, aluminum plasmas

D. Duston\* and J. Davis

Plasma Radiation Group, Naval Research Laboratory, Washington, D. C. 20375

(Received 30 July 1979)

The radiation emission from dense, high-temperature aluminum plasmas has been studied to appraise the influence of photoexcitation on several spectral diagnostics currently used to determine average plasma parameters. The plasma state is described by a set of collisional-radiative rate equations characterizing the competing atomic processes occurring in a homogeneous plasma volume of constant density and temperature. Radiation is transported through the plasma by the method of frequency diffusion, a technique which employs collision times of the photons as they diffuse through the wings of a broadened line profile. Line spectra and line-intensity ratios for several pairs of emission lines of the K shell are calculated in optically dense plasmas and compared with those obtained from the model within the optically thin approximation. The radiation-trapping effects are shown significantly to modify the behavior of the optically thin constant-density or constant-temperature line ratio curves, which become double valued in some cases. Comparisons of state populations obtained from this model and the local-thermodynamic-equilibrium model are also shown.

## I. INTRODUCTION

It has been suggested from recent experiments<sup>1,2</sup> in which moderate-*Z* plasmas have been heated to high temperatures at high density, that the resulting radiation emission may play an important role in the dynamic evolution of the plasma temperature and density profile. The extent to which the radiation may represent a significant energy-loss mechanism is a moot question,<sup>3</sup> but clearly, resonance reabsorption of emitted photons in an optically thick medium will both redistribute the plasma energy, spatially and spectrally,<sup>4</sup> and can alter significantly the radiation signature at the diagnostic detectors.

In an effort to provide theoretical insight into some of the effects of radiation and ionization on the plasma development, several atomic models have recently been developed<sup>5-9</sup> which take into account the various processes occurring in high-temperature plasmas and which ultimately affect the radiation emission. While a complete theoretical analysis of the radiation dynamics and its interplay with other basic plasma processes requires a full-scale, detailed, time-dependent model coupling ionization dynamics with magneto-hydrodynamics, we feel that the atomic processes leading to the radiation emission are sufficiently complex that a better understanding of the radiation physics would be more realizable if the model were limited, initially, to the basic ionization and radiation processes, in the absence of convection.

In this work, we present results from our radiation-ionization model as applied to the problem of diagnostics in a dense high-temperature aluminum plasma, with the notion that systematic trends in the emission features calculated from

this model will lead to conclusions about the nature of the radiating plasma. These results will be compared with those obtained from different physical models as well as with other investigations.<sup>9-11</sup>

## II. MODEL PREDICTIONS

The ionization-dynamic model employed in this study is similar to our earlier model.<sup>3,12,13</sup> A general set of time-dependent atomic rate equations are solved for a stationary volume element of plasma, homogeneous in temperature and total ion density. Each equation describes the population and depopulation of a particular ion (atom) species as determined by rate coefficients characterizing the various collisional events the particles experience. Such an equation, in the absence of convection, would be

$$\frac{dN_i}{dt} = \sum_j W_{ji} N_j - \sum_j W_{ij} N_i, \quad (1)$$

where  $W_{ij}$  is the rate describing a transition from state  $i$  to  $j$  (in sec<sup>-1</sup>). Each ground state and excited level in the model is represented by an equation of the form given by (1). The collisional and radiative processes are described by the rate  $W_{ij}$ . The model currently includes the following atomic processes: Collisional ionization, collisional (3-body), radiative (2-body), and dielectronic recombination, collisional excitation, collisional and spontaneous radiative de-excitation. The collisional ionization rates were calculated using a prescription suggested by Seaton,<sup>14</sup> and the radiative recombination rate coefficients were calculated by the detailed balance of photoioniza-

tion rates<sup>15</sup> employing effective Gaunt factors.<sup>16</sup> The dielectronic recombination rate coefficients are those calculated by Jacobs *et al.*,<sup>17</sup> while the spontaneous decay rates were taken from the NBS tables<sup>18</sup> or from oscillator strength extrapolations.<sup>19</sup> The electron collisional-excitation rate coefficients were calculated in the Born approximation<sup>19</sup> for the hydrogenlike transitions and by the distorted-wave method<sup>20</sup> for the heliumlike and lithiumlike transitions. The rates for the collisional processes from higher to lower energy states were calculated by the detailed balance of the corresponding upward collisional rate coefficients.

The processes of photoexcitation and stimulated emission are taken into account by a phenomenological transport model which allows photons to escape from an optically thick plasma by scattering into the optically thin wings of the absorption line profile. The photon-loss rate depends upon the optical depth of the plasma,

$$\tau_\nu = \frac{\pi e^2}{m_e c} f_{ij} \frac{L N_i}{\sqrt{\pi \Delta \nu_D}} \varphi(\nu), \quad (2)$$

where  $f$  is the line oscillator strength,  $N_i$  is the lower-state density, and  $\varphi$  is the line-profile function; the Doppler width is given by

$$\Delta \nu_D = (2 T_i / M c^2)^{1/2} \nu_0, \quad (3)$$

where  $T_i$  is the ion temperature,  $M$  is the ion mass, and  $\nu_0$  is the line-center frequency. The effective photon path length across the plasma is given by  $L$ ; in this way an average measure of the spatial extent of the optically thick plasma is taken into account. We can write an equation for the collisional processes undergone by photons in going from state  $j$  to state  $i$ , viz.,

$$\frac{dN_{ji}^*}{dt} = N_j A_{ji} + \frac{1}{t_s} N_{ji}^* \frac{g_i N_i}{g_j N_j} - \left( \frac{1}{t_s} + \frac{1}{t_e} \right) N_{ji}^*, \quad (4)$$

where  $A$  is the Einstein coefficient,  $N^*$  is the photon density, and  $t_s$  and  $t_e$  are scattering and escape times for the photon, respectively. The terms on the right-hand side of (4) describe spontaneous decay, stimulated emission, stimulated absorption and escape. We can rewrite Eq. (1) to include the photon transport terms,

$$\begin{aligned} \frac{dN_j}{dt} &= \sum_k W_{kj} N_k - \sum_k W_{jk} N_j \\ &+ \sum_{i < j} \left( \frac{1}{t_s} N_{ji}^* - \frac{1}{t_e} \frac{g_i N_i}{g_j N_j} N_{ji}^* \right). \end{aligned} \quad (5)$$

Assuming that the photon processes occur on a

time scale faster than the other collisional processes, the time derivative is set to zero in (4),  $N^*$  is solved for and substituted into (5), removing the  $A_{ji}$  term from  $W_{jk}$ . This yields the probability that a photon born at plasma center will escape to the outside ( $\lambda A$  times probability); an integration over  $r$  is then performed to average over all photons born throughout the plasma volume (with  $L$  replaced by  $r$  in the optical depth) to obtain

$$\gamma = \frac{1}{R} \int_0^R \left[ 1 + \frac{t_e}{t_s} \left( 1 - \frac{g_i N_i}{g_j N_j} \right) \right]^{-1} dr. \quad (6)$$

We incorporate this factor in the rate equations and in the radiation calculation,

$$P_\nu = h \nu N_{ji} A_{ji} \gamma. \quad (7)$$

Hence, both the attenuation of the radiation by opacity and the optical pumping effects on the level populations are included self-consistently. To evaluate  $\gamma$ , expressions for  $t_s$  and  $t_e$  have been derived as a function of the broadening mechanism influencing the line profile. For a naturally broadened line, the plasma is assumed to be optically thin,  $\tau < 1$ , and  $t_e = 0$ . For Doppler and Voigt line profiles, respectively the expressions can be used for  $t_e/t_s$ ,<sup>13, 21, 22</sup>

$$t_e/t_s = \begin{cases} \tau_0 (\pi \ln \tau_0)^{1/2} (1 + 1/2 \ln \tau_0) \\ 3(\tau_0/a)^{1/2} - 1, \end{cases} \quad (8)$$

where  $\tau_0$  is the optical depth at line center ( $\nu = \nu_0$ ) and  $a$  is a damping parameter given by

$$a_{ji} = \frac{\sum_k (A_{jk} + C_{jk}) + \sum_k (A_{ik} + C_{ik})}{4 \pi \Delta \nu_D}, \quad (9)$$

with  $C$  representing collisional rates. Hence, the Voigt profile is broadened by both collisional and radiative processes from emitting and absorbing states.

Preliminary studies of the radiation emission using these two broadening mechanisms indicate that under most plasma conditions, a Doppler line profile will result in more attenuation of line radiation than will a Voigt profile, primarily because photons can escape in the extended wing structure of the Voigt profile.

In order to test its validity, this method of radiation transport has been applied to a two-level atom for an infinite slab plasma medium<sup>23</sup> and the fluxes and radiation field departure coefficients compare quite favorably with Hearn's numerical solution of the exact radiation transport equation in this geometry.<sup>24</sup>

Aluminum was selected for study because of our

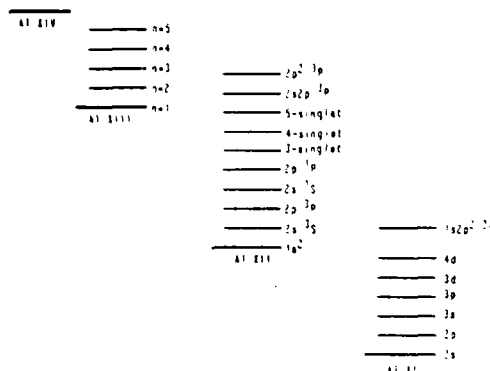


FIG. 1. Aluminum level structure used in the CRE model.

previous experience and understanding of aluminum models and the availability of experimental results.<sup>25-27</sup> Basic to any theoretical calculation of this kind is the atomic level structure; for aluminum we have included the 14 ground states, 4 excited levels in Al XIII ( $n = 2, 3, 4, 5$ ), 7 levels in Al XII ( $2s^2S, 2p^3P, 2s^1S, 2p^1P, 3\text{-singlet}, 4\text{-singlet}$ , and  $5\text{-singlet}$ ), and 5 levels in Al XI ( $2p, 3s, 3p, 3d, 4d$ ). In addition, we include 3 double-excited levels ( $2s2p^3P, 2p^23P, 1s2p^22D$ ) in order to study some prominent satellite lines in the spectra of high-temperature aluminum plasmas; the level structure is depicted in Fig. 1. Note that we have represented individual  $nl$  components of the hydrogenlike ion and the higher Rydberg levels of the heliumlike ion as single degenerate  $n$  states. The collisional rates by both ions and electrons which couple the  $\Delta n = 0$  transitions for these levels have been assessed in a previous work<sup>13</sup> and have been found to be sufficiently large over a wide range of densities and temperatures that the various  $l$  states are populated according to their relative statistical weights. Hence, for all Al XIII states and for  $n \geq 3$  in Al XII, we have previously averaged the rates which describe processes initiating or terminating on an individual  $nl$  level over all possible values of  $l$  for a given  $n$ , according to the statistical weights. Thus, the collisional-excitation rate from the  $1s^2$  state to the  $n = 3$  singlet level, for example, is obtained from the individual rates coupling the  $1s^2$  state to the  $3s, 3p$ , and  $3d$  singlet levels.

### III. RESULTS

#### A. Line spectrum from aluminum plasmas

One reason for performing calculations of this type is to predict level populations and radiation emission from a plasma characterized by elec-

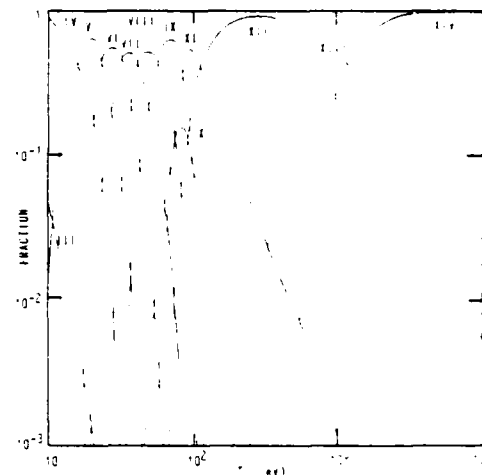


FIG. 2. Aluminum abundance curves vs electron temperature for an ion density of  $10^{20} \text{ cm}^{-3}$  (optically thin).

tron temperature, ion density, and size. As an example of the information obtained from our collisional-radiative equilibrium (CRE) model about state-density populations, an abundance curve showing the distribution of ionization-state populations as a function of temperature at a constant ion density of  $10^{20} \text{ cm}^{-3}$  in the optically thin approximation is shown in Fig. 2. The higher peaks corresponding to Al IV and Al XII are due to the large ionization energy of a closed-shell configuration. These peaks are usually broader in temperature indicating the propensity of the atom to remain in such a configuration. In Fig. 3, the "thin" abundances of Al XI-Al XIV are shown as a function of ion density for an electron temperature of 300 eV. Note that over a wide range of densities, the closed-shell Al XII ion is again the dominant species.

A typical x-ray spectrum as calculated by our

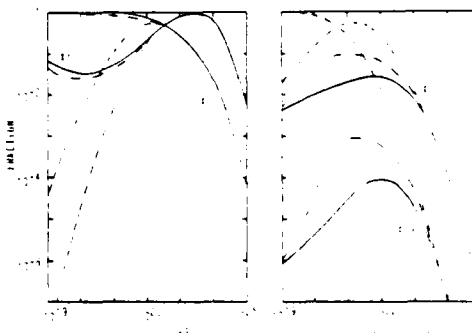


FIG. 3. Aluminum abundance curves vs ion density for an electron temperature of 300 eV: CRE-thin (-), CRE-thick (- - -), LTE (---).

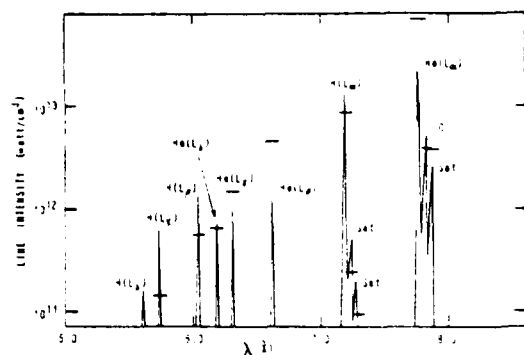


FIG. 4. Aluminum line emission spectrum, 5-8 Å, for an ion density of  $10^{20} \text{ cm}^{-3}$ , electron temperature of 500 eV and radius of 100  $\mu\text{m}$ .

model is shown in Fig. 4 and the corresponding vacuum ultraviolet (vuv) spectrum in Fig. 5, for a plasma at 300 eV, a density of  $10^{20} \text{ ions/cm}^3$  and a radius of 100  $\mu\text{m}$  for a Voigt profile. All lines in Fig. 4 decay to the 1s or 1s<sup>2</sup> ground-state levels, whereas, in Fig. 5, all transitions terminate on an n=2 level. The AlXII Balmer series lines, e.g., He (2p <sup>1</sup>P-3<sup>1</sup>S), are actually a manifold of the p-s and p-d transitions, but since levels with principle quantum number greater than 2 are considered as degenerate in our model, only their combined intensities are shown in Fig. 5. Also notice the satellite structure to the long-wavelength side of the hydrogenlike and heliumlike resonance lines; these satellites are due to the transitions 1s 2s 1S-2s 2p <sup>3</sup>P, 1s 2p <sup>3</sup>P-2p <sup>3</sup>P, and 1s<sup>2</sup> 2p <sup>3</sup>P-1s 2p <sup>1</sup>D, and are important both as relatively strong emitters and as valuable plasma diagnostics.

In order to illustrate the significance of photoexcitation on the radiation emission of dense plasmas, we have indicated the line intensities for a plasma with identical equilibrium conditions, but

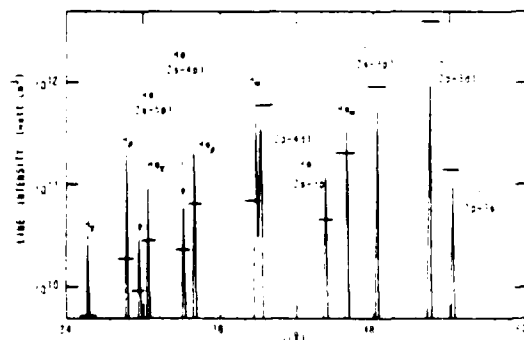


FIG. 5. Aluminum line emission spectrum 24-60 Å for an ion density of  $10^{20} \text{ cm}^{-3}$ , electron temperature of 500 eV and radius of 100  $\mu\text{m}$ .

calculated in the optically thin approximation by horizontal lines through the intensity spikes in Figs. 4 and 5. The differences are seen to range from a few percent, as in the case of the intercombination (IC) line, to more than an order of magnitude as with the H<sub>α</sub> line. In general, one would expect lines with large optical depths to experience a decrease in intensity due to the large photoexcitation cross section. This is, in fact, the case for the heliumlike Lyman lines and lithiumlike lines shown in the spectra, including the He(L<sub>α</sub>) satellite line. The intercombination transition is unaffected because, in spite of the fact that its lower level is a highly populated ground state, it has a rather small spontaneous decay coefficient ( $2.5 \times 10^{10} \text{ sec}^{-1}$ ), and hence, a relatively small optical depth ( $\tau_{\alpha} = 0.23$ ) compared to that of the heliumlike resonance line ( $\tau_{\alpha} = 83$ ).

The hydrogenlike and heliumlike Balmer-series lines show a universal increase in intensity when radiation trapping is included in the calculation. Since their lower states are excited states of the ions ( $n=2$  levels), their optical depths are small, and little photon reabsorption takes place. In addition, the Lyman-series lines are so optically thick that the power levels are "optically pumped" by the stimulated absorption process and the net effect of the increase in upper-state populations is a corresponding increase in intensities of the optically thin Balmer-series lines when opacity is included. Note, however, the He(L<sub>α</sub>) line; although it is a Lyman-series transition, and has an optical depth of about 2.4, the increase in the 5p population due to pumping more than compensates for the attenuation of the line intensity by photoabsorption.

An apparent contradiction to the above argument concerning lines with large optical depth is seen to occur in Fig. 4, where it is shown that the hydrogenlike Lyman-series lines are universally stronger in the thick calculation than in the thin, even though the optical depths of the α, β, and γ lines are 28.7, 4.6, and 1.6, respectively. In fact, these lines are somewhat attenuated by photoabsorption, but an actual increase in the thick intensities is caused by a significant enhancement of the Al XIII ground state by collisional ionization from the Al XII excited states, whose populations are now optically pumped. In order to verify this effect, a calculation was performed in which the radiation transport was "turned off" in the hydrogenlike ion. The intensity of the H(L<sub>α</sub>) line was then calculated to be over  $2 \times 10^{13} \text{ W/cm}^2$ , thus indicating that the states of Al XIII receive an increase in population from Al XII states in the optically thick case which exceeds the decrease in line intensity from the hydrogenlike Lyman lines

due to photon absorption. Hence, we have a case where it is possible that an optically thick transition may radiate at a *higher* intensity than would be calculated in an optically thin approximation, due to the strong collisional coupling between ions and significant optical pumping.

#### B. Diagnostic line ratios in the optically thin approximation

Spectral line intensity ratios are a valuable diagnostic tool employed by spectroscopists to determine the average temperature and density of the emitting region of a plasma. Although absolute line intensities are directly linked to the radiation source function, they are difficult measurements to make, requiring extremely accurate calibration of the detector. Taking the ratio of two emission lines eliminates some of the more difficult aspects of this calibration; in addition, if the two lines lie in the same region of the spectrum, technical problems due to nonlinearity of film or crystal response are lessened. We have chosen to study the behavior of five line ratios commonly used in the plasma community to diagnose laboratory and astrophysical plasma sources. The ratio of the hydrogenlike resonance line ( $1s-2p$ ) to the heliumlike resonance line ( $1s^2-1s2p^1P$ ) and the lithiumlike satellite line ( $1s^22p-1s2p^2D$ ) to the heliumlike resonance line are both used to determine electron temperature. Similarly, the ratio of the hydrogenlike resonance line to the heliumlike  $L_\alpha$  line ( $1s^2-1s3p^1P$ ) and the hydrogenlike  $L_\beta$  ( $1s-3p$ ) to the heliumlike  $L_\alpha$  ( $1s^2-1s5p^1P$ ) are temperature diagnostic ratios. Finally, the ratio of the heliumlike intercombination (IC) line ( $1s^2-1s2p^3P$ ) to the heliumlike  $L_\alpha$  is used to determine density.

In general, a good temperature diagnostic ratio is relatively insensitive to changes in density while the converse is true for a good density diagnostic ratio. We have plotted the density dependence of several of the ratios against ion density from cal-

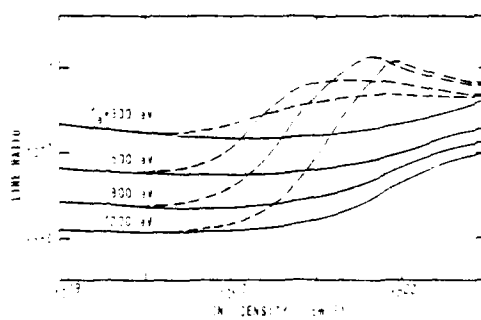


FIG. 6.  $1s^2 2p^2P - 1s2p^2D / 1s^2 - 1s2p^1P$  line ratio vs ion density; optically thin (-), optically thick with radius of 100  $\mu m$  (---).

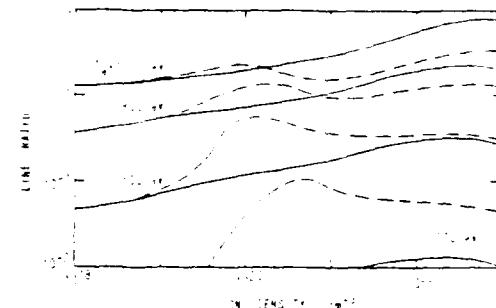


FIG. 7.  $1s-2p / 1s^2-1s2p^1P$  line ratio vs ion density; optically thin (-), optically thick with radius of 100  $\mu m$  (---).

culations done with the CRE model (as shown in Figs. 6-10); these calculations have been done assuming an optically thin plasma, temporarily neglecting reabsorption, in order to see the effects of particle collisions on the ratios as the plasma goes from a coronal to a collisional regime. The Al XII satellite to Al XIII  $L_\alpha$  ratio in Fig. 6 is relatively flat up to a density of  $10^{21}$  for the temperatures displayed. Above this density, the ratio increases due to a combination of two effects: The increasing ratio of Al XII ground-state population to Al XIII ground-state population and the strong collisional coupling between the Al XIII ground state and the  $1s2p^1P$  level. At low densities, both the  $1s2p$  Al XII state and the  $1s2p^2D$  Al XI state are strongly coupled to the Al XII ground state by electron collisions; consequently the ratio is nearly constant with density. As the density increases, the collisional recombination from the Al XIII ground state becomes the dominant mechanism populating the  $1s2p$  level, uncoupling this level to some degree from the Al XII ground state. At the same time, the fractional population of the Al XIII ground state decreases more rapidly with density than the Al XII ground state (see Fig. 3). This leads to a relative in-

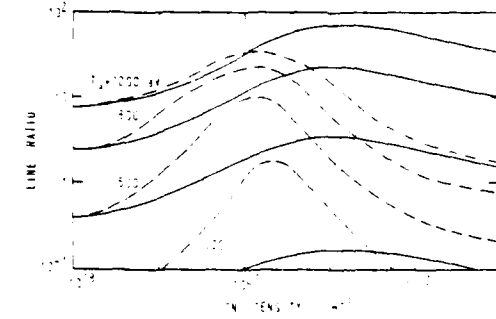


FIG. 8.  $1s-2p / 1s^2-1s3p^1P$  line ratio vs ion density; optically thin (-), optically thick with radius of 100  $\mu m$  (---).

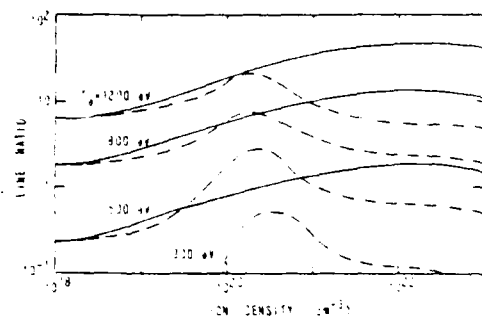


FIG. 9.  $1s-3p/1s^2 - 1s5p(^1P)$  line ratio vs ion density; optically thin (-), optically thick with radius of  $100 \mu m$  (---).

crease in the ratio of the  $1s2p^2$  to  $1s2p$  populations and a corresponding increase in the line intensity ratio. Notice that the increase occurs at a slightly lower density for the higher temperature curves. This is due to the greater fractional population of the hydrogenlike ground state at higher temperatures; this enhances the coupling of the  $1s2p^1P$  state to this ground state making its population less strongly coupled to the heliumlike ground state, yielding the density-sensitive result the ratio displays at higher ion densities.

The hydrogenlike  $L_s$  to heliumlike  $L_s$  ratio in Fig. 7, the hydrogenlike  $L_s$  to heliumlike  $L_s$  ratio in Fig. 8, and the hydrogenlike  $L_s$  to heliumlike  $L_s$  ratio in Fig. 9 all display a definite density effect at the temperatures studied. As seen from Fig. 3, the distribution of the heliumlike ground state is flat at low densities and drops off at higher densities; the hydrogenlike ground state is more peaked with a maximum near  $10^{22}$  ions/cm<sup>3</sup>. The line ratios in Figs. 7, 8, and 9 reflect these distributions rather plainly, with definite maxima occurring in the  $10^{21}-10^{23}$  ions/cm<sup>3</sup> range. It is interesting to note that while these ratios possess

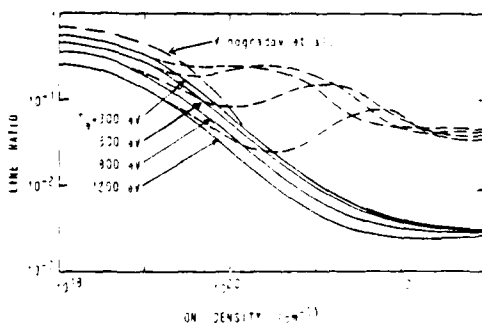


FIG. 10.  $1s^2-1s2p(^3P)/1s^2-1s2p(^1P)$  line ratio vs ion density; optically thin (-), optically thick with radius of  $100 \mu m$  (---).

this undesirable density dependence, a knowledge of the density to within an order of magnitude allows one to predict an electron temperature from the curves with an uncertainty of usually less than 100 eV. Since most experimental plasmas are able to be diagnosed easily to densities within this range, these line ratios are still valuable indications of the plasma temperature.

The intercombination-to-resonance line ratio in Fig. 10 is a well-known density diagnostic<sup>23</sup> used with reasonable success<sup>24, 30</sup> for laboratory plasma. The intercombination line is usually a very weak line compared to the heliumlike resonance line due to a relatively small radiative decay rate. As  $Z$  increases, however, this coefficient increases to within less than a few orders of magnitude of the decay rate of the resonance line, and a reasonable line ratio measurement can usually be made for  $Z > 11$ . At low densities, both the  $1s2p^1P$  and  $1s2p^3P$  levels are populated by electron collisions from the ground state and depopulated by spontaneous decay, yielding a rather constant ratio at corona densities. As the density increases, however, collisional effects coupling the four  $n=2$  levels become increasingly important. The effect is twofold: The density of the rapidly decaying singlet  $P$  level is increased from contributions from the other states, while the highly populated slowly decaying, triplet  $P$  level suffers depopulation through contributions to other  $n=2$  states. The ratio thus drops rapidly until a density is achieved at which the local-thermodynamic-equilibrium (LTE) state distributions are reached and the ratio becomes constant again. This value is given simply by

$$R = \frac{(gA)(\text{triplet})}{(gA)(\text{singlet})} \quad (10)$$

Using statistical weights and Einstein coefficients of 9 and  $2.54 \times 10^{10} \text{ sec}^{-1}$  for the  $^3P$  level, and 3 and  $2.83 \times 10^{13} \text{ sec}^{-1}$  for the  $^1P$  level gives us a value for  $R$  of  $2.69 \times 10^{-3}$ , in excellent agreement with Fig. 10 at  $10^{23}$  ions/cm<sup>3</sup>. Although the curves display some temperature dependence, an uncertainty of 300 eV in electron temperature will result in, at most, an error in the density determination of less than a factor of 2, reasonably good accuracy for this plasma parameter. Also plotted in Fig. 10 is the intercombination-to-resonance line ratio as calculated by Vinogradov *et al.*<sup>24</sup> for an aluminum plasma at an electron temperature of 360 eV. Although the ratio is only given up to an ion density of  $10^{22}$  cm<sup>-3</sup> in that study, the agreement between the two calculations is very good. The small differences between the values obtained from that work and ours are attributed to the fact that the collisional-excitation and col-

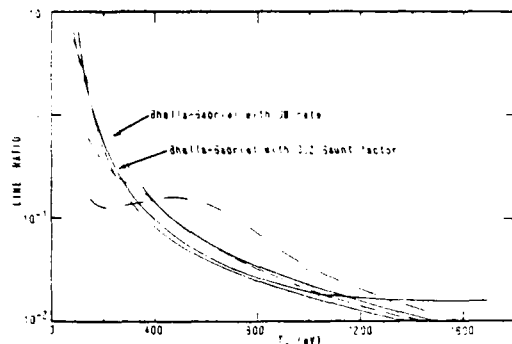


FIG. 11.  $1s^2 2p(^2P)$ - $1s^2 2p(^2D)$ / $1s^2-1s^2 2p(^1P)$  line ratio vs electron temperature; optically thin (-), optically thick for  $50\text{-}\mu\text{m}$  (---) and  $500\text{-}\mu\text{m}$  (---) plasma.

lisional-ionization-rate coefficients used in the two studies have been calculated by different methods.<sup>13</sup> In addition, the radiative decay rate used in that work for the  $1s 2p(^3P)$ - $1s^2$  transition differs slightly from the one used in our model.<sup>31</sup> However, the similarities between the predictions of the two models is encouraging.

The temperature dependence of the four temperature-sensitive ratios have been plotted in Figs. 11-14 for an optically thin plasma (solid lines) at a density of  $10^{20}$  ions/cm<sup>3</sup>. The satellite-to-resonance line ratio in Fig. 11 displays the usual  $T_e^{-1} e^{-E/T_e}$  behavior resulting from an analysis of the  $1s^2$ ,  $1s 2p(^1P)$ ,  $1s 2p(^2D)$  3-level system. Balancing the population of the doubly excited lithiumlike state by electron capture with the depopulation of this state by autoionization and spontaneous radiative decay yields the dielectronic recombination (DR) rate<sup>32</sup>

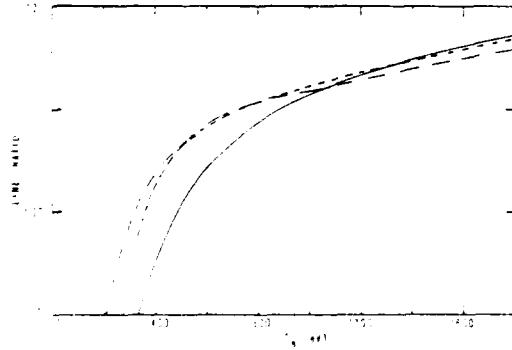


FIG. 12.  $1s-2p/1s^2-1s^2 2p(^1P)$  line ratio vs electron temperature; optically thin (-), optically thick for  $50\text{-}\mu\text{m}$  (---) and  $500\text{-}\mu\text{m}$  (---) plasma.

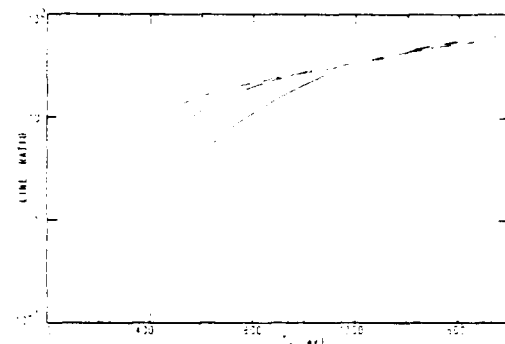


FIG. 13.  $1s-2p/1s^2-1s^3p(^1P)$  line ratio vs electron temperature; optically thin (-), optically thick for  $50\text{-}\mu\text{m}$  (---) and  $500\text{-}\mu\text{m}$  (---) plasma.

$$\alpha_{DR} = 2.06 \times 10^{-16} \frac{g_s}{g_t} A_r \\ \times \left( \frac{A_d}{A_d + A_r} \right) T_e^{-1/2} e^{-E_s/T_e}, \quad (11)$$

where  $g_s$  and  $g_t$  are statistical weights of the doubly excited and heliumlike ground states,  $A_r$  and  $A_d$  are the radiative decay and autoionization rates for the doubly excited state, and  $E_s$  is the energy separation between the  $1s^2$  and  $1s 2p(^2D)$  states. A value for the line ratio can be obtained by dividing  $\alpha_{DR}$  by the electron collisional-excitation rate from the  $1s^2$  to the  $1s 2p(^1P)$  level. An approximate expression for this rate due to Van Regemorter<sup>33</sup> is

$$X = 1.7 \times 10^{-3} f \langle \bar{g} \rangle \Delta E^{-1} T_e^{-1/2} e^{-\Delta E/T_e}, \quad (12)$$

where  $f$  is the oscillator strength,  $\langle \bar{g} \rangle$  is a thermally averaged Gaunt factor and  $\Delta E$  is energy separation of the transition. The division of the two rates yields the well-known Bhalla-Gabriel

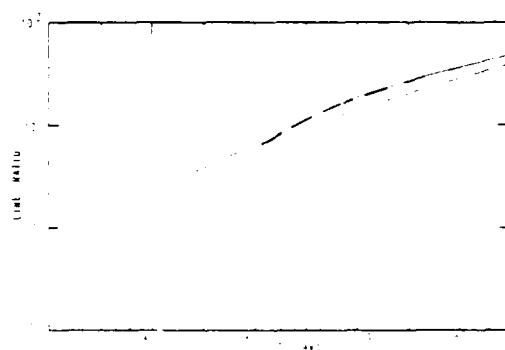


FIG. 14.  $1s-3p/1s^2-1s^3p(^1P)$  line ratio vs electron temperature; optically thin (-), optically thick for  $50\text{-}\mu\text{m}$  (---) and  $500\text{-}\mu\text{m}$  (---) plasma.

formula<sup>14</sup> for this line ratio,

$$R = 1.212 \times 10^{-13} \frac{g_s \Delta E}{g_e f(g) T_e} \times \left( \frac{A_r A_s}{A_r + A_s} \right) e^{(\Delta E - E_s) / T_e}. \quad (13)$$

This result was first derived for use in astrophysical phenomena and has been a valuable diagnostic when the two excited states are populated predominantly from the heliumlike ground state; that is, in low-density regimes. As was stated earlier, at higher densities, the  $1s2p^1P$  level begins to be affected by contributions from the  $1s2s^1S$  and  $1s$  states, and the population density diverges slightly from its coronal value. For comparison, we plotted the analytical result for this ratio alongside the CRE result in Fig. 11. One curve employs a 0.2 value<sup>14</sup> for the Gaunt factor and formula (12) for the excitation rate, while the other uses the distorted-wave result for the excitation rate instead of formula (12) in obtaining the ratio. At an electron temperature of 500 eV, our model predicts the  $2s-2p$  rate to be 50% of the dominant  $1s-2p$  rate, even at the nominal density of  $10^{20}$  ions/cm<sup>3</sup> for which Fig. 11 was obtained. The neglect of the complete collisional coupling at these plasma parameters would then result in a predicted radiation intensity from the AlXII  $L_\alpha$  line which is 30% lower than the CRE model, a significant error in the emission of the most prominent line in the x-ray region of the aluminum spectra. Hence, when employing this ratio for accurate temperature determination of laboratory plasmas at higher ( $>10^{19}$ ) densities, the analysis requires the complete  $n=2$  level system.

The apparent agreement between the curve using the 0.2 Gaunt factor with Eq. (13) and the CRE calculations at lower temperatures is the result of the missing collisional couplings and the inaccurate rate coefficient for the  $1s-2p$  transition canceling each other in the 0.2 Gaunt factor curve.

The satellite-to-resonance line ratio does present the plasma spectroscopist with some inherent difficulties, however. The sensitivity of the ratio is diminished somewhat at higher temperatures, the resonance line is quick to be affected by opacity, and some experimental difficulties occur when trying to resolve the satellite line completely. On the other hand, the major contribution to both upper levels responsible for this ratio comes from the same level, the heliumlike ground state. When the two upper levels of the ratio originate from separate ion ground states, the danger exists that these ions will appear as strong emitters in different spatial regions of the plasma, and the ratio will yield a

meaningless value for the temperature if a temperature gradient exists in the plasma. The validity of these model predictions would then be limited, applying only to experimental spectra which is spatially resolved.

The line ratios in Figs. 12-14 are similar in that they compare a hydrogenlike line intensity with a heliumlike line intensity. The basic feature of all the curves is the monotonic increase in the ratio as the AlXIII ground state becomes more populated, relative to the AlXII ground state. Of the three line ratios, the hydrogenlike  $L_\alpha$  to the heliumlike  $L_\alpha$  in Fig. 14 is probably the best one in terms of accuracy. The two transitions which make up the ratio lie at very similar energies (6.055 and 6.18 Å), their spontaneous decay rates are of the same order ( $4.77 \times 10^{12}$  and  $1.58 \times 10^{12}$  sec<sup>-1</sup>), opacity is not expected to affect either line in laboratory-size plasmas until higher densities are achieved, the ratio is of order 1 over a range of electron temperatures (400-800 eV) commonly encountered in laboratory aluminum plasmas, and the sensitivity of the ratio in that range is very good.

### C. Line ratios from optically thick plasmas

In order to account for reabsorption of emitted line radiation for optically thick plasmas, we attenuate the escaping photon flux by a phenomenological reduction in the radiative source function. This reduction factor,  $\gamma$ , discussed earlier, is calculated to account for the number of ion scatterings the photon undergoes before it diffuses in frequency to the optically thin wings of the broadened line profile, where it can escape. While this model can accommodate the radiation transfer for a natural, Doppler, or Voigt line profile, the calculations presented here were performed using Voigt line profiles.

We have plotted the line ratio behavior versus density for a plasma with a radius of  $100 \mu\text{m}$  in Figs. 6-10 (broken curves). Comparing these with the optically thin curves, it is found that the thin and thick line ratios are identical at  $N_i = 10^{12} \text{ cm}^{-3}$ , indicating that this plasma is probably transparent to x rays at these densities. Although this is, in fact, the case here, the true indication of whether photon absorption is occurring for a particular line can be found from the optical depth, given by Eq. (2).

An optical depth at line center ( $\nu = \nu_0$ ) of less than 0.1 usually indicates that self-absorption is negligible. However, larger optical depths can occur accompanied by significant photoexcitation in the plasma, yet no effect in the line intensity be apparent. When the plasma is radiation dom-

inated, the rate of stimulated absorption may be quite large due to large  $\tau$ , but if the downward radiative processes (spontaneous and stimulated) dominate over other collisional processes which destroy the upper state, absorbed photons will be reemitted again and again. This process will continue until the photons redistribute in frequency to the thin wings of the line or in space to the edge of the plasma, where they escape. Hence, an indication of whether photon absorption will affect the line intensity is given by the quenching parameter for a line whose upper state is  $i$  and lower state is  $k$ ,

$$\rho_i = \frac{\sum C_{ij}}{\sum_j C_{ij} + A_{ik}}, \quad (14)$$

where  $C_{ij}$  represents collisional rates and  $A_{ik}$  is the Einstein coefficient. When  $\rho_i$  is small, collisional quenching of the upper state is not appreciable, and the emitted line intensity will be unaffected by significant reabsorption. A quenching parameter of near one, on the other hand, indicates that any photon reabsorbed is likely to be collisionally quenched, resulting in a large reduction in the line intensity. However, when  $\tau$  is large, the upper-state population will be altered due to the large photoexcitation rate, regardless of whether  $\rho_i$  is large or small.

Comparing the general features of the curves, all of which include a heliumlike Lyman-series line as part of the line ratio, a common trend is apparent. The curves all display a shoulder structure beginning at densities above  $10^{20}$  ions/cm<sup>3</sup>. The onset of this shoulder signals the point at which the Al XII Lyman lines begin to be affected by opacity. The  $L_\alpha$  line is usually the first of the lines considered here to be attenuated by reabsorption of photons since its radiative decay rate is the largest and its lower state (which determines the optical depth) is the Al XII ground state, the level which is the most dominant fractional density over a wide range of temperatures and densities. For example, the intercombination line has an Einstein coefficient which is 3 orders of magnitude lower while the satellite line and the Al XIII  $L_\alpha$  line are due to transitions which end on different, less populated levels over a significant temperature range. The curves maximize and then turn over as the other line comprising the ratio begins to suffer opacity reduction. In Figs. 6 and 10, where both the upper levels of each ratio are populated predominantly from the  $1s^2$  level and general state abundance variations can be folded out, the shoulder appears at a higher density for the high-temperature curves. This is characteristic of the  $T^{-1/2}$  dependence of the optical depth [see

Eq. (3)]; at high temperatures, the optical depth will become large only at higher densities. Hence, the onset of opacity effects will occur at higher densities for a ratio at 1200 eV than one at 500 eV. In Figs. 7-9, where a hydrogenlike and heliumlike line are compared, the shoulder at 500 eV is larger than the one at 1200 eV, emphasizing the dominance of the Al XII ion at the lower temperature. However, the most striking feature of many of the curves, and, in terms of diagnostics, a rather unfortunate one, is the double-valued nature of the line ratios. This aspect of these curves could render them useless as plasma diagnostics unless either the plasma density is relatively well known or several of the diagnostics are used simultaneously in plasma parameter determinations.

As an analytic check on the model calculations, line-intensity ratios in the LTE (high density) limit with opacity effects included have been calculated for the  $H(L_\alpha)$  to  $He(L_\alpha)$  ratio and the IC to  $He(L_\alpha)$  ratio. To first-order approximation with a Voigt profile used in the radiation transport model, the line ratio can be expressed as

$$R = \frac{N_2 A_2 \Delta E_2}{N_1 A_1 \Delta E_1} \left( \frac{\tau_1}{\tau_2} \right)^{1/2}. \quad (15)$$

The main assumption here is that the broadening is nearly the same for the two transitions forming the ratio. The optical depth is proportional to the radiative decay rate, the  $g$  factors of upper and lower states, and the lower-state population density; hence Eq. (15) becomes

$$R = \frac{N_2 \Delta E_2}{N_1 \Delta E_1} \left( \frac{A_2 g_2 / g_2 N'_1}{A_1 g'_1 / g'_1 N'_2} \right)^{1/2}, \quad (16)$$

where the prime refers to the lower state of the transition. In the case of the ratio of the two resonance lines, the Saha equation<sup>10</sup> can be used to calculate the ratio of the  $n=2$  and  $2p^1P$  levels:

$$\frac{N(n=2)}{N(2p^1P)} = \frac{2g_{n=2}}{N_e g_{2p}} \left( \frac{m_e k T_e}{2\pi\hbar^2} \right)^{3/2} e^{-\Delta E/k T_e}. \quad (17)$$

A similar expression can be used to get the ratio of the two lower states, the Al XII and Al XIII ground states. Inserting the appropriate atomic parameters, the ratio is calculated to be about 0.26 at 500 eV, which compares quite well with the model prediction of 0.3 in Fig. 7, even though the levels considered here are not in a state of LTE with each other at a density of  $10^{23}$  ions/cm<sup>3</sup>. Density criteria for LTE will be discussed in detail in Sec. III D.

The LTE limit for the IC line-to-resonance line ratio is simpler to calculate since (1) the lower state of both transitions is the Al XII ground state and (2) the strong collisional coupling between

the  $2p$  singlet and triplet levels will equilibrate their populations to nearly a 1:3 ratio at even moderate ( $\sim 10^{23}$  ions/cm $^3$ ) densities. Hence, Eq. (16) becomes (note that the energies are nearly equal),

$$R_{\text{LTE}} \approx 3 \left( \frac{A_{\text{IC}}}{3A_{\text{RES}}} \right)^{1/2}. \quad (18)$$

Inserting the appropriate parameters in (18) yields a value of 0.05 for the LTE ratio of the IC and He( $L_s$ ) lines in the optically thick case, while the curves calculated by the model tend to center around 0.04, again, quite favorable agreement.

It is often believed that the opacity effects on the line emission intensities in laboratory plasmas might be small enough to use diagnostics developed for optically thin plasmas if the size of the emitting region of the laboratory plasma was small or the densities were not extremely high. To illustrate the opacity effects on laboratory plasmas, we have plotted the temperature dependence on the line ratios in the optically thick case in Figs. 11-14 for a plasma of  $10^{20}$  ions/cm $^3$  and radii of 50 and 500  $\mu\text{m}$ , typical of a laser-produced plasma and an exploding wire plasma. In all ratios but the H( $L_s$ ) to He( $L_s$ ), the transport of the radiation has a significant effect on the values that would be determined for the electron temperature. In fact, the error incurred by using optically thin calculations for these plasmas can be as much as 200-300 eV for the 500  $\mu\text{m}$  plasma and 100-200 eV for the 50- $\mu\text{m}$  plasma. Curiously enough, the ratios may also be useful in determining the size of the emitting region.

Looking more closely at the optically thick calculations plotted in Figs. 12-14, the results for the larger-radius plasma yield values for the line ratios which are larger at low temperatures and smaller at high temperatures than those predicted by the optically thin calculation. This is a reflection of the shift in abundances from the AlXII ion to the AlXIII ion as electron temperature increases. At 500 eV, the  $1s^2$  level is more populated than the  $1s$  level; consequently, the optical depths of the heliumlike Lyman lines are greater than those of the hydrogenlike Lyman lines, and the greater attenuation of line radiation from AlXII excited states is manifested in the enhancement of the line ratios. At 1600 eV, the opposite is true of the relative abundances of the  $1s^2$  and  $1s$  levels; therefore, the line ratios will be decreased somewhat compared to those calculated in the optically thin approximation.

#### D. Comparison with LTE model

Since the ionization-radiation model described

here is characterized both by particle collisions and photon processes in an equilibrium mode, it was termed a collisional-radiative model. Another model frequently used to calculate the plasma atomic state is the LTE model.<sup>10</sup> The models differ in that the LTE assumption presupposes that a radiative process is negligible when compared to a competing collisional process. The CRE model, however, takes both processes into account, explicitly. An abundance curve, calculated using an LTE model, is shown in Fig. 3 (broken curves) for a plasma at 300 eV, alongside the CRE results. As would be expected, the higher ionization stages approach the LTE limiting values at higher densities; lithiumlike states attain their LTE values at an ion density of  $2 \times 10^{22}$  cm $^{-3}$ , while this occurs for the heliumlike, hydrogenlike, and stripped ions at densities of  $10^{23}$ ,  $3 \times 10^{23}$ , and  $6 \times 10^{23}$  ions/cm $^3$ , respectively.

Because of its simplicity, the LTE ionization model has had widespread applications in the plasma community for the purpose of diagnostics and effective charge determinations in laboratory plasmas. To test the validity of the application of the LTE model, simple expressions<sup>11</sup> have been offered to determine whether plasma conditions are within the constraints of the LTE regime. The basis of these expressions is the notion that a collisional rate depopulating a level must be a factor of 10 greater than a competing radiative rate from this level for the state population to be within 10% of its LTE value. We will attempt to show, here, that this can be too strict a density requirement.

If we consider the rates which couple the AlXIV ion to the AlXIII ground state, the competing processes are collisional (3-body) recombination and radiative (2-body) recombination. The collisional recombination rate coefficient is given by,<sup>9</sup> in cm $^6/\text{sec}$ ,

$$\beta = 8.05 \times 10^{-28} (g_u/2g_l) \xi \chi^{-2} T_e^{-1} \quad (19)$$

while an approximate expression can be used for the radiative rate coefficient,<sup>12</sup> in cm $^3/\text{sec}$ ,

$$\alpha \approx 5.2 \times 10^{-14} Z \lambda (0.43 + \frac{1}{2} \ln \lambda + 0.469 \lambda^{-1/3}), \quad (20)$$

while  $g$  is the statistical weight,  $\xi$  is the number of outer-shell electrons,  $\chi$  is the ionization energy,  $Z$  is ion charge,  $\lambda = \chi/T_e$ , and  $u$  and  $l$  refer to upper and lower states. The ratio  $\beta N_e / \alpha$  becomes equal to 10 at an electron density of about  $1.7 \times 10^{26}$  cm $^{-3}$  yielding an ion density of about  $6 \times 10^{23}$  cm $^{-3}$ . Hence, these two ground states should attain the population density ratio close to that predicted by the Saha equation for a plasma at 300 eV above an ion density of  $6 \times 10^{23}$  ions/cm $^3$ . A similar calculation for the hydrogenlike and

heliumlike ground states yields an ion density of about  $9 \times 10^{25} \text{ cm}^{-3}$  at 300 eV.

A similar estimate can be applied to excited states, where the collisional-deexcitation rate coefficient must exceed the largest competing radiative decay rate by about a factor of 10 for the upper and lower states to be in LTE with each other. If we consider the  $1s-2p$  transition in AlXIII and employ the collisional-excitation rate coefficient from our distorted-wave calculation, the ion density required for these levels to be in LTE with respect to each other is around  $1 \times 10^{24} \text{ cm}^{-3}$ . A similar calculation with the  $1s^2-1s2p\ ^1P$  transition indicates that an ion density of at least  $1.5 \times 10^{24} \text{ cm}^{-3}$  is required for these two levels to equilibrate to their LTE values.

The values obtained from these simple expressions are noticeable higher than those predicted by the CRE model as seen in Fig. 3. It would appear that the use of the above expressions neglects the rather important effect of the interplay between the levels which lie in energy between the ground states. Since the density at which states equilibrate to their LTE values generally increases with energy separation, many close-lying levels will reach their LTE population ratios at much lower densities than the cases considered above which are typified by large energy differences. In an apparent "bootstrapping" process, the coupling between these levels and the ground states is enough to cause significant equilibration of the ground states toward LTE at densities significantly lower than those predicted by a simple test involving an isolated 2-level system. Hence, a collisional-radiative treatment with some excited-state structure included is necessary to accurately ascertain at what density and temperature a plasma can adequately be described by an LTE model.

Although the restrictions on the density required for LTE are seen to be eased somewhat by the results of this study with the CRE model, care must be taken when making theoretical predictions based on diagnostics from an LTE calculation. At densities where  $K$ -shell excited states have equilibrated to their LTE population ratios but the ground states have not, the absolute populations of the excited states (and consequently the radiation emission) will be incorrect, since they are determined relative to the still non-LTE ground-state densities.

It is well known that photoexcitation in an opaque plasma will force it toward a state of LTE at lower densities than would be predicted in the optically thin approximation. To illustrate, opacity effects were included in the calculation for a  $100-\mu\text{m}$ , 300-eV plasma, and the fractional distributions plotted in Fig. 3 (dotted-dashed lines) also. Notice

that the optically thick CRE results are always between the optically thin CRE and the LTE predictions, and that there is a substantial change in the populations in a direction closer to those for LTE over a density range of  $10^{20}-10^{22} \text{ ions/cm}^3$ . Notice also, however, that the plasma becomes collision dominated above  $5 \times 10^{22} \text{ ions/cm}^3$  and the CRE calculation with opacity effects included does not differ significantly from the CRE thin prediction of the density at which the plasma finally attains the LTE state.

#### IV. DISCUSSION

This work has investigated some of the fundamental aspects of line emission from a hot dense aluminum plasma. In particular, we have examined the radiation signature by modeling the plasma ion dynamics using a collisional-radiative model which includes opacity effects. Line ratios were calculated and then compared, in two cases, with older theoretical predictions, and contrasted with the result predicted when opacity effects are taken into account. We have shown that what may appear to be a well-behaved and understood diagnostic in an optically thin approximation may, in fact, be a rather complex double-valued function dependent on both plasma temperature and density when the optical depth of a photon through the plasma becomes large. An important result of this work which we would like to stress is not that these line ratios may become ineffective diagnostic tools when they are taken from a spectra emitted from an optically dense plasma. Rather, it now becomes apparent that a comprehensive treatment of the radiation diagnostics is required. Close agreement between a number of separate temperature or density diagnostics can resolve the dilemma of double valuedness. The comparison of parameters determined from line ratios and those obtained from other methods such as series merging,<sup>36</sup> Stark profiles,<sup>37</sup> or slope of the continuum can also be an effective technique. However, the entire spectrum must be analyzed in detail to properly make use of the plasma diagnostic techniques available.

The results of this model have also been compared with the LTE result and it has been seen that the plasma cannot be fully described by an LTE model until rather large densities have been obtained. Although, in an opaque plasma, excited states may approximate their LTE populations at a significantly lower density than in an optically thin plasma, due to optical pumping through re-absorption of photons, the ground states will still maintain populations between the LTE and coronal limits at this lower density, only slightly affected

by the opacities considered here. Thus, though the excited-state populations may be correctly determined relative to the next-higher ground-state density, line ratios calculated from lines which originate in excited states from different ionization stages will be in error since the ground states are not accurately given by their LTE-determined values. It is also worth noting that there is a disagreement between abundance curves quoted here and those shown in Ref. 9, which depicts highly overpopulated Al<sup>XIII</sup> and Al<sup>XIV</sup> ions. This result appears unphysical in light of the previous discussion of electron shell configurations and their effect on the ionization dynamics. The lithium-like ion with an ionization potential of 442 eV should ionize easily to the closed-shell Al<sup>XII</sup> ion and should never constitute a major partial density fraction over a wide range of temperatures at an ion density of only  $10^{22} \text{ cm}^{-3}$  as is shown in Ref. 9. This is in agreement with work done previously by other authors<sup>38,39</sup> on aluminum as well as other materials of nearly the same atomic number. In addition, the study in Ref. 9 includes a graph showing that their CRE model is in agreement with the LTE result for the Al<sup>XIV</sup> population at an ion density of about  $5 \times 10^{22} \text{ cm}^{-3}$ , a factor of 10 lower than in Fig. 3. It is our opinion that this disagreement is due to their collisional-ionization rate from Al<sup>XIII</sup>. An approximate form for the rate is given in Ref. 6, in  $\text{cm}^3/\text{sec}$ ,

$$S \propto \zeta X^{-2} T_e^{1/2} e^{-\chi/kT_e}, \quad (21)$$

where  $\zeta$  is the electron number in the outermost shell. This would predict a rate for Al<sup>XII</sup> which is about twice as large as that for Al<sup>XIII</sup> (ionization potentials are within 10% of each other). This is in disagreement with Fig. 5 of Ref. 9 which shows the Al<sup>XIII</sup> rate to be about two orders of magnitude greater than the Al<sup>XII</sup> rate at  $T_e = 300$  eV. The Al<sup>XII</sup> collisional-ionization rate used in this study is in good agreement with the one quoted in Ref. 9, hence it is the questionably large Al<sup>XIII</sup> ionization rate which is the cause of their

#### Al<sup>XIV</sup> population.

Some discussion of the approximations made in constructing this model is warranted in order to properly assess the significance of the analysis presented here. The equations governing the physics described above are solved numerically by a zero-dimension (single-zone) computer model; this allows only for treatment of plasmas which are homogeneous in temperature and density at the time of the radiation pulse. In addition, the rate equations are solved time-independently; hence, the assumption is made that the width of the radiation pulse is small compared to the hydrodynamic time scale of the plasma. The atomic level structure used was selected in order to describe the most important  $K$ -series emission lines, based on analysis of experimental spectra and the states contributing most significantly to its formation, either quantitatively or qualitatively (within the temperature range of interest of this work). Thus, we have retained some structure which is less important energetically, for diagnostic purposes. We have not included detailed structure in most of the  $L$ -shell ions, leaving that for later investigations. Finally, several atomic processes have been omitted such as multiphoton excitation, photoionization, and inner-shell collisions. The model retains the flexibility to include these processes in future work, but their contribution toward the determination of the level populations is considered of less importance in plasmas studied in this paper.

#### ACKNOWLEDGMENTS

The authors would like to thank Dr. J. Rogerson for his aluminum LTE calculations, Dr. V. Jacobs for calculating the dielectronic recombination rates, and Dr. P. C. Kepple and Dr. K. G. Whitney for helpful discussions and suggestions. One of us (D.D.) was supported by an NRC-NRL Resident Research Associateship. This work was supported in part by the Defense Nuclear Agency.

\*Present address: Science Applications, Inc., McLean, Virginia.

<sup>1</sup>K. B. Mitchell, D. B. Van Hulsteyn, G. H. McCall, Ping Lee, and H. R. Griem, Phys. Rev. Lett. 42, 228 (1979).

<sup>2</sup>B. Yaacobi, D. Steel, E. Thorsos, A. Hauer, and B. Perry, Phys. Rev. Lett. 39, 1526 (1977).

<sup>3</sup>J. Mizui, N. Yamaguchi, T. Yamanaka, and C. Yamanaka, Phys. Rev. Lett. 39, 619 (1977).

<sup>4</sup>J. P. Apruzese, J. Davis, and K. G. Whitney, J. Appl. Phys. 47, 4433 (1976); 48, 667 (1977).

<sup>5</sup>A. L. Hoffmann and E. A. Crawford, J. Appl. Phys. 49,

3219 (1978).

<sup>6</sup>R. K. Landshoff and J. D. Perez, Phys. Rev. A 13, 1619 (1976).

<sup>7</sup>D. Duston and J. J. Duderstadt, J. Appl. Phys. 49, 4388 (1978); Phys. Rev. A 18, 1707 (1978).

<sup>8</sup>J. Davis and K. G. Whitney, J. Appl. Phys. 45, 5294 (1974).

<sup>9</sup>D. Salzmann and A. Krumbein, J. Appl. Phys. 49, 3229 (1978).

<sup>10</sup>J. Richter, in *Plasma Diagnostics*, edited by W. Lochte-Holtgreven (North-Holland, Amsterdam, 1968).

<sup>11</sup>R. W. P. McWhirter, in *Plasma Diagnostic Techniques*,

- ques*, edited by R. H. Huddlestone and S. L. Leonard (Academic, New York, 1965).
- <sup>12</sup>D. G. Colombant, K. G. Whitney, D. A. Tidman, N. K. Winsor, and J. Davis, *Phys. Fluids* 18, 1687 (1975).
- <sup>13</sup>D. Duston and J. Davis, NRL Memorandum Report No. 3846, 1978 (unpublished).
- <sup>14</sup>M. J. Seaton, *Proc. Phys. Soc. London* 79, 1105 (1962).
- <sup>15</sup>V. L. Jacobs, J. Davis, P. C. Kepple, and M. Blaha, *Astrophys. J.* 211, 605 (1977).
- <sup>16</sup>W. J. Karzas and R. Latter, *Astrophys. J. Suppl. Ser.* 6, 167 (1961).
- <sup>17</sup>V. L. Jacobs and J. Davis, *Phys. Rev. A* 19, 697 (1978).
- <sup>18</sup>W. Wiese, M. Smith, and B. Miles, *Atomic Transition Probabilities* (U.S. GPO, Washington, D.C., 1969), Vol. II.
- <sup>19</sup>L. A. Vainshtein, and I. I. Sobel'man, *Lebedev Report No. 66* (1967); I. I. Sobel'man, *Introduction to the Theory of Atomic Spectra* (Pergamon, Oxford, 1972).
- <sup>20</sup>J. Davis, P. C. Kepple, and M. Blaha, *J. Quant. Spectrosc. Radiat. Transfer* 16, 1043 (1976).
- <sup>21</sup>George B. Field, *Astrophys. J.* 129, 551 (1959).
- <sup>22</sup>D. G. Hummer, *Astrophys. J.* 140, 276 (1964).
- <sup>23</sup>P. S. Julienne and J. Davis, NRL Memorandum Report No. 2556, 1973 (unpublished).
- <sup>24</sup>A. G. Hearn, *Proc. Phys. Soc. London* 81, 648 (1963).
- <sup>25</sup>P. G. Burkhalter, C. M. Dozier, and D. J. Nagel, *Phys. Rev. A* 15, 700 (1977).
- <sup>26</sup>L. F. Chase, W. G. Jordan, J. D. Perez, J. G. Pronko, *Appl. Phys. Lett.* 30, 137 (1977).
- <sup>27</sup>P. Burkhalter, J. Davis, J. Rauch, W. Clark, G. Dahlbacka, and R. Schneider, *J. Appl. Phys.* 50, 705 (1979).
- <sup>28</sup>A. V. Vinogradov, I. Yu. Skobelev, and E. A. Yukov, *Kvant. Elektron. (Moscow)* 2, 1165 (1975) [Sov. J. Quantum Electron. 5, 630 (1975)].
- <sup>29</sup>H. J. Kunge, A. H. Gabriel, and H. R. Griem, *Phys. Rev.* 165, 276 (1968).
- <sup>30</sup>E. V. Aglitskii, V. A. Boiko, A. V. Vinogradov, and E. A. Yukov, *Kvant. Elektron. (Moscow)* 1, 579 (1974) [Sov. J. Quantum Electron. 4, 322 (1974)].
- <sup>31</sup>C. D. Lin, W. R. Johnson, and A. Dalgarno, *Phys. Rev. A* 15, 154 (1977).
- <sup>32</sup>A. H. Gabriel and C. Jordan, in *Case Studies in Atomic Collision Physics*, edited by E. W. McDaniel and M. H. McDowell (North-Holland, Amsterdam, 1972), Vol. 2.
- <sup>33</sup>H. Van Regemorter, *Astrophys. J.* 136, 906 (1962).
- <sup>34</sup>C. P. Bhalla, A. H. Gabriel, and L. P. Presnyakov, *Mon. Not. R. Astron. Soc.* 172, 359 (1975).
- <sup>35</sup>M. J. Seaton, *Mon. Not. R. Astron. Soc.* 119, 81 (1959).
- <sup>36</sup>J. Davis, NRL Memorandum Report No. 2655, 1973 (unpublished).
- <sup>37</sup>H. R. Griem, M. Blaha, and P. C. Kepple, *Phys. Rev. A* 19, 2421 (1979).
- <sup>38</sup>C. Jordan, *Mon. Not. R. Astron. Soc.* 142, 501 (1969).
- <sup>39</sup>L. L. House, *Astrophys. J. Suppl. Ser.* 9, 307 (1964).

APPENDIX C

SOFT X-RAY AND KUV RADIATION FROM HIGH  
DENSITY ALUMINUM PLASMAS

D. Duster\* and J. Davis

Plasma Radiation Group  
Naval Research Laboratory  
Washington, D. C. 20375

July 1980

\*Science Applications Inc., McLean, Va.

ABSTRACT

Radiation emission over a wide range (5-5000 Å) of wavelengths in a high density aluminum plasma has been studied theoretically. The atomic model includes explicit treatment of a large number of states and transitions characterizing the line emission from the Al III - Al XIII ions. The state populations are calculated using a set of atomic rate equations describing a plasma in collisional-radiative equilibrium. The ionization state of the plasma is calculated self-consistently with line and continuum radiation transport using a 1-dimensional multi-cell structure for the plasma. A new radiation transport scheme has been implemented in this model based on probability of escape for both line and continuum photons. The total L and K-shell radiation emission is described as a function of plasma temperature, density, and source size, and is compared to predictions made from corona and local thermodynamic equilibrium models. It is shown that over a wide range of plasma parameters, neither of these two limiting models accurately describes the plasma emission characteristics. Several line intensity ratios from L-shell lines are studied and shown to be useful diagnostic indicators of the plasma temperature and density. Finally, theoretical spectra are calculated and discussed in the context of their comparability with experimental spectra in order to make contact with real plasma radiation signatures and exploit the predictive capabilities of the model.

## I. Introduction

The x-ray emission from high density aluminum plasmas has received much attention in recent years due to interest in results from exploding wire experiments<sup>(1,2)</sup>, laser plasmas<sup>(3,4)</sup>, and particle beam-foil interactions<sup>(5)</sup>. Theoretical analysis of the radiation emission from these dense plasmas is useful for understanding both the plasma energetics and determination of plasma parameters from spectral diagnostics. Several models have been developed in an effort to understand various aspects of aluminum plasma emissions, concentrating on K-shell ions<sup>(6-10)</sup>, some L-shell<sup>(11)</sup> and M-shell<sup>(12)</sup> ions. In this study we include excited states from all ions of the K and L shells of aluminum as well as Al III in the M shell. In addition, the ionization dynamics and radiation transport calculations are solved self-consistently for all included level populations producing line and continuum photons in a one-dimensional plasma model. The multicell aspect of this model also allows us to treat stationary plasmas in which there exists temperature and density gradients characteristic of imploding wire array plasmas.

This work will be presented in four sections. First, a detailed description of the level structure and rate coefficients employed in this model is presented along with a brief description of the ionization-radiation calculation as well as the radiation transport. Second, the gross characteristics of both the line and continuum radiation are studied as they vary with the plasma electron temperature, ion density and plasma radius. The results are then compared with those obtained from local thermodynamic equilibrium (LTE) and corona models and define the plasma conditions necessary for the valid application of these models. Third, we explore the details of the bound-bound radiation spectrum to describe various line intensity ratios from the L shell ions which can effectively be applied to diagnose plasma parameters in temperature regimes lower than that in which K-shell ions are abundant. Finally, in the fourth section we present theoretically generated emission spectrum and discuss, in detail, their implications with respect to plasma diagnostics. Although these calculations have been done for an aluminum plasma, the interplay between particle collisions and photon transport in determining level populations and radiation emission are expected to be typical of many dense plasmas. Therefore, we have attempted to be as general as possible

in our analysis of the results, realizing that many of the trends occurring in this study will be typical of L-shell emission from other materials. Some features of the data will nevertheless be strongly dependent on the detailed rates and structure representative of aluminum in particular, and we have made an effort to point out these occurrences when not obvious.

## II. ATOMIC MODEL

### A. Level Structure

Integral to any theoretical prediction of the radiation emission from a plasma which spans a significant temperature range in its evolution is the detailed system of states included in the atomic model. In a previous work on K-shell emission<sup>(6)</sup>, we chose to include several higher lying states whose emission was diagnostically useful but were not energetically significant. In this study, it was necessary to include many states for energetic purposes alone. Because of the smaller energy differences between ground and excited levels in L shell ions as compared to those of the K-shell, excited level populations constitute a non-negligible fraction of the total population at ion densities typical of exploding wire plasmas and one would like to include many levels in each ion to insure completeness of the radiative description. On the other hand, several criteria restrict the number of levels one can practically include in a model: (i) the availability of data for higher Rydberg members of L-shell aluminum ions, (ii) the unwieldiness of solving, self-consistently with radiation transport, a set of rate equations for several hundred levels, (iii) time restrictions on computer runs to solve this large set of equations for a meaningfully extensive set of parameters. With these restrictions in mind, the number of levels to include per ion was decided upon after scanning several sources of XUV spectral data<sup>(13)</sup> and identifying the strongest lines. These spectra showed that  $\Delta n = 0$  transitions of the form  $2s^2 2p^n - 2s2p^{n+1}$  and  $2s2p^{n+1} - 2p^{n+2}$  were very evident in many of the shots, despite the high density of the plasmas. In addition, very few lines were identified above principle quantum number 3 for all but the alkali ions, Al XI and Al III. We chose, therefore, to include, in addition to the ground states, the  $n = 2$  and  $n = 3$  levels in all ions in as complete a manner as possible, as well as a few higher  $n$  states in the two alkali ions. The complete level structure employed in this

study is shown Table I along with the state energy (measured from ground). The energies of the states were taken from the level diagrams of Bashkin and Sconer<sup>(14)</sup> and the tables of Martin and Salubas<sup>(15)</sup>; wavelengths of bound-bound transitions were taken from reference 14 and the tables of Kelly and Palumbo<sup>(16)</sup>.

In a previous study on the K-shell emission<sup>(17)</sup>, it was found that at high densities, many of the individual  $l$  states of a given  $n$  level may be in Boltzmann equilibrium with each other due to heavy particle collisions. Specifically, if the energy separation between level  $nl$  and  $nl'$  is small compared to the plasma thermal energy, ion-ion collisions will cause the levels to equilibrate at densities lower than electron-ion collisions would. Since the primary purpose of this investigation is to study high density plasma radiation (typically, ion densities greater than  $10^{18} \text{ cm}^{-3}$ ), the assumption has been made that many of the close-lying states have equilibrated and the ratio of their populations is given by the ratio of their statistical weights. The individual  $nl$  levels are then grouped as a single "degenerate"  $n$  level with the appropriate statistical weight. In addition, any rate populating this  $n$  level is an average (over initial states) of each rate populating the individual  $nl$  states. This method of treating levels of similar electron configuration and separated by only a few electron volts in energy allows the model to carry a large number of excited levels while reducing computation time that would have been used calculating a known relationship between many of the levels. The brackets in Table I indicate the levels which were appropriately combined in our model.

### B. Rate Coefficients

With the exception of electron collisional excitation rate coefficients and spontaneous decay rates, the methods of calculating the various rate coefficients used in this study have been described in detail in previous papers<sup>(6,18)</sup>, and only brief reference will be made to these. Every state is coupled to the next (energetically) highest ground state by collisional ionization, photo-ionization, collisional recombination and radiative recombination. The collisional ionization rates are calculated by Seaton's prescription<sup>(19)</sup>, and

the photoionization rates are calculated in the hydrogenic approximation<sup>(20)</sup> using effective free-bound Gaunt factors<sup>(21)</sup>. Collisional and radiative recombination rates are then calculated as the detailed balance of these. In addition, adjacent ground states are coupled by dielectronic recombination<sup>(22)</sup> found by summing capture rates over a manifold of states above the ionization limit which then decay via cascade to the ground state.

Excited levels of a given ion are coupled to other selected excited levels and the ground state by electron collisional excitation and de-excitation, stimulated emission and absorption, and spontaneous radiative decay. In the K-shell ions, Al XII and Al XIII, and in Al XI, the collisional couplings are complete, including forbidden and spin-flip transitions as well as those which are dipole allowed. For Al XIII, the Coulomb-Born approximation<sup>(23)</sup> was used, while a distorted wave calculation with exchange<sup>(24)</sup> was used to calculate the coefficients for Al XI and Al XII. Comparisons of these two methods have been made for several transitions in Al XIII<sup>(17)</sup>, and excellent agreement was obtained.

The prohibitively large number of levels to be collisionally coupled in the remaining ions precluded the indiscriminate use of the distorted wave calculation for these transitions. Instead, a calculation employing the semi-classical impact parameter method<sup>(25)</sup> with thermally averaged Gaunt factors<sup>(26)</sup> was used to couple levels between which electric dipole transitions are allowed, while forbidden transitions were neglected. When dipole oscillator strengths, required by the impact parameter code, were not available, a Bates-Damgaard calculation<sup>(27)</sup> was used to generate them.

Many of the ions contain excited levels from several spin systems and it was necessary to collisionally couple these systems (usually between the lowest lying excited state in the system and the ground state); the distorted wave calculation was used for these transitions to take account of the spin flip. If these couplings are not included, the state populations in the spin systems not coupled to the lower ground state are found to float somewhat at low electron densities, being coupled only to the ground state above by ionization and radiative recombination. While collisional ionization is the dominant de-populating mechanism for these states at coronal collisional excitation from the ground state dominates over recombination as the main populating process; hence, if these rates are not included, incorrect populations for these states are generated by the model.

AD-A094 186

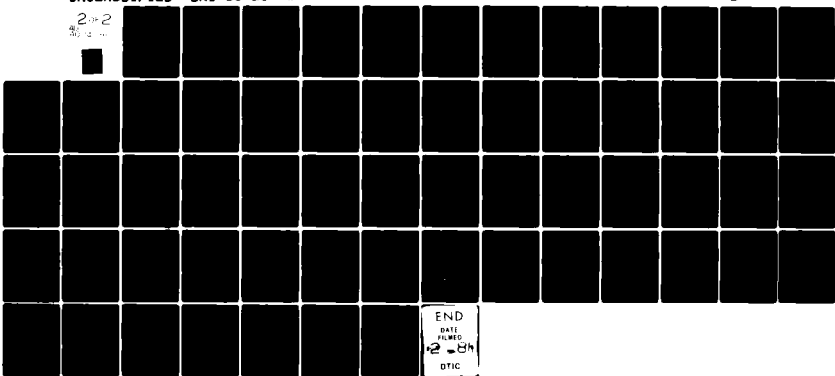
SCIENCE APPLICATIONS INC MCLEAN VA  
RADIATION FROM HIGH TEMPERATURE PLASMAS.(U)  
SEP 80 J APRUZESE, E KANE, P VITELLO  
UNCLASSIFIED SAI-81-239-W/A

F/G 20/9

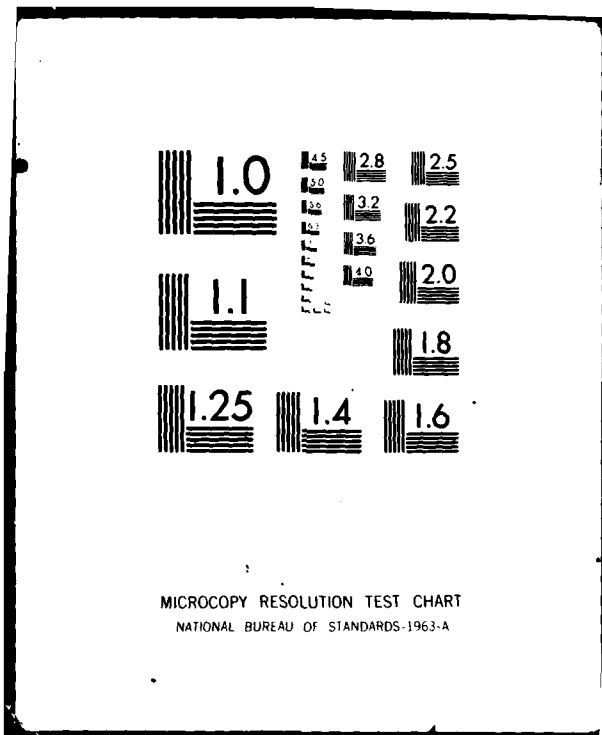
N00173-79-C-0448

NL

202  
SAI-81-239-W/A



END  
DATA INFO  
2 - 84  
DTIC



MICROCOPY RESOLUTION TEST CHART  
NATIONAL BUREAU OF STANDARDS-1963-A

Dipole oscillator strengths and spontaneous radiative decay rates for the L-shell ions were extracted from several sources. The very complete tabulation by Lindgard and Nielsen<sup>(28)</sup> was the source of these rates for lithium-like Al XI and sodiumlike Al III. Many of the oscillator strengths describing the transitions  $2s^2 2p^n - 2s2p^{n+1}$  and  $2s2p^{n+1} - 2p^{n+2}$  for beryllium-like Al X through oxygenlike Al VI were found in the calculations by Fawcett<sup>(29)</sup>. The following references were also consulted as sources for oscillator strengths: Martin and Simons<sup>(30)</sup> for Al X, Shamey<sup>(31)</sup> and Weiss<sup>(32)</sup> for Al IX, McIntyre et al.<sup>(33)</sup> for Al VIII, Buchet and Buchet-Poulizac<sup>(34)</sup> for Al V - VII, Kernahan et al.<sup>(35)</sup> for Al III - VII, Mewe<sup>(36)</sup> for Al V, Shorer<sup>(37)</sup> and Loginov and Gruzdev<sup>(38)</sup> for Al IV. Finally, the tables of transition probabilities by Wiese et al.<sup>(39)</sup> were used for many of the L-shell f-values not located in the above sources. As stated earlier, all oscillator strengths not contained in the references were generated from a Bates-Damgaard calculation.

A brief discussion at this point about the effect of neglecting forbidden transitions in the L-shell ions is warranted. At low density, this is a good approximation if the radiation emission is the quantity one is most concerned with. At these densities, the plasma is in the coronal regime and excited states are populated predominantly by electron collision from the ground state. Consequently, only low-lying  $n = 2$  levels will have significant populations and the bulk of the line radiation will be due to transitions from these states. Since almost all of the transitions involving a 2s-2p excitation are dipole-allowed, the  $n = 2$  populations and hence the radiation will be calculated accurately. Since many of the  $n \geq 3$  levels are forbidden in their coupling to the ground state, their populations may not be as accurate, but the radiation from these states is negligible at low densities. At high densities, collisional ionization and recombination between excited states and the next highest ground state dominate the redistribution of the populations among the excited states; since these rates are included in the model, all population densities are accurately determined in the LTE regime. The collisional-radiative regime between corona and LTE is where collisional excitation processes are most important in determining the populations of states with  $n \geq 3$ . Although forbidden transitions will definitely affect the populations of and radiation from these levels, we place the maximum error in populations due to the neglect of these

rates at a maximum of a factor of 2 and an uncertainty of at most 50% in the total radiation emission (based on our previous work with collisional couplings in the aluminum K-shell). The inclusion of forbidden transitions and their effect on the L-shell line emission will be the subject of a future study.

### C. Ionization Dynamics and Radiation Transport

The scheme for solving the ionization dynamics of an equilibrium plasma has been described in detail in earlier work<sup>(6)</sup>. Briefly, an atomic rate equation of the form

$$\frac{dN_i}{dt} = \sum_j w_{ji} N_j - \sum_j w_{ij} N_i \quad (1)$$

can be written for each ground and excited state included in the model, where  $w_{ji}$  is a rate for populating state  $i$  and  $w_{ij}$  is a rate for depopulating state  $i$ . In this study, the approximation is made that the plasma radiation pulse is short compared to characteristic hydrodynamic time scales, and hence, state populations are constant during the duration of the pulse. This allows for a steady-state solution and the time derivative can be set to zero in equation (1). In addition, no hydrodynamic equations are as yet solved together with the rate equations; thus, the solution to the set of equations (1) represents a plasma frozen in space and time at, for example, the point of peak plasma emission.

The radiation transport employed here represents an improvement on our phenomenological frequency diffusion technique reported on earlier<sup>(6,17)</sup>, and is based on a calculation of the probability of escape of photons born in the plasma. The probability that photons born in a given zone of the plasma and re-absorbed in a different zone (or allowed to escape to the detector) is calculated, taking into account both stimulated emission and stimulated absorption processes. These probabilities are calculated assuming that the line emission profile is a Voigt and, therefore, both Doppler and collisional broadening contribute to the line width.

The probability of escape for a Voigt line profile is defined by Hummer<sup>40</sup> and is given by,

$$P_e \approx 2/3 \left[ \frac{a_{ij}}{\tau_0} \right]^{1/2} \quad (2)$$

where  $\tau_0$  is the line-center optical depth and  $a_{ij}$  is the Voigt damping parameter defined by,

$$a_{ij} = \frac{\sum_k A_{ik} + \sum_k X_{ik} + \sum_k A_{ik} + \sum_k X_{ik}}{4 \pi \Delta v_D} \quad (3)$$

Here, A and X represent all radiative and collisional rates depopulating the upper level, i, and the lower level, j, of the transition, while  $\Delta v_D$  is the Doppler width of the line,

$$\Delta v_D = \left[ \frac{2T_i}{Mc^2} \right]^{1/2} v_0 \quad (4)$$

where  $T_i$  is ion temperature, M is ion mass, and  $v_0$  is the photon frequency at line center. Using the expression in equation (2), the probability that a photon emitted in cell m will traverse, unabsorbed, to a cell boundary can be calculated. Thus, using the difference of such probabilities, one can determine the probability that a photon emitted in zone m will be absorbed in zone  $m'$ . By calculating zone-to-zone coupling coefficients,  $C(m,m')$ , in this way for each emission line, one computes the probability of escape from zone m by,

$$P_z(m) = 1 - C(m,m) \quad (5)$$

where  $C(m,m)$  is the coupling coefficient relating the photon absorption probability before reaching the first zone boundary. The photon pumping rate in zone m due to photons emitted in other zones and absorbed in zone m is then given by,

$$R_{\text{pump}} = \frac{\sum_{m' \neq m} N(m')^* A C(m', m) \Delta V(m')}{\Delta V(m)} \quad (6)$$

where  $N^*$  is the density of the upper state of the transition,  $A$  is the radiative decay rate,  $\Delta V$  is the zonal volume, and the coupling coefficients,  $C(m, m')$ , contain terms accounting for both stimulated absorption (photo-excitation) and stimulated emission. The quantities calculated in eqns. (5) and (6) are employed in the atomic rate equations since the reabsorption of photons can significantly alter the ionization state and excited state distributions in the plasma<sup>6</sup>. Finally, we define the probability of escape of a line photon from zone  $m$  to the spectrometer,

$$P_{\text{esc}}(m) = 1 - \sum_{m'} C(m, m') \quad (7)$$

and the line intensity that exists the plasma,

$$I_{v_0} = \sum_m N^*(m) A P_{\text{esc}}(m) h v_0 \Delta V(m) . \quad (8)$$

In a time-dependent calculation,  $I_{v_0}$  would be integrated in time to describe the temporal evolution of the spectral line as the state densities and opacity of the plasma change. A more detailed discussion of the method of calculating the coupling coefficients and the probability of escape transport technique can be found in the work of Apruzese et al<sup>41</sup>. In addition to transporting line photons, we have developed a method for transporting bound-free continuum photons as well. Using the photoionization cross sections calculated by a method described earlier, a probability of escape for photons originating from radiative recombinations is calculated based on the recombination edge profile and implemented in the rate equations in a way similar to that for the line photons. A detailed description of this method will be described in a following work.

### III. RADIATION POWER IN PLASMAS

The main emphasis of this study is to quantify both the gross and detailed features of the radiation emission from the L-shell ions of dense aluminum plasmas. Previously, it was necessary to characterize the gross nature of the emission by either a corona model in the low density limit, or an LTE model in the high density limit. In this section, we present collisional-radiative equilibrium (CRE) results from a study of the line and continuum radiation as they vary with plasma temperature, density and size. In addition, comparisons are made between predictions of this CRE calculation and the other two limiting models to establish regions of validity for their application.

In order to assess the collisional properties of the plasma and allow for a more equitable comparison between models, a study of the total line emission as a function of temperature and ion density was conducted with the initial assumption that the plasma was optically thin. The results are shown in Fig. 1, where the total bound-bound emission power coefficient (Power density divided by electron density divided by ion density) is plotted as a function of electron temperature for various ion densities from  $10^{11} - 10^{23} \text{ cm}^{-3}$ . Plotting the power coefficient allows one to easily discern the departure from corona equilibrium, since that model predicts a coefficient which is independent of density. The radiation from L-shell ions is seen in Fig. 1 to peak about 60-120 eV while the K-shell emission maximizes at 1 keV. The curves for  $10^{11}$  and  $10^{13} \text{ cm}^{-3}$  are identical, indicating that the plasma can truly be described by a corona model at those densities. Deviations from coronal equilibrium become noticeable above  $10^{15} \text{ cm}^{-3}$  for L-shell radiation and above  $10^{19} \text{ cm}^{-3}$  for K-shell radiation. At low densities, the maximum radiative emission at the L-shell exceeds that of the K-shell by an order of magnitude, while at high densities, the K-shell radiation is much stronger. This is due to the increase in electron collisional quenching of L-shell photons as the density is increased and the L-shell ion states tend toward LTE. In fact, at very high density, the L-shell peak disappears completely, leaving a functional dependence suggestive of the power radiated by a black-body, viz

$$P = \sigma T^4 \quad (9)$$

where  $\sigma$  is the Stefan-Boltzmann constant and  $T$  is plasma temperature. The deviation from corona equilibrium for the K-shell first appears at about  $10^{19}$

$\text{ions/cm}^3$ ; this occurs at a much higher density for the K-shell because typical energy separations between ground and excited states in the K-shell are much larger, and hence, collisional de-excitation rates are much smaller than those for L-shell ions. (The corona approximation is no longer valid when collisional de-excitation becomes comparable to radiative decay in depopulating excited states).

The curves shown in Fig. 1 are, of course, due to the manifold of L and K-shell ions emitting line radiation which is peaked at temperatures corresponding to roughly the peak in their ground state abundances. The individual ionic contributions to the total line emission are shown in Fig. 2, where radiated power density vs.  $T_e$  (electron temperature) for an optically thin plasma at  $10^{19} \text{ ions/cm}^3$  is plotted. Notice that the boronlike Al IX peak falls somewhat below the Al VIII peak disrupting what was a monotonic increase in peak intensities with increasing ionic charge. This could be due to: some inherent atomic structure differences, such as a reduction in intensity as a closed subshell is attained; a possible error in an oscillator strength; or some level structure being left out of the model. Since the peak would need an increase of about 50% to bring it in line with the ionic trend, it is possible that the radiation from some  $n = 3$  states not included in the model could account for the difference. According to model predictions, the strongest radiating lines at 70 eV (Al IX peak temperature) in Al IX are  $2s^2 2p(^2P) - 2s^2 3s$ ,  $- 3p$ ,  $- 3d$  (doublet),  $2s2p(^4P) - 2s2p3d(^4P, ^4D)$ , and  $2s^2 2p(^2P) - 2s2p^2(^2S, ^2P, ^2D)$ , in that order. The  $2s2p3s$ ,  $- 3p$ , (quartet) states were not included, but it's possible that they could have accounted for a significant portion of the Al IX emission due to their transitions to the  $2s2p(^4P)$  level.

It was stated earlier that in the coronal regime the bulk of the plasma line radiation emanating from the L-shell ions is due to  $\Delta n = 0$  transitions within the  $n = 2$  states. To illustrate how that changes as density increases, the individual line power densities from Al VIII (carbonlike) are shown vs.  $T_e$  for an optically thin plasma at  $10^{19} \text{ cm}^{-3}$  in Fig. 3. The transitions in Al VIII shown in this figure are listed in Table II along with their approximate wavelengths. Note that while  $n = 2$  transitions still dominate, a large portion of the radiation now comes from decays from  $n = 3$  levels. The peak intensities for these transitions occur at slightly higher temperatures than the  $n = 2$

transitions due to their larger excitation energies. The extent to which the higher Rydberg states contribute to the total ionic line emission at high plasma densities can seriously affect the validity of the atomic model. If not enough level structure is included in the model, the theoretical calculation may seriously underestimate the gross radiation features. As an example, one would probably assume that  $n = 4$  and  $n = 5$  levels would be important at densities above  $\sim 10^{20} \text{ cm}^{-3}$  based on Fig. 3; hence, the two curves in Fig. 1 for ion densities of  $10^{21}$  and  $10^{23} \text{ cm}^{-3}$  could be in error due to the omission of these and even higher levels. This would, in fact, be the case if it were not for lowering of the ionization potential in dense plasmas. Using the method prescribed by Griem<sup>(42)</sup>, the ionization lowering was determined for carbonlike Al VIII in a 50 eV plasma. At an ion density of  $10^{19} \text{ cm}^{-3}$ , the lowering is only about 5.0 eV; however, at  $10^{21} \text{ cm}^{-3}$ , it is nearly 45.0 eV and the reduced ionization limit falls approximately 10 eV above several of the  $n = 4$  excited states in this ion, pushing higher energy states into the continuum. While these estimates are only approximate, it is doubtful that gross errors are present in the radiation calculations. Moreover, it is found that lithiumlike Al XI is the strongest L-shell radiator above  $10^{19} \text{ cm}^{-3}$ , peaking at about 100 eV, and excited levels up to  $n = 6$  have been included for this ion to assure approximately correct calculation of the peak intensity at high densities (at  $10^{21} \text{ ions/cm}^3$  and 100 eV, the calculated ionization potential of Al XI lies just above the  $n = 5$  level).

As plasma density increases, the level populations and, thus, the radiation emission approach values that would be predicted by an LTE model. This trend is illustrated in Fig. 4, where we have used an LTE calculation with the identical level structure as in our CRE model to predict the optically thin line emission; a comparison is made with the CRE results for three ion densities. At  $10^{21} \text{ ions/cm}^3$  the L-shell line emission is very nearly in LTE while the K-shell is not. At  $10^{23} \text{ ions/cm}^3$ , the L-shell is in LTE and the K-shell shows only small differences from LTE. An approximate hydrogenic formula<sup>(42)</sup> can be used to determine the density at which excited states go into LTE;

$$N_e \geq 9 \times 10^{17} \left( \frac{\Delta E}{E_H} \right)^3 \left( \frac{T_e}{E_H} \right)^{1/2} \text{ cm}^{-3} \quad (10)$$

where  $\Delta E$  is the transition energy and  $E_H$  is the ionization potential of hydrogen. Using the  $n = 3$  state of Al XI at 120 eV yields an electron density of  $1.3 \times 10^{22} \text{ cm}^{-3}$  or an ion density of  $\sim 2 \times 10^{21} \text{ cm}^{-3}$ , which gives very reasonable agreement with the result in Fig. 4, at 120 eV.

In the interest of comparison with corona and LTE models, CRE results have been presented for optically thin plasmas only. Photon reabsorption, however, will play a more important role for L-shell line emission than for the K-shell in dense laboratory plasmas. In order to study the effect of photo-excitation and stimulated emission on the radiation, the plasma size was varied for a number of calculations, since the photoexcitation rates are dependent on the optical depth which is, in turn, dependent on the plasma physical extent. Shown in Fig. 5 is the bound-bound power density vs.  $T_e$  for a plasma at  $10^{19} \text{ ions/cm}^3$  and a radius which varies from  $50 \mu\text{m}$  to  $5000 \mu\text{m}$  (the thin curve is also plotted). Note that at these parameters, the K-shell is only slightly affected by opacity while the L-shell emission is reduced at peak  $T_e$  (120 eV) by factors of  $1/3$ ,  $1/6$ , and  $1/9$  of the thin result as the radius increases by an order of magnitude. Since the optical depth is also proportional to the population density of the lower state of the transition, it is expected that these opacity effects will be magnified at higher densities, while at lower densities, the emission will tend toward the optically thin values.

In addition to line photons, the radiation from free-bound transitions (due to radiative recombination) is also transported. The effects of opacity on the continuum are illustrated in Fig. 6 where the continuum power density is shown vs.  $T_e$  for the same plasma parameters as in Fig. 5. Note that in the region of L-shell emission the effect is reversed! Since reabsorption and transport of line photons results in strong optical pumping of the excited state populations, the increase in ground state populations via collisional ionization results in a subsequent increase in radiative recombination photons which more than compensates for the attenuation of continuum photons by photo-ionization processes (photoionization is almost negligible at these plasma parameters). Hence, the continuum radiation power density, being strongly tied to the excited state densities, increases as the radius of the plasma increases. This anomalous behavior is, however, strongly density dependent,

and photon attenuation by photoionization processes will overtake the pumping effects described above as the plasma density rises. Also notice, upon comparison, that while K-shell line emission dominates over continuum emission by about a factor of 5, the continuum radiation from L-shell ions is comparable to or exceeds the line photons for laboratory-size plasmas at this density.

Having examined both bound and continuum contributions to the emission individually, we are now in a position to understand the total radiation emission characteristics, shown in Fig. 7, for identical plasma parameters as in Figs. 5 and 6. The most striking feature is the relatively small difference between total radiated power density for the 50, 500, and 5000  $\mu\text{m}$  plasmas over all ranges of temperature at  $10^{19}$  ions/cm<sup>3</sup>. Only the optically thin approximation differs significantly, and only by a factor of 6 at the L-shell peak at 130 eV. A consideration of the behavior of line and continuum radiation from the previous two figures shows quite clearly the compensating effect of their contributions.

An approximation that is often used to characterize the emission from dense plasmas is the black-body emission rate, given by eqn. (9). Converting the flux to a power density, the black-body (BB) radiation emission is also plotted in Fig. 7 for the three relevant plasma radii. While the slope of the BB curves is similar to the CRE curves, large quantitative errors result from using this approximation to describe a plasma at  $10^{19}$  ions/cm<sup>3</sup> except at temperatures lower than 15 eV for the 5000  $\mu\text{m}$  plasma. It is conceivable, however, that one could use the BB approximation to describe the plasma emission by employing a BB temperature lower than the actual plasma electron temperature. For example, a black-body radiation function would approximately describe the emission of a 5000  $\mu\text{m}$  plasma at  $10^{19}$  cm<sup>-3</sup> if the BB temperature used was about half of the actual temperature; factors of about 1/3 and 1/6 could be also used for the 500 and 50  $\mu\text{m}$  plasmas, respectively. The approximation, of course, is only good up to the temperature where the L-shell radiation peaks, since, at  $10^{19}$  cm<sup>-3</sup>, the K-shell is substantially removed from the LTE state which eqn. (9) characterizes. The approximation is still quite crude at  $10^{19}$  ions/cm<sup>3</sup> because the slope of the BB is steeper than the CRE curve. To illustrate the trend toward black-body emission as density increases, a curve has been drawn in

Fig. 4 (dotted line) which represents the  $T^4$  slope of the BB curve adjacent to the optically thin CRE calculation at  $10^{23} \text{ cm}^{-3}$ . Considering that the comparison is between a detailed model of the microprocesses in a plasma and a simple formula describing an ideal radiator, the agreement is significant.

#### IV. XUV DIAGNOSTICS

The motivation for modeling detailed atomic physics and radiation processes in high density plasmas is twofold: (1) In medium-to-high Z plasmas, not only is radiation a significant mechanism for the loss and re-distribution of plasma energy, but a large proportion of this energy can be contained in ion internal energy. Consequently, the atomic model can seriously affect the partitioning of energy in hydrodynamic calculations. (2) In addition to accurate determination of this partitioning, a detailed atomic model has the added attractiveness of being capable of accurate prediction of the details of emission which can then be used to diagnose conditions in laboratory plasmas. Merging of lines and continuum<sup>(43)</sup>, as well as line broadening<sup>(44)</sup> and shift<sup>(45-47)</sup>, can be helpful in determining plasma densities. Absolute line intensities can be used to predict the approximate size of the emitting region of the plasma. Line intensity ratios<sup>(42)</sup> are often accurate indicators of both temperature and density. Line ratios have been used extensively in diagnosing the temperature and density of plasmas which emit strongly in the K-shell, and many studies<sup>(6, 8, 48-50)</sup> have been done to quantify soft x-ray line ratios for this use. Few investigations have dealt, however, with the spectral diagnostics of dense, medium and high Z plasmas which lie in the XUV region<sup>(52-54)</sup>. In this section, we investigate several possible line intensity ratios from L-shell aluminum ions that show promise as density and temperature indicators for plasmas typical of exploding wire and laser-created plasma experiments.

##### A. Temperature Determinations

Appropriate line intensity ratios for temperature diagnosis in hot plasmas are relatively abundant in most XUV spectra. Since the ionic populations displays the pronounced "picket fence" effect with temperature (as does the ionic radiation, as seen in Fig. 2), intensities of lines from adjacent ions form ratios which are very sensitive to changes in plasma temperature.

This would seem to suggest that any number of pairs of lines from adjacent ions are effective diagnostics; in fact, there are further restrictive considerations. In choosing what we consider to be good diagnostics, three additional criteria need to be considered: (1) A good temperature diagnostic-line ratio should be comprised of two lines which lie close together in the spectrum. This eliminates many of the experimental uncertainties associated with non-linear response of crystal or film due to differences in wavelength. (2) The two lines should also be of sufficient intensity to be easily measured and their peak intensities should be comparable, hence, yielding a ratio near 1 in the temperature range of the plasma where the lines are strong emitters. (3) Good temperature diagnostic ratios should be somewhat independent of density variation (over a limited range of interest) and should also exhibit little change due to opacity effects. Of the three conditions, the last is the most difficult to satisfy.

In Table III, selected transition pairs comprising temperature sensitive line intensity ratios for every adjacent pair of L-shell ions are listed which satisfy the first two criteria. Since individual j-components of the transitions are not treated in this model, the contributions over a number of wavelengths need to be summed in several cases in order to experimentally obtain the total intensity of the transition as calculated by the model; these wavelengths are also given. The line ratios for these transitions vs. electron temperature for an optically thin plasma at  $10^{19}$  ions/cm<sup>3</sup> have been calculated and are shown in Fig. 8. Note that these ratios provide useful diagnosis over a wide range of temperatures corresponding to the range over which L-shell radiation is prominent. In an earlier work<sup>(6)</sup> on aluminum K-shell diagnostics, it was shown that line intensity ratios formed from lines from heliumlike and hydrogenlike ions provide insight into plasmas temperatures over an effective range beginning at about 300 eV. In light of this result and from examination of Fig. 8, there exists a large temperature range from about 150 eV to about 300 eV in which no temperature diagnostic is available. This is, of course, the range which lies between the lithiumlike and heliumlike systems - the barrier between the two atomic shells. A line ratio was calculated for this pair of ions, but Al XII lines don't effectively turn on until temperatures of about 250-300 eV are reached, resulting in this difficult region for diagnosis. However this, in itself, is informative in interpreting spectra. Namely, any time-resolved

spectrum in which both lithiumlike and heliumlike lines occur together (specifically 25-50 Å, in aluminum) and show comparable intensities is an indication of a rather substantial temperature gradient in the plasma source. This is not necessarily true for lines from adjacent ions within the L-shell...

The third criteria referred to earlier involves the variation of the temperature-sensitive ratios with density and opacity. If the line ratio varies significantly with either of these plasma parameters, the problem of interpreting the experimental spectrum becomes a very complicated puzzle in which the assessment of size, temperature, and density are all strongly coupled. In order to illustrate these effects on the line ratios listed in Table III, the  $2p-3s/2s^2-2s3p(^1P)$  ratio (#7) was selected as an example. This ratio was calculated from 50 to 200 eV for plasmas of  $10^{17}$ ,  $10^{19}$ , and  $10^{21}$  ions/cm<sup>3</sup> in the optically thin approximation and at  $10^{19}$  ions/cm<sup>3</sup> with opacity effects for plasma of radii 50, 500, and 5000 μm; the results are displayed in Fig. 9. The results show primarily, that the line intensity ratio depends only slightly on the plasma density between  $10^{17}$  and  $10^{21}$  ions/cm<sup>3</sup>. The ratio tends to diverge more as the temperature increases, so that at 170 eV, near the upper temperature limit for applicability of this diagnostic (the Al X line is too faint above this temperature), the ratio at  $10^{17}$  cm<sup>-3</sup> is about 1.6 times the ratio at  $10^{21}$  cm<sup>-3</sup>. If one were to use the low density curve as a universal one, and attempt to diagnose a high density plasma, errors in the predicted temperature of 25-30 eV could be expected. In reality, the density is usually known to within an order of magnitude, and, using the results of this model, one could anticipate only small discrepancies in a temperature determination using this ratio. Nevertheless, the density effects on the ratio are so small within the range of Fig. 9, that practically speaking, the ratio is density insensitive. The reason for this insensitivity is not immediately apparent. Close inspection of the dominant depopulating rates of the upper levels of each transition shows that over the 4 orders of magnitude change in density in Fig. 9, the levels traverse from the coronal region to the collision-dominated plasma regime. The radiative decay coefficients for the  $2p-3s$  and  $2s^2-2s3p$  transitions are  $1.5 \times 10^{11}$  sec<sup>-1</sup> and  $4.6 \times 10^{11}$  sec<sup>-1</sup>, respectively. At  $10^{17}$  ions/cm<sup>3</sup> and 100 eV, the respective electron collisional de-excitation rates are  $5.3 \times 10^8$  and  $2.8 \times 10^8$  cm<sup>3</sup>/sec, well below the radiative decay rates, implying a coronal behavior for the upper level populations. Thus, the line intensities are given approximately by

$$I = N_u A \Delta E = N_l \times N_e \Delta E \quad (11)$$

where  $u$  and  $l$  denote upper and lower states of the transition. Hence, at constant temperature, each line intensity scales as the total ion density squared, and the line ratio remains constant at coronal densities. At  $10^{21}$  ions/cm<sup>3</sup>, however, the collisional de-excitation rates are  $5.3 \times 10^{12}$  and  $2.8 \times 10^{12}$  cm<sup>3</sup>/sec, exceeding the radiative decay rates by factors of 35 and 6, respectively. At this density, the L shell ion populations are approaching their LTE distribution. In LTE, we can relate the 2s3p <sup>1</sup>P state population ( $N_1$ ) to the 2s <sup>2</sup>S ground state population ( $N_0$ ) by the Saha equation,

$$\frac{N_e N_0}{N_1} = \frac{g_0}{g_1} \frac{2(2\pi m T)^{3/2}}{h^3} \exp(-\Delta E_{10}/T) \quad (12)$$

We can also express the relationship between the 2s and 3d ( $N_2$ ) levels of Al XI via Boltzmann's Law,

$$\frac{N_2}{N_0} = \frac{g_2}{g_0} \exp(-\Delta E_{02}/T) \quad (13)$$

Eliminating  $N_0$  and  $g_0$ , we find,

$$\frac{N_2}{N_1} = \frac{g_2}{N_e g_1} \frac{2(2\pi m T)^{3/2}}{h^3} \exp(-\Delta E_{12}/T) \quad (14)$$

Thus, in strict LTE, the ratio of the populations and, hence, the line intensities (in the optically thin approximation) scale by a factor of  $N_e^{-1}$ . To illustrate, we have plotted, as isolated points, the line ratio at densities of  $10^{22}$  and  $10^{23}$  ions/cm<sup>3</sup> and a temperature of 100 eV in Fig. 9. It becomes apparent that this line ratio loses its "density insensitive" quality somewhere between  $10^{21}$  and  $10^{22}$  ions/cm<sup>3</sup> as the levels make the transition from the collisional-radiative regime to that of LTE. In fact, this is the criteria which determines the density sensitivity of the other line intensity ratios in Table III; as two adjacent ions approach a state of LTE, the line ratio formed by emission lines from each of them becomes very dependent on the plasma density and unsuitable as a temperature diagnostic unless the density is known to good accuracy.

The effect of photoexcitation on the line ratio is also shown in Fig. 9. As the temperature increases, it is generally the transition from the lower-charge ion which first becomes attenuated by the plasma opacity, causing an initial increase in the value of the line ratio compared to the optically thin value. As the temperature continues to increase, the ionic populations change and the transition from the higher-charge ion becomes optically thick, reducing the ratio somewhat as compared to the thin value; both of these effects are seen in Fig. 9. Notice that the larger 5000  $\mu$ m plasma exhibits a ratio closer to the thin values than the 500  $\mu$ m plasma from about 50 to 150 eV. This is a function of the relative values of oscillator strengths and collisional quenching rates of the respective transitions. This behavior, therefore, is particular to these transitions at this density, and is not characteristic of any general trend in radiation transport effects. The absence of radiation transport can lead to errors in the calculation, as seen in Fig. 9, but these errors would lead to temperatures which are typically 10 to 20 eV higher than the correct calculation yields. At lower densities, the tendency toward an optically thin plasma reduces these effects somewhat. The way to reduce opacity effects in line intensity ratios is (1) to choose transitions which have small oscillator strengths, or (2) which end on levels which are not as highly populated as the ground state. Unfortunately, this results, in the first case, in choosing transitions which may be too weak to detect. The second case is not useful since the L-shell excited state populations are not significantly smaller than the ground states in the density regime of interest for this investigation. Hence, if a truly accurate determination is required, a detailed calculation with radiation transport is necessary.

### B. Density Determinations

The criteria discussed in the previous section concerning good temperature diagnostic line ratios apply to good density diagnostic line ratios by simply interchanging the words "temperature" and "density". Density diagnostics, however, were much more difficult to locate in the spectrum since the variation of line intensities with density is not as straightforward as it is with temperature. In addition, several of the diagnostic ratios first selected, although density-sensitive, displayed only small changes in the value of the line ratio with density variations; thus, experimental error would introduce large

uncertainties in density determinations. We found we were most successful by choosing lines which originated from different spin systems within the same ion. Because of the forbidden nature of the transitions of different spin-system levels to the ground state, density effects were often profound in determining the population of the excited states. Lines from the same ion were chosen to ensure that the radiation from both lines was emitted from the same location in the plasma. A problem which occurs in these diagnostics for L-shell ions is the narrow range of temperatures over which the ions exist (see Fig. 2). As the plasma temperature deviates slightly from the small interval over which the transitions radiate strongly, the line ratios become extremely temperature dependent. Three pairs of lines were selected as density diagnostics over a limited range of temperatures, however, and they are listed in Table IV along with the relevant wavelengths. The line intensity ratios for these transitions are plotted vs. ion density in Figs. 10-12 for an optically thin plasma for several electron temperatures at which the lines are strong radiators. In Fig. 10, the two transitions are from nitrogenlike Al VII; from Fig. 2, the line emission from this ion peaks at about 35 eV and the line ratio at 30 and 40 eV in Fig. 10 are reasonably close above  $3 \times 10^{18}$  ions/cm<sup>3</sup>. The ratio at 50 eV displays larger deviations from the other curves above this density, since the Al VII emission is already 15 eV removed from the peak emitting temperature. Note also the double-valuedness of the ratio complicates spectral interpretation even further. This ratio is typical of the transition pairs we investigated from Al IV - Al VII ions; significant temperature dependence over even small ranges of T<sub>e</sub>. In Figs. 11 and 12, the line ratios show much less temperature sensitivity and no double-valuedness in the useful density region. In Fig. 12, the ratio changes very little over a temperature range of 80 eV, causing, for example, an error of at most a factor of 5 in the density determination if the experimental line ratio was 2.0. It is assumed, however, that the temperature could be determined to better accuracy than that from diagnostics presented earlier, and the density could probably be determined to less than a factor of 2 error by a comprehensive analysis of the spectrum. Agreement between many aspects of the theoretical and experimental spectrum is in fact the only way to insure that the plasma has been accurately characterized by the model. In the following section, this point is explored in relation to the generation of theoretical spectra with CRE calculations.

## V. CALCULATION OF THEORETICAL SPECTRA

In the previous sections, we presented the results of L-shell aluminum calculations which we deemed useful in gaining understanding of the radiation energetics in dense plasmas over a wide range of temperatures, as well as providing diagnostic information applicable to the determination of plasma parameters. Although one can often make a strong case for an attempt to characterize a plasma via an isolated diagnostic, we are of the opinion that ionization-radiation dynamic calculations have, at present, reached a level of sophistication that allows for direct comparisons of theoretically generated spectra and those obtained experimentally. Moreover, it is our contention that only by this comprehensive replication of line and continuum radiation signatures, that anything definitive can be said about the ability of the theoretical calculations to characterize the experimental plasma. In this section, theoretical spectra calculated by our radiation model for a plasma with a temperature gradient similar to that found in imploding wire array plasmas are presented and discussed. These spectra are not intended to be an attempt to model any individual wire implosion but are meant to be illustrative of the ability of the theoretical model to produce spectra suitable for comparison with experiment using only plasma temperature, density, and size of emitting region as input parameters. For examples of actual experimental spectra from imploding wire plasmas and other dense plasma sources, the reader is referred to an upcoming paper by D. Nagel.<sup>13</sup>

Within the probability of escape phenomenology employed by this model, a radiation spectrum can be calculated by summing the frequency-by-frequency contributions from each plasma zone for line emission, recombination radiation, and bremsstrahlung. Only the bremsstrahlung is not transported through the plasma since the free-free opacity is small for the density and temperature regime of interest here. The contribution from each zone is determined from the radiative source function and the probability of escape to the vacuum region beyond the outer boundary of the plasma. This zone-by-zone treatment produces a spectrum in which lines are superpositions of a number of different profiles and the continuum is a superposition of a number of different slopes, depending on the zonally determined temperature and density as well as the transport dependent atomic state population densities. The results are displayed as spectral intensity (in watts/cm<sup>2</sup>/angstrom) radiated into  $4\pi$  radians and plotted versus wavelength.

The temperature gradient for this example was chosen so as to approximately describe an imploded cylindrical aluminum plasma which was assembled on axis and is at the point of maximum emission in its time evolution. The plasma is taken to be 1 mm in diameter with a linear temperature gradient from 80 eV in the central region to 30 eV near the periphery. A hot K-line emitting core is usually present in these plasmas but was neglected here since it is our purpose to illustrate the emission solely from the L-shell lines in this study; however, the K-lines are easily included in the calculation by altering the temperature profile to reflect K-shell emission temperatures. A comparison of theoretical and experimental spectra from aluminum K-shell ions is the subject of another study<sup>55</sup>. Although a density gradient most likely exists in actual imploded plasmas, none was included in this example in order to eliminate confusion over which effects are due to a temperature gradient and which to a density profile. Moreover, a temperature profile alone is sufficient to illustrate the varied line emission from the L-shell ions as would be recorded by a spectrometer for an actual experiment.

The calculated theoretical spectra for the above conditions are reproduced in Figs. 13-15. Approximately 30 mÅ of source and instrumental broadening has been convoluted with the line profiles to duplicate similar conditions as would be present in experimental spectra, since this broadening mechanism often dominates line profiles for plasmas of these temperatures and densities. In Figs. 13 & 14, the spectral intensity has been plotted on a linear y-axis as would an experimental spectrum; the wavelength range has been separated into the 30-65 Å and 65-105 Å regions in order to show better detail. The 30 Å cutoff just includes the Al XI 2s-6p line, the shortest wavelength line in our L-shell model (excluding the satellite line from the doubly-excited 1s2p<sup>2</sup> <sup>2</sup>D state). If K-shell emission intensity had been comparable to the L-shell lines, however, several Balmer series lines from the hydrogenlike and heliumlike ions could be seen among the L-shell lines ranging from about 25 to 52 Å. Notice that we have allowed several very prominent lines to "saturate" our theoretical "spectrometer crystal" in order to display some of the lower intensity lines of the spectra. The jagged base line is due to recombination edges forming the free-bound continuum (the bremsstrahlung is very much lower); in actual experimental spectra, the noise level often washes out much of the finer detail of this feature, while

the absorption edges of filters frequently distort the true shape of this emission profile. Identification of the individual lines is accomplished by numbering in order of increasing wavelength, with Table V serving as a key; also given in Table V is the transition wavelength and the optical depth at line center, calculated from the central axis of the plasma to the outer boundary. The wavelengths quoted in this table are, in some cases, averages over a number of transitions with similar initial and final electron configurations but different angular momentum states; hence, they may not correspond exactly to values quoted by standard references for a given transition.

From Fig. 13, it is seen that the strongest emitters in this plasma are the lithiumlike 2p-3d transition (#10), the berylliumlike 2s2p-2s3d, -3s (singlet) transitions (#16), and the boronlike 2p-3d, -3s (doublet) transitions (#17). For the latter two lines, the intensity is due almost entirely to the transitions from the 3d levels, since both the population of these states and radiative decay rates from them exceed those of the corresponding 3s levels. An interesting feature that became apparent when comparisons were made with experimental spectra was the relative heights of the Al XI 2s-5p (#2) and 2p-6d, -6s (#3) lines. In all spectra examined, the shorter wavelength line always exceeded the longer one in intensity. Yet, when optically thin calculations were analyzed, the longer wavelength line dominated at all temperatures and over a wide range of densities. It was only when opacity effects were included in the analysis that the emission lines reversed their relative intensities and agreed with experimental data. The phenomenon is explained by the larger optical depth of the 2p-6d line; since both the 2s-5p and 2p-6d oscillator strengths are comparable (about a 2:3 ratio), the difference in opacity lies with the population density of the lower state of the transition. At these densities, the 2s and 2p levels are populated approximately according to their statistical weights at temperatures where Al XI lines emit strongly. Consequently, the 2p-6d optical depth will be about 2 to 3 times larger than that of the 2s-5p transition and the former line will be attenuated more as the plasma becomes increasingly optically dense. Initially, it was thought that this feature could be useful as an opacity diagnostic to estimate the size of

the emitting region; however, the relative changes in intensities of the two lines with plasma size was found to be too small to derive sufficiently accurate quantitative information to be able to make a definitive statement about this plasma parameter.

In Fig. 14, lines from the lower ionization stages are prevalent, with Al VI - Al VIII dominating the emission. The lines from Al III - Al V do not appear with sufficient intensity to be seen since these ions are dominant at temperatures lower than the 30 eV cutoff in our profile used in this example. In fact, this lower limit on the temperature gradient was chosen after several examples of data from aluminum wire experiments were scanned and few intense contributions to the line spectrum from these ions found.

In order to illustrate the gross characteristics of the radiation spectrum from this sample run, Fig. 15 was plotted with a logarithmic y-axis, exhibiting low intensity lines as well as the stronger ones. At the longer wavelengths, above about 240 Å, lines due to  $\Delta n=0$  transitions among the  $n=2$  levels of the L-shell ions are prominent along with a few weak lines from higher Rydberg state transitions in Al XI. The real value of a comprehensive spectrum as shown in Fig. 15 is in its ability to indicate, at a glance, which wavelength regions are responsible for the bulk of the emission. In particular, the wavelength dependence of the free-bound continuum radiation, which was seen from Fig. 6 to constitute a significant fraction of the total emission, is very clearly illustrated. This extensive picture of the radiation emission as a function of wavelength is extremely useful when knowledge of the emission from particular "energy bins" is required. In particular, single-temperature analytic models of the plasma dynamics often characterize the plasma radiation in a very approximate way, such as assuming that all the line emission is radiated at a single frequency and an appropriate optical depth, in attempt to mock up, in a concise manner, the actual emission energetics while taking some opacity effect into account. Based on runs made with a flat temperature profile, we find that comprehensive spectral plots display even more localized emission than is shown in Fig. 15 for the exemplary temperature profile. Thus, these plots serve to quantify the overall plasma emission in a way that may easily be implemented in a simple analytic calculation.

Although qualitative comparisons have been made using the spectra generated by this model and a few random experimental spectra, no attempt has, as yet, been made to quantitatively compare the theory with a specific experiment in order to diagnose the plasma conditions at the time of emission. Recently, however, spectroscopists at many laboratories have realized the wealth of information contained in the XUV region of the emission spectrum from dense plasmas, and have begun to make serious attempts to obtain good spectral data in that wavelength range as well as in the soft X-ray region dominated by the K-shell lines. It is our hope that through direct comparison of theoretical and experimental data, this model may make adequate use of that information and shed light on the continuing problem of the characterization of dense plasma dynamics and the determination of basic plasma parameters.

#### ACKNOWLEDGEMENTS

The authors would like to thank M. Blaha, P. C. Kepple, and V. L. Jacobs for many helpful suggestions regarding the detailed atomic physics, and M. Davis, J. Cain, and R. Ernst for their assistance in organizing the enormous data base used in these calculations. This work was supported by the Defense Nuclear Agency.

## REFERENCES

1. P. G. Burkhalter, C. M. Dozier, and D. J. Nagel, Phys. Rev. A 15, 700 (1977).
2. P. Burkhalter, J. Davis, J. Rauch, W. Clark, G. Dahlbacka, and R. Schneider, J. Appl. Phys. 50, 705 (1979).
3. I. Yu. Skobalev, A. V. Vinogradov, and E. A. Yukov, Physica Scripta 18, 78 (1978).
4. L. E. Chase, W. C. Jordan, J. D. Perez, and J. G. Pronko, Appl. Phys. Lett. 30, 137 (1977).
5. Electron Beam Fusion Progress Report, April-December 1978, SAND 79-1011 (1979).
6. D. Duston and J. Davis, Phys. Rev. A 21, 1664 (1980).
7. D. Duston and J. J. Duderstadt, Phys. Rev. A 18, 1707 (1978).
8. Jon C. Weisheit, C. Bruce Tartar, James H. Scofield, and Leland M. Richards, J. Quant. Spectros. Radiat. Transfer, 16, 659 (1976).
9. R. K. Landshoff and J. D. Perez, Phys. Rev. A 13, 1619 (1976).
10. A. L. Hoffman and E. A. Crawford, J. Appl. Phys. 49, 3219 (1978); D. Salzmann and A. Krumbein, J. Appl. Phys. 49, 3229 (1978).
11. J. D. Perez and Gerald L. Payne, Phys. Rev. A 21, 969 (1980); G. A. Doschek and U. Feldman, NRL Memorandum Report No. 8416 .
12. F. M. Bacon and H. A. Watts, J. Appl. Phys. 46, 4758 (1975).
13. D. J. Nagel (unpublished).
14. S. Bashkin and J. O. Stoner, Jr., Atomic Energy Levels and Grotrian Diagrams (North-Holland, Amsterdam, 1975), Vol. 1.
15. W. C. Martin and Romuald Zalubas, J. Phys. Chem. Ref. Data 8, 817 (1979).
16. R. L. Kelly and L. J. Palumbo, Atomic and Ionic Emission Lines Below 2000 Angstroms, NRL Report 7599 (1973).
17. D. Duston, J. Davis, and K. G. Whitney, NRL Memorandum Report NO 3846, 1978 (unpublished).
18. K. G. Whitney and J. Davis, J. Appl. Phys. 45, 5294 (1974), and J. Davis and K. G. Whitney, J. Appl. Phys. 47, 1426 (1976).
19. M. J. Seaton, Proc. Phys. Soc. London 79, 1105 (1962).
20. V. L. Jacobs, J. Davis, P. C. Kepple, and M. Blaha, Astrophys. J. 211, 605 (1977).

References (continued)

21. W. J. Karzas and B. Latter, *Astrophys. J. Suppl. Ser.* 6, 167 (1961).
22. V. L. Jacobs and J. Davis, *Phys. Rev. A* 13, 697 (1973).
23. L. A. Vainshtein and I. I. Sobel'man, *Lebedev Report No. 66* (1967).
24. J. Davis, P. C. Kepple, and M. Blaha, *J. Quant. Spectrosc. Radiat. Transfer* 16, 1043 (1976).
25. E. Oran and J. Davis, *J. Appl. Phys.* 45, 2480 (1974).
26. J. Davis, *J. Quant. Spectrosc. Radiat. Transfer* 14, 549 (1974).
27. D. R. Bates and A. Damgaard, *Phil. Trans. Roy. Socl London, Ser. A*, 242, 101 (1949).
28. A. Lindgård and S. E. Nielsen, *Atomic Data and Nuclear Data Tables* 19, 533 (1977).
29. B. C. Fawcett, *Atomic Data and Nuclear Data Tables* 22, 473 (1978).
30. I. Martin and G. Simons, *Mol. Phys.* 32, 1017 (1976).
31. L. J. Shamey, *J. Opt. Soc. Am.* 61, 942 (1971).
32. A. W. Weiss, *Phys. Rev. A* 188, 119 (1969).
33. L. C. McIntyre, Jr., D. J. Donahue, and E. M. Bernstein, *Physica Scripta* 17, 5 (1977).
34. J. P. Buchet and M. C. Buchet - Poulicac, *Phys. Lett.* 63A, 267 (1977).
35. J. A. Kernahan, E. H. Pinnington, J. A. O'Neill, R. L. Brooks, and K. E. Donnelly, *Physica Scripta* 19, 267 (1979).
36. R. Mewe, *Astron. Astrophys.* 59, 275 (1977).
37. P. Shorer, *Phys. Rev. A* 20, 642 (1979).
38. A. V. Loginov and P. F. Gruzdev, *Opt. Spectrosc. (USSR)* 45 (5), 725 (1978).
39. W. Wiese, M. Smith, and B. Miles, Atomic Transition Probabilities (U.S. GPO, Washington, D.C., 1969), Vol. II.
40. D. G. Hummer, *Astrophys. J.* 140, 276 (1964).
41. J. P. Apruzese, J. Davis, D. Duston, and K. G. Whitney, *J. Quant. Spectrosc. Radiat. Transfer* 23, 479 (1980).

References (continued)

42. Hans R. Griem, Plasma Spectroscopy (McGraw-Hill, New York, 1964).
43. J. Davis, NRL Memorandum Report No. 2655, 1973 (unpublished).
44. H. R. Griem, M. Blaha, and P. C. Kepple, Phys. Rev. A 19, 2421 (1979).
45. H. R. Griem, Spectral Line Broadening by Plasmas (Academic, New York, 1974).
46. J. C. Weisheit and B. F. Rozsnyai, J. Phys. B 9, L63, (1976).
47. Stanley Skupsky, Phys. Rev. A 21, 1316 (1980).
48. A. V. Vinogradov, I. Yu. Skobelev, and E. A. Yukov, Sov. J. Quant. Electron. 5, 630 (1975) and Sov. Phys. JETP 45, 925 (1977).
49. U. Feldman, G. A. Doschek, D. K. Prinz, and D. Nagel, J. Appl. Phys. 47, 1341 (1976).
50. C. P. Bhalla, A. H. Gabriel, and L. P. Presnyakov, Mon. Not. R. Astron. Soc. 172, 359 (1975).
51. H. J. Kunze, A. H. Gabriel, and H. R. Griem, Phys. Rev. 165, 267 (1968).
52. G. V. Peregudov, E. N. Ragozine, I. Yu. Skobelev, A. V. Vinogradov, and E. A. Yukov, J. Phys. D: Appl. Phys. 11, 2305 (1978).
53. V. A. Boiko, A. Yu. Chugunov, T. G. Ivanova, A. Ya. Faenov, I. V. Holin, S. A. Pikuz, A. M. Urnov, L. A. Vainshtein, and U. I. Safronova, Mon. Not. R. Astr. Soc. 185, 305 (1978).
54. N. A. Ebrahim, M. C. Richardson, G. A. Doschek and U. Feldman, J. Appl. Phys. 51, 182 (1980).
55. P. G. Burkhalter, D. Duston, and J. Davis (unpublished).

LIST OF TABLES

1. Atomic level structure for aluminum included in the collisional-radiative equilibrium model (brackets indicate levels which were grouped together in the calculation).
2. Transitions within the carbonlike Al VIII ion included in the CRE model (see Figure 3 for power densities).
3. Transitions comprising the temperature-sensitive line intensity ratios depicted in Figure 8.
4. Transitions comprising the density-sensitive line intensity ratios depicted in Figures 10-12.
5. Transitions shown in the spectral plots, Figs. 13 and 14 with their wavelengths (Note: wavelengths may be averages over several transitions within the same configuration) and their line-center optical depths measured from plasma center for the conditions described in Section V.

LEVEL	ENERGY (eV)	LEVEL	ENERGY (eV)
A1 I 1s <sup>2</sup> 2s <sup>2</sup> 2p <sup>5</sup> 3s <sup>2</sup> 3p <sup>2</sup> p	0.0	[2s <sup>2</sup> 2p <sup>3</sup> (2D)3d 3F 2s <sup>2</sup> 2p <sup>3</sup> (2D)3d 3D 2s <sup>2</sup> 2p <sup>3</sup> (2D)3d 3P 2s <sup>2</sup> 2p <sup>3</sup> (2D)3d 3S 2s <sup>2</sup> 2p <sup>3</sup> (2D)3d 1P 2s <sup>2</sup> 2p <sup>3</sup> (2D)3d 1D 2s <sup>2</sup> 2p <sup>3</sup> (2D)3d 1F]	140.55 140.63 141.50 141.97 140.86 141.57 142.56 144.43 144.80 144.95 145.14 145.30 145.56
A1 II 1s <sup>2</sup> 2s <sup>2</sup> 2p <sup>5</sup> 3s <sup>2</sup> 1s	0.0		
A1 III 1s <sup>2</sup> 2s <sup>2</sup> 2p <sup>6</sup> 3s <sup>2</sup> S 3p <sup>2</sup> P 3d <sup>2</sup> D 4s <sup>2</sup> S 4p <sup>2</sup> P 4d <sup>2</sup> D 4f <sup>2</sup> F	0.0 6.675 14.377 15.64 17.815 20.555 20.782	[2s <sup>2</sup> 2p <sup>3</sup> (2P)3d 3P 2s <sup>2</sup> 2p <sup>3</sup> (2P)3d 3F 2s <sup>2</sup> 2p <sup>3</sup> (2P)3d 3D 2s <sup>2</sup> 2p <sup>3</sup> (2P)3d 1D 2s <sup>2</sup> 2p <sup>3</sup> (2P)3d 1P 2s <sup>2</sup> 2p <sup>3</sup> (2P)3d 1F]	144.43 144.80 144.95 145.14 145.30 145.56
A1 IV 1s <sup>2</sup> 2s <sup>2</sup> 2p <sup>5</sup> 1s 2p <sup>5</sup> 3s <sup>3</sup> P 2p <sup>5</sup> 3s <sup>1</sup> P 2p <sup>5</sup> 3p <sup>1</sup> D 2p <sup>5</sup> 3p <sup>3</sup> P [2p <sup>5</sup> 3d <sup>3</sup> P 2p <sup>5</sup> 3d <sup>1</sup> P 2p <sup>5</sup> 3d <sup>3</sup> D 2p <sup>5</sup> 4s <sup>3</sup> P 2p <sup>5</sup> 4s <sup>1</sup> P	0.0 76.68 77.45 85.02 85.32 94.23 95.57 95.14 99.47 99.93	A1 VII 1s <sup>2</sup> 2s <sup>2</sup> 2p <sup>3</sup> 4S 2s <sup>2</sup> 2p <sup>3</sup> 2D 2s <sup>2</sup> 2p <sup>4</sup> 4P [2s <sup>2</sup> 2p <sup>4</sup> 2D 2s <sup>2</sup> 2p <sup>4</sup> 2S 2p <sup>5</sup> 2p <sup>2</sup> 2P 2s <sup>2</sup> 2p <sup>2</sup> 23s <sup>4</sup> P 3s <sup>2</sup> 2D 2s <sup>2</sup> 2p <sup>2</sup> (3P)3d 4D 2s <sup>2</sup> 2p <sup>2</sup> (3P)3d 4P 2s <sup>2</sup> 2p <sup>2</sup> (3P)3d 2F 2s <sup>2</sup> 2p <sup>2</sup> (1D)3d 2F 2s <sup>2</sup> 2p <sup>2</sup> (1D)3d 2D 2s <sup>2</sup> 2p <sup>2</sup> (1D)3d 2P 2s <sup>2</sup> 2p <sup>2</sup> (1D)3d 2S	0.0 7.73 11.75 34.92 47.84 56.17 59.35 91.39 142.53 148.58 164.15 164.59 163.35 164.50 166.85 169.66 170.02 171.15 171.97
A1 V 1s <sup>2</sup> 2s <sup>2</sup> 2p <sup>5</sup> 2P 2s <sup>2</sup> p <sup>5</sup> 2S 2s <sup>2</sup> 2p <sup>4</sup> 3s <sup>2</sup> P 2s <sup>2</sup> 2p <sup>4</sup> 3s <sup>2</sup> D 2s <sup>2</sup> 2p <sup>4</sup> 3s <sup>2</sup> S [2s <sup>2</sup> 2p <sup>4</sup> (3P)3d 2F 2s <sup>2</sup> 2p <sup>4</sup> (3P)3d 2D 2s <sup>2</sup> 2p <sup>4</sup> (3P)3d 2P [2s <sup>2</sup> 2p <sup>4</sup> (1D)3d 2S 2s <sup>2</sup> 2p <sup>4</sup> (1D)3d 2P 2s <sup>2</sup> 2p <sup>4</sup> (1D)3d 2D 2s <sup>2</sup> 2p <sup>4</sup> (1D)3d 2F	0.0 44.49 94.86 98.77 104.38 114.28 114.82 115.01 119.08 119.17 119.39 119.44	A1 VIII 1s <sup>2</sup> 2s <sup>2</sup> 2p <sup>2</sup> 3P [2s <sup>2</sup> 2p <sup>2</sup> 1D 2s <sup>2</sup> 2p <sup>2</sup> 1S 2s <sup>2</sup> 2p <sup>3</sup> 5S 2s <sup>2</sup> 2p <sup>3</sup> 3D 2s <sup>2</sup> 2p <sup>3</sup> 3S 2s <sup>2</sup> 2p <sup>3</sup> 1D 2s <sup>2</sup> 2p <sup>4</sup> 3P 2s <sup>2</sup> 2p <sup>4</sup> 1D 2s <sup>2</sup> 2p <sup>4</sup> 1S 2s <sup>2</sup> 2p <sup>3</sup> 3F 3D 3P 3S 1D 1P 1S 1D 1S 1P 1F 1P	0.0 5.97 11.93 16.55 32.51 38.33 50.11 49.22 55.12 75.58 80.25 91.56 182.10 184.21 184.87 182.50 187.12 187.23
A1 VI 1s <sup>2</sup> 2s <sup>2</sup> 2p <sup>4</sup> 3P [2s <sup>2</sup> 2p <sup>4</sup> 1D 2s <sup>2</sup> 2p <sup>4</sup> 1S 2s <sup>2</sup> 2p <sup>5</sup> 3P 2s <sup>2</sup> 2p <sup>5</sup> 1P [2s <sup>2</sup> 2p <sup>3</sup> 3S <sup>3</sup> S 2s <sup>2</sup> 2p <sup>3</sup> 3S <sup>3</sup> D 2s <sup>2</sup> 2p <sup>3</sup> 3S <sup>3</sup> P [2s <sup>2</sup> 2p <sup>3</sup> 3S <sup>1</sup> D [2s <sup>2</sup> 2p <sup>3</sup> 3S <sup>1</sup> P 2s <sup>2</sup> 2p <sup>3</sup> (4S)3d 3D	0.0 5.104 10.937 40.20 55.97 113.21 119.16 123.21 120.31 124.39 133.85		

TABLE I (continued)

LEVEL	ENERGY (eV)	LEVEL	ENERGY (eV)
$2s2p^2(^2D)3s\ ^3D$	196.57	$2p3s\ ^1P$	259.36
$2s2p^2(^4P)3d\ ^5D$	202.37	$2p3p\ ^1P$	259.73
$2s2p^2(^4P)3d\ ^3D$	202.70	$2p3d\ ^1D$	266.58
$2s2p^2(^4P)3d\ ^3F$	203.93	$2p3d\ ^3D$	265.53
$2s2p^2(^2D)3d\ ^3D$	206.46	$2p3d\ ^1F$	271.89
$2s2p^2(^2D)3d\ ^3F$	215.00	$2p3d\ ^1P$	272.73
$2s2p^2(^2D)3d\ ^3D$	216.01		
$2s2p^2(^2D)3d\ ^3P$	216.81		
$2s2p^2(^2D)3d\ ^3S$	218.47		
<b>A1 IX</b>		<b>A1 XI</b>	
$1s^22s^22p\ ^2P$	0.0	$1s^22s\ ^2S$	0.0
$2s2p^2\ ^4P$	18.236	$2p\ ^2P$	22.30
$2p\ ^2D$	32.205	$3s\ ^2S$	250.51
$2s\ ^2S$	41.25	$3p\ ^2P$	256.64
$2p\ ^2P$	44.14	$3d\ ^2D$	258.93
$2p^3\ ^4S$	57.04	$4s\ ^2S$	335.47
$2p\ ^2D$	64.49	$4p\ ^2P$	338.07
$2p\ ^2P$	72.58	$4d\ ^2D$	339.02
$2s^23s\ ^2S$	186.11	$4f\ ^2F$	339.10
$2s^23p\ ^2P$	195.11	$5s\ ^2S$	374.40
$2s^23d\ ^2D$	203.62	$5p\ ^2P$	375.64
$2s2p3d\ ^4P$	223.94	$5d\ ^2D$	376.14
$4D$	222.94	$5f\ ^2F$	376.16
$2s2p(^3P)3d\ ^2D$	223.27	$5g\ ^2G$	376.17
$2p\ ^2F$	227.28	$6s\ ^2S$	395.26
$2p\ ^2P$	228.26	$6p\ ^2P$	395.96
$2s2p(^1P)3d\ ^2F$	239.67	$6d\ ^2D$	396.31
$2p\ ^2D$	240.98	$6f\ ^2F$	396.32
$2p\ ^2P$	242.36	$6g\ ^2G$	396.36
$2s2p4d\ ^4D$	279.46	$6h\ ^2H$	396.38
$4P$	279.79	$1s2p^2\ ^2D$	1596.70
<b>A1 X</b>		<b>A1 XII</b>	
$1s^22s^2\ ^1S$	0.0	$1s^2\ ^1S$	0.0
$2s2p\ ^3P$	19.67	$1s2s\ ^3S$	1575.06
$2s2p\ ^1P$	37.26	$1s2p\ ^3P$	1588.5
$2p^2\ ^3P$	50.59	$1s2s\ ^1S$	1589.03
$2p^2\ ^1D$	55.76	$1s2p\ ^1P$	1598.37
$2p^2\ ^1S$	68.66	$n=3$ , triplet	1866.08
$2s3s\ ^3S$	230.09	$n=3$ , singlet	1868.63
$2s3p\ ^3P$	239.16	$n=4$ , singlet	1963.89
$2s3d\ ^3D$	243.77	$n=5$ , singlet	2006.47
$2s3s\ ^1S$	233.64		
$2s3p\ ^1P$	238.53		
$2s3d\ ^1D$	247.02		
$2p3s\ ^3D$	255.06		
$2p3p\ ^3D$	261.02	<b>A1 XIII</b>	
$3S$	262.81	$n=1$ , doublet	0.0
$3P$	264.06	$n=2$ , doublet	1728.71
$2p3d\ ^3D$	268.10	$n=3$ , doublet	2048.57
$3P$	269.14	$n=4$ , doublet	2160.66
		$n=5$ , doublet	2212.31

TABLE II

KEY	TRANSITION		
1	$2s^2 2p^2 (^3P)$	-	$2s2p^3 (^3S, ^3P, ^3D)$
2	$2s^2 2p^2 (^1S, ^1D)$	-	$2s2p^3 (^1P, ^1D)$
3	$2s2p^3 (^3S, ^3P, ^3D)$	-	$2p^4 (^3P)$
4	$2s2p^3 (^1P, ^1D)$	-	$2p^4 (^1S, ^1D)$
5	$2s^2 2p^2 (^3P)$	-	$2s^2 2p3d (^3P, ^3D)$
6	$2s^2 2p^2 (^1S, ^1D)$	-	$2s^2 2p3d (^1P, ^1D, ^1F)$
7	$2s2p^3 (^3P, ^3D)$	-	$2s2p^2 (^2D) 3s (^3D)$
8	$2s2p^3 (^3S)$	-	$2s2p^2 3d (^5P)$
9	$2s2p^3 (^3P, ^3D)$	-	$2s2p^2 (^4P) 3d (^3P, ^3D, ^3F)$
		-	$2s2p^2 (^2D) 3d (^3S, ^3P, ^3D, ^3F)$

TABLE III

Key	Ion	Transition	Wavelengths $\text{\AA}^o$
(1)	Al IV	$2s^2 2p^6 (1S)$ - $2s^2 2p^5 3d (3D)$	129.729
	Al V	$2s^2 2p^5 (2P)$ - $2s 2p^4 (3P) 3s (2P)$	130.413, 130.848, 131.003, 131.441
(2)	Al VI	$2s^2 2p^5 (2P)$ - $2s 2p^4 (3P) 3d (2D)$	107.945, 108.057, 108.462
	Al VII	$2s^2 2p^4 (3P)$ - $2s^2 2p^3 (4S) 3s (3S)$	109.514, 109.843, 109.974
(3)	Al VIII	$2s^2 2p^4 (3P)$ - $2s^2 2p^3 (4S) 3d (3D)$	92.626, 92.636, 92.875, 92.97
	Al IX	$2s^2 2p^3 (2P)$ - $2s^2 2p^2 (1D) 3s (2D)$	90.63
(4)	Al X	$2s^2 2p^3 (4S)$ - $2s^2 2p^2 (3P) 3d (4P)$	75.27, 75.320, 75.36
	Al XI	$2s 2p^3 (3D)$ - $2s 2p^2 (2D) 3s (3D)$	75.577
(5)	Al XII	$2s 2p^3 (5S)$ - $2s 2p^2 (4P) 3d (5P)$	66.704, 66.731, 66.771
	Al XIII	$2s^2 2p (2P)$ - $2s^2 3s (2S)$	66.624, 66.836
(6)	Al XIV	$2s 2p^2 (4P)$ - $2s 2p 3d (4D)$	60.504, 60.549, 60.588, 60.645
	Al XV	$2s 2p (1P)$ - $2s 3d (1D)$	59.107
(7)	Al XVI	$2s^2 (1S)$ - $2s 3p (1P)$	51.979
	Al XVII	$2p (2P)$ - $3s (2S)$	54.39

TABLE IV

ION	TRANSITION	WAVELENGTHS (Å)
Al VII	$2s^2 2p^3(^4S) - 2s^2 2p^2 3s(^4P)$	86.887, 87.06, 87.176
Al VII	$2s^2 2p^3(^2D) - 2s^2 2p^2(^1D) 3s(^2D)$	88.033
Al VIII	$2s^2 2p^2(^3P) - 2s^2 2p 3d(^3D)$	67.36, 67.408, 67.437, 67.464, 67.529
Al VIII	$2s 2p^3(^5S) - 2s 2p^2 3d(^5P)$	66.704, 66.731, 66.771
Al X	$2s 2p(^1P) - 2s 3d(^1D)$	59.107
Al X	$2s 2p(^3P) - 2s 3d(^3D)$	55.227, 55.272, 55.376

TABLE V

<u>KEY</u>	<u>TRANSITION</u>	<u>WAVELENGTH (Å)</u>	<u>T<sub>2</sub></u>
1.	Al XI    2s-6p	31.31	7.3
2.	Al XI    2s-5p	33.007	14.7
3.	Al XI    2p-6s, - 6d	33.109	20.4
4.	Al XI    2p-5s, - 5d	34.994	44.0
5.	Al XI    2s-4p	36.675	38.5
6.	Al XI    2p-4s, - 4d	39.28	132.6
7.	Al XI    2s-3p	48.297	193.2
8.	Al X    2s2p-2p3p	50.47	70.2
9.	Al X    2s <sup>2</sup> -2s3p	51.096	147.1
10.	Al XI    2p-3d	52.299	937.2
11.	Al X    2s2p-2p3p	53.83	25.3
12.	Al XI    2p-3s	54.388	31.1
13.	Al X    2s2p-3s, - 3d	56.06	195.4
14.	Al X    2p <sup>2</sup> -2p3s, - 3d	57.74	418.0
15.	Al X    2p <sup>2</sup> -2p3s, - 3d	59.1	157.3
16.	Al X    2s2p-2s3d, - 3s	60.36	353.8
17.	Al IX    2p-3s, - 3d	62.37	786.6
18.	Al IX    2s2p <sup>2</sup> -2s2p3d	62.97	206.7
19.	Al VIII    2s2p <sup>3</sup> -2s2p <sup>2</sup> 3d	66.72	47.7
20.	Al VIII    2p <sup>2</sup> -2p3d	67.62	995.0
21.	Al VIII    2p <sup>2</sup> -2p3d	69.36	560.0
22.	Al VIII    2s2p <sup>3</sup> -2s2p <sup>2</sup> 3d	71.27	191.1
23.	Al VII    2p <sup>3</sup> -2p <sup>2</sup> 3d	75.32	647.4
24.	Al VII    2p <sup>3</sup> -2p <sup>2</sup> 3d	76.17	406.0
25.	Al VIII    2s2p <sup>3</sup> -2s2p <sup>2</sup> 3s	77.92	44.4
26.	Al VII    2p <sup>3</sup> -2p <sup>2</sup> 3d	78.10	116.8
27.	Al VII    2p <sup>3</sup> -2p <sup>2</sup> 3d	78.93	61.5
28.	Al VII    2p <sup>3</sup> -2p <sup>2</sup> 3d	81.02	338.1
29.	Al XI    3s-6p	85.19	0.9
30.	Al VI    2p <sup>4</sup> -2p <sup>3</sup> 3d	86.84	102.1
31.	Al VII    2p <sup>3</sup> -2p <sup>2</sup> 3s	87.07	94.0
32.	Al VII    2p <sup>3</sup> -2p <sup>2</sup> 3s	88.04	19.1

Table V (continued)

<u>KEY</u>	<u>TRANSITION</u>	<u>WAVELENGTH (Å)</u>	<u><math>\gamma_{\alpha}</math></u>
33.	AL XI    3p-6s, - 6d	83.90	3.5
34.	AL VI    2p <sup>4</sup> -2p <sup>3</sup> 3d	90.19	54.3
35.	AL XI    3d-6p, -6f	90.44	5.1
36.	AL VII    2p <sup>3</sup> -2p <sup>2</sup> 3s	90.64	6.9
37.	AL VI    2p <sup>4</sup> -2p <sup>3</sup> 3d	92.65	260.3
38.	AL XI    3s-5p	99.59	2.4
39.	AL VI    2p <sup>4</sup> -2p <sup>3</sup> 3s	103.46	57.7
40.	AL V    2p <sup>5</sup> -2p <sup>4</sup> 3d	103.92	7.00
41.	AL XI    3p-5s, - 5d	104.82	10.1

FIGURE CAPTIONS

- Figure 1. Total line emission power coefficient vs. electron temperature for densities from  $10^{11}$  -  $10^{13}$  ions/cm<sup>3</sup> (optically thin approximation).
- Figure 2. Ionic line emission power densities vs. electron temperature for a plasma at  $10^{19}$  ions/cm<sup>3</sup> (optically thin approximation); total L-shell emission is also shown (broken line).
- Figure 3. Individual line emission power densities for Al VIII (carbonlike) vs. electron temperature for a plasma at  $10^{19}$  ions/cm<sup>3</sup> (optically thin approximation). See Table II for line identifications.
- Figure 4. Comparison of CRE (solid) and LTE (broken) line emission power coefficients for plasma densities from  $10^{19}$  -  $10^{23}$  ions/cm<sup>3</sup> (optically thin approximation).
- Figure 5. Total line emission power densities (with opacity effects) for a plasma cylinder at  $10^{19}$  ions/cm<sup>3</sup> and radii from 50 - 5000 μm.
- Figure 6. Total free-bound continuum emission power densities (with opacity effects) for a plasma cylinder at  $10^{19}$  ions/cm<sup>3</sup> and radii from 50 - 5000 μm.
- Figure 7. Total line plus continuum emission power density (with opacity effects) for a plasma cylinder at  $10^{19}$  ions/cm<sup>3</sup> and radii from 50 - 5000 μm. Power density from similar plasmas in the black-body limit are also shown (straight curves in upper left).
- Figure 8. Temperature-sensitive line intensity ratios for selected L-shell lines at  $10^{19}$  ions/cm<sup>3</sup> (optically thin approximation).
- Figure 9. Line intensity ratio for the  $2p-3s/2s^2-2s3p(^1P)$  transitions for densities of  $10^{17}$ ,  $10^{19}$  and  $10^{21}$  ions/cm<sup>3</sup> (optically thin approximation) and for a plasma cylinder at  $10^{19}$  ions/cm<sup>3</sup> (with opacity effects) for radii of 50 - 5000 μm.
- Figure 10. Line intensity ratio for the  $2s2p(^1P)-2s3d(^1D)/2s2p(^3P)-2s3d(^3D)$  transitions vs. ion density, for several electron temperatures (optically thin approximation).
- Figure 11. Line intensity ratio for the  $2s^22p^2(^3P)-2s^22p3d(^3D)/2s2p^3(^5S)-2s2p^23d(^5P)$  transitions vs. ion density, for several electron temperatures (optically thin approximation).
- Figure 12. Line intensity ratio for the  $2s^22p^3(^4S)-2s^22p^23s(^4P)/2s^22p^3(^2D)-2s^22p^2(^1D)3s(^2D)$  transitions vs. ion density, for several electron temperatures (optically thin approximation).

Figure Captions (continued)

Figure 13. Aluminum spectrum from 30-65 angstroms for a plasma at  $10^{19}$  ions/cm<sup>3</sup> and a linear temperature gradient from 30 to 80 eV.

Figure 14. Aluminum spectrum from 65-105 angstroms for a plasma at  $10^{19}$  ions/cm<sup>3</sup> and a linear temperature gradient from 30 to 80 eV.

Figure 15. Aluminum spectrum from 0-700 angstroms for a plasma at  $10^{19}$  ions/cm<sup>3</sup> and a linear temperature gradient from 30 to 80 eV.

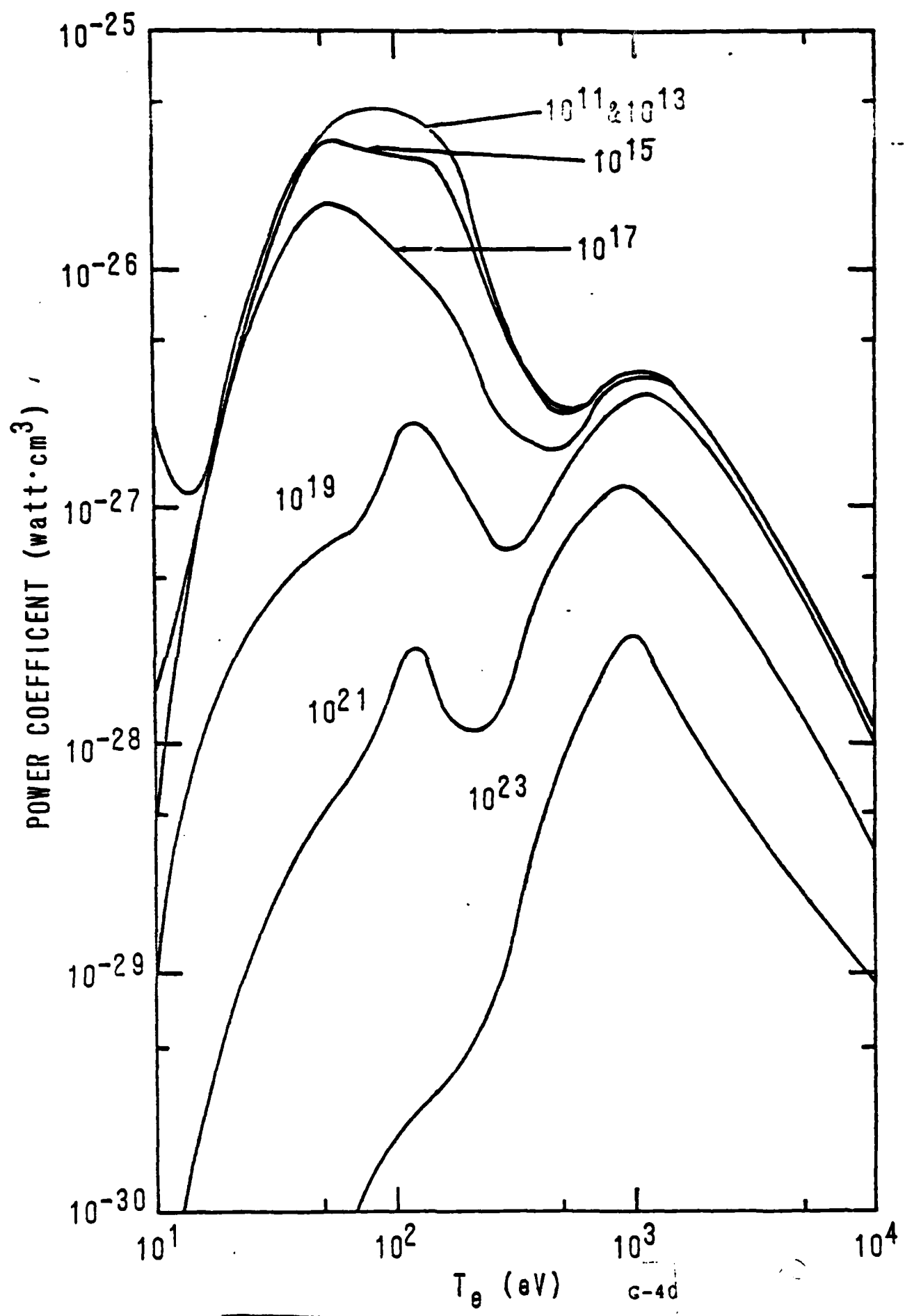


Fig. 1

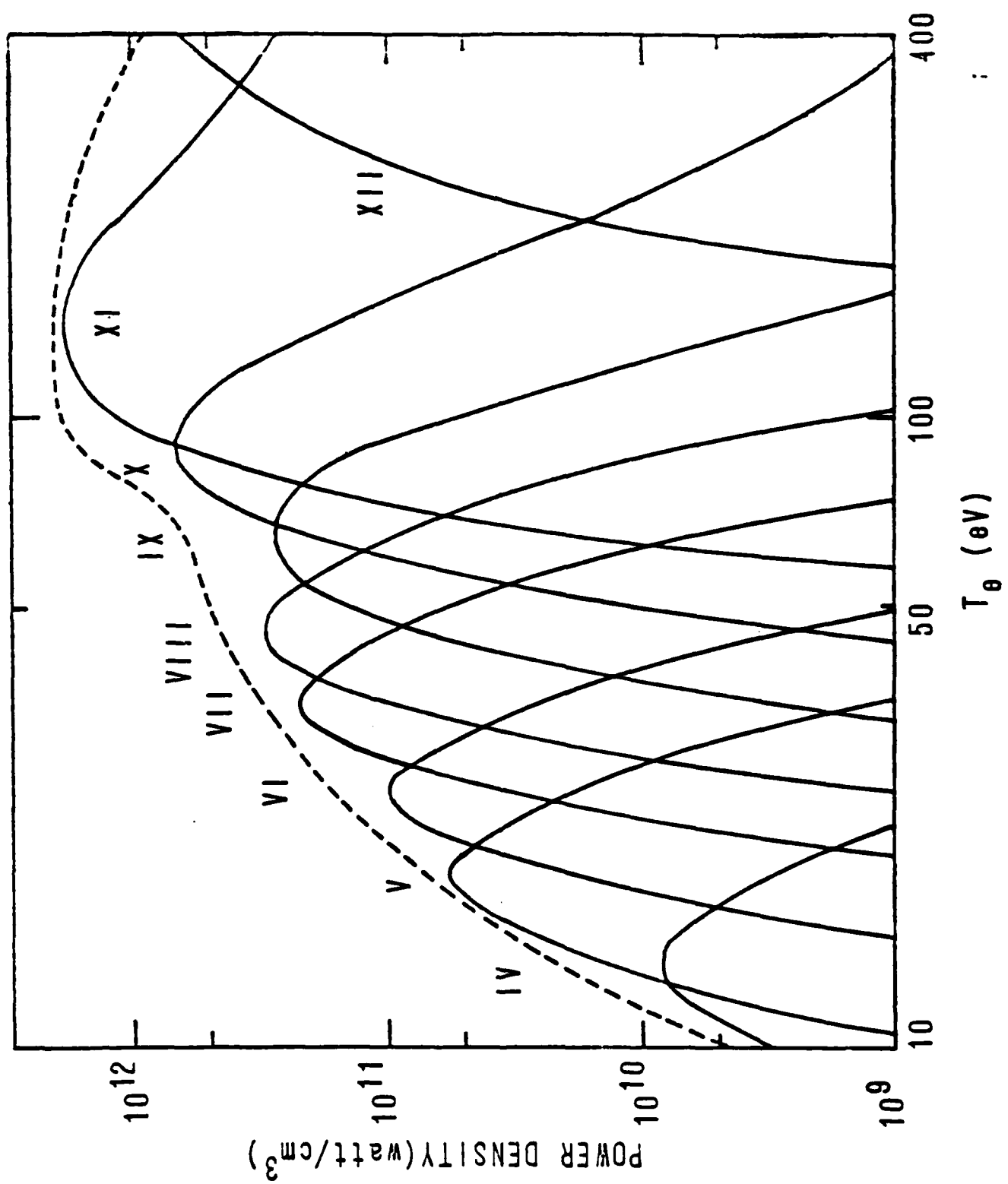
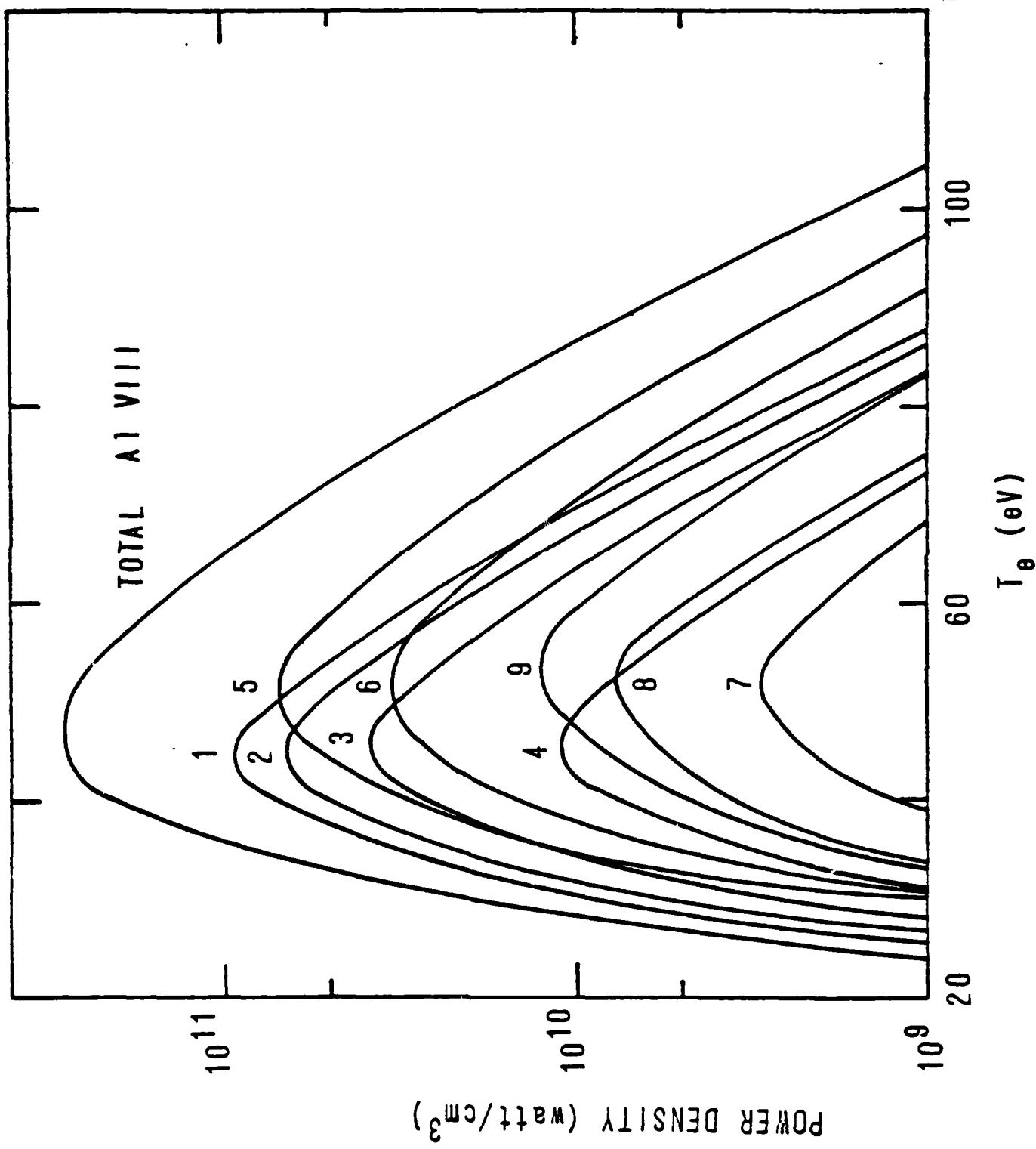


Fig. 2

Fig. 3



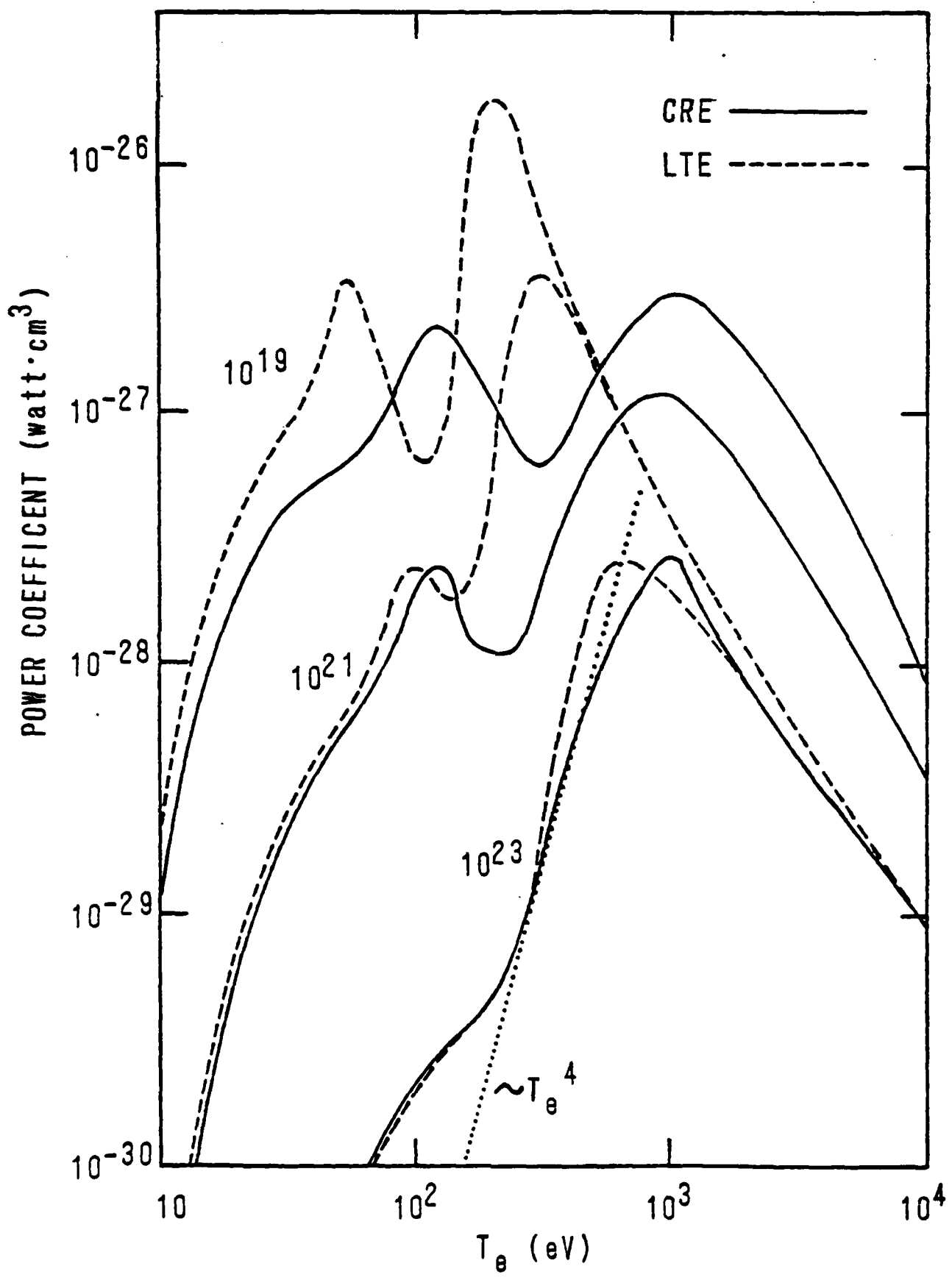


FIG. 4

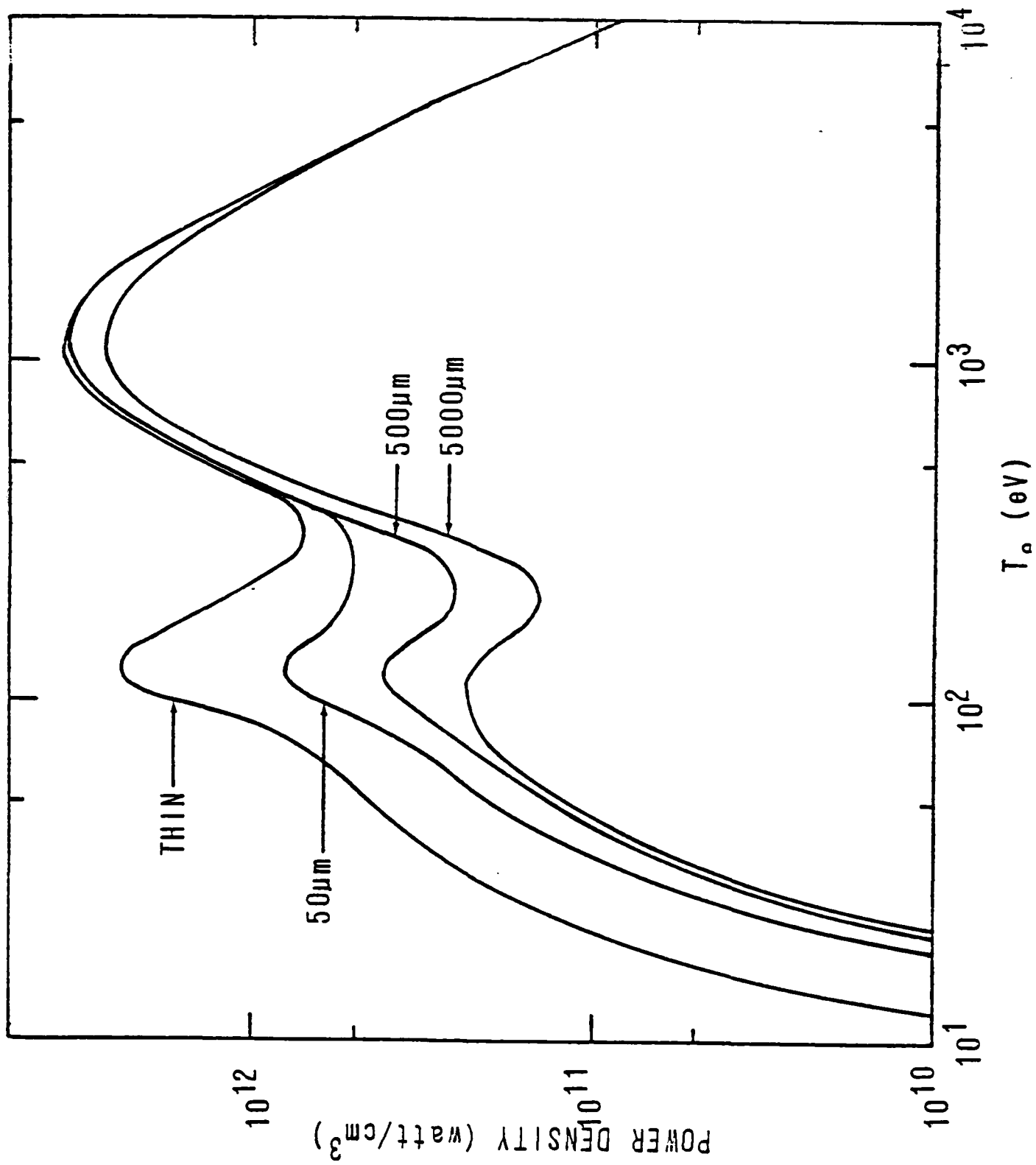
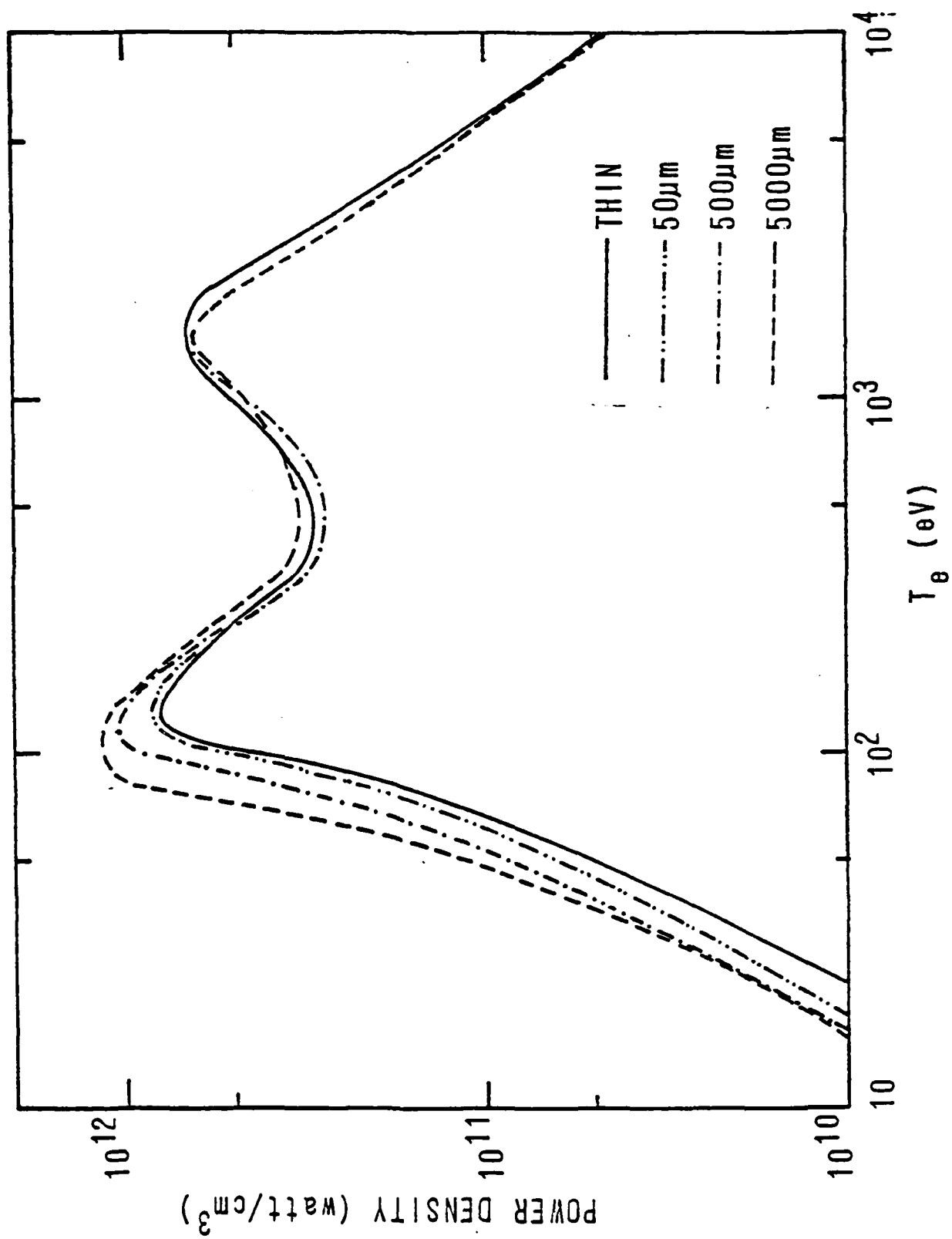


Fig. 5

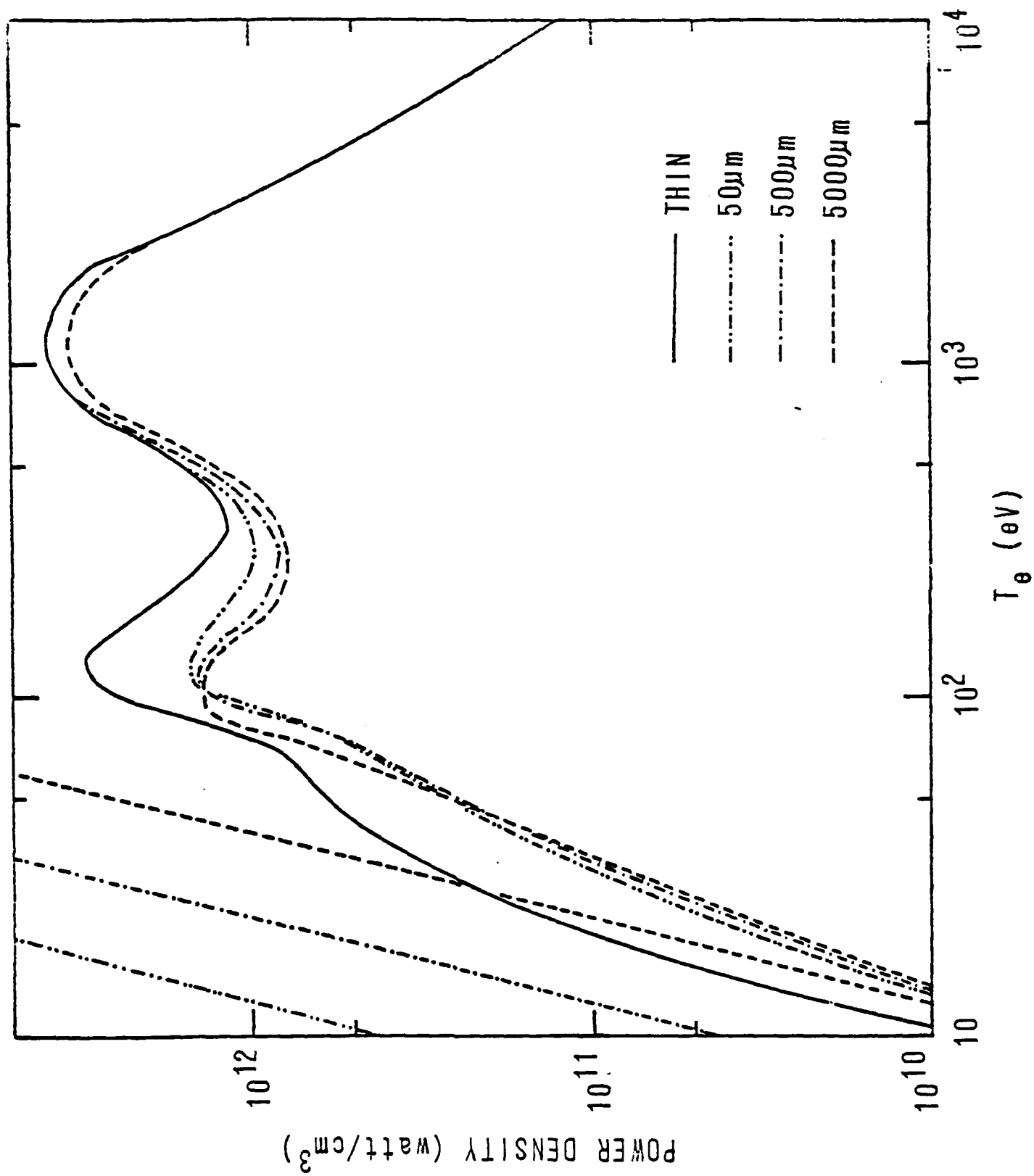
C-44



POWER DENSITY (Watt/cm<sup>3</sup>)

C-45

Fig. 7



POWER DENSITY (Watt/cm<sup>3</sup>)

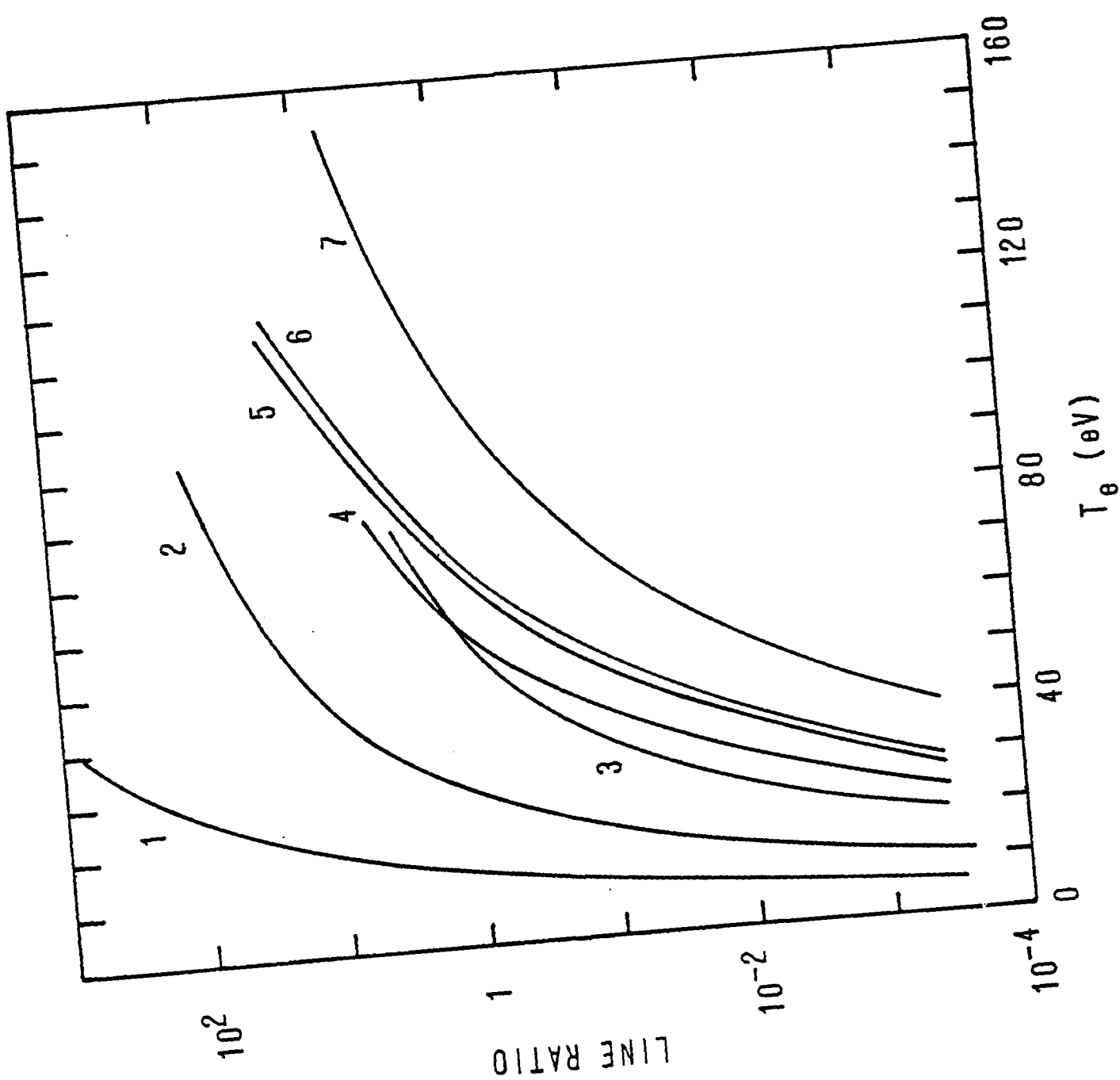
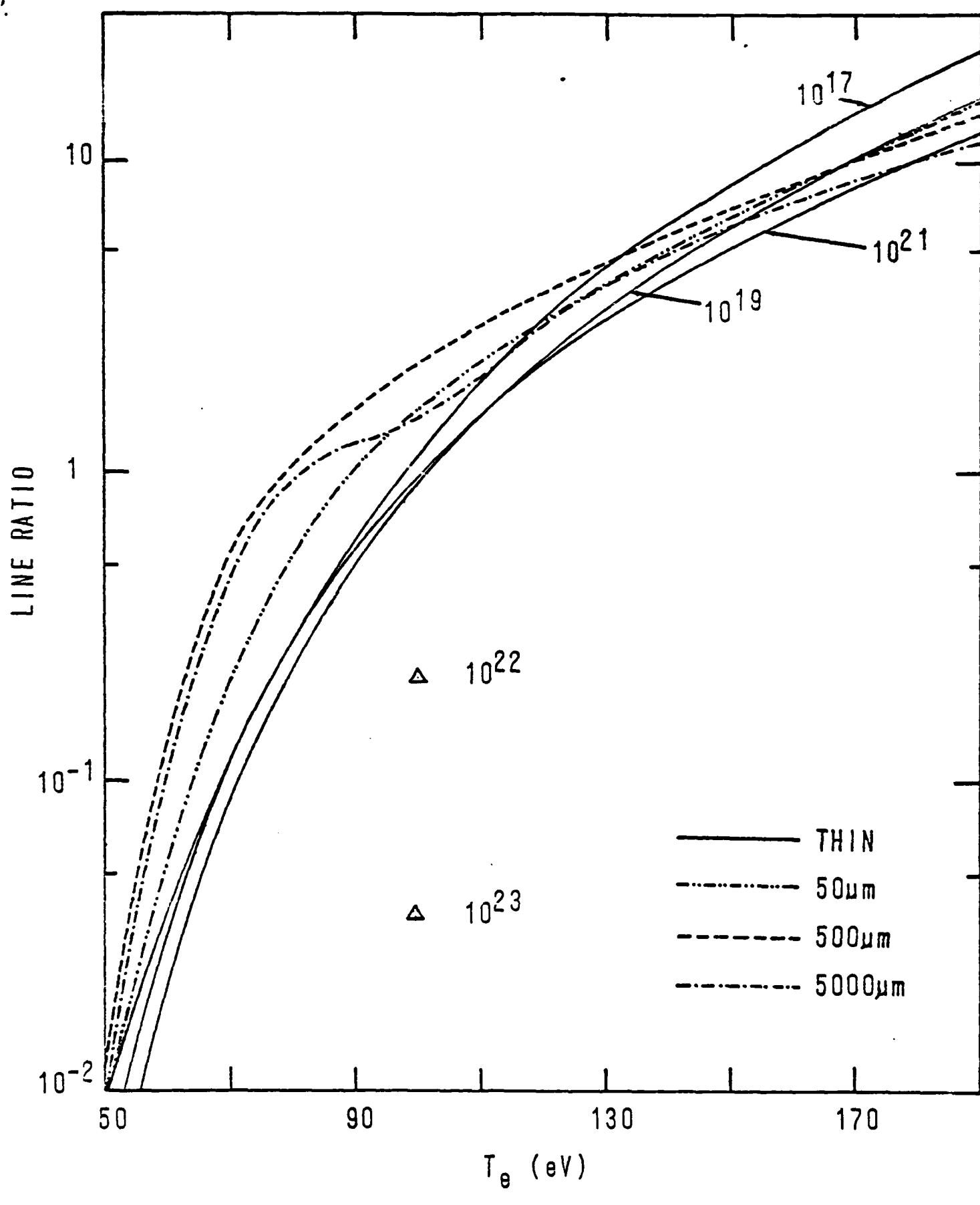


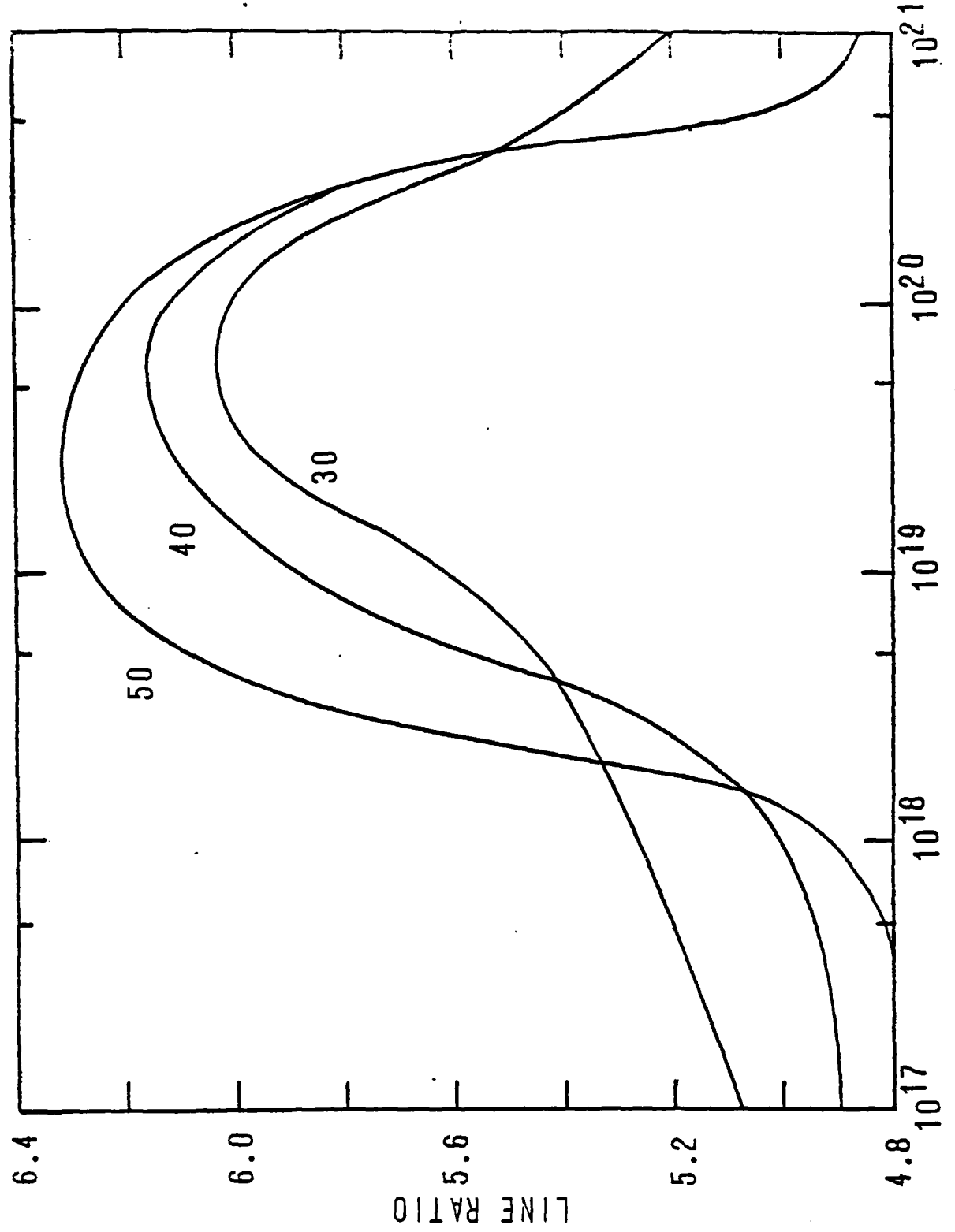
Fig. 8

C-47

Fig. 9



C-48



C-49

Fig. 10

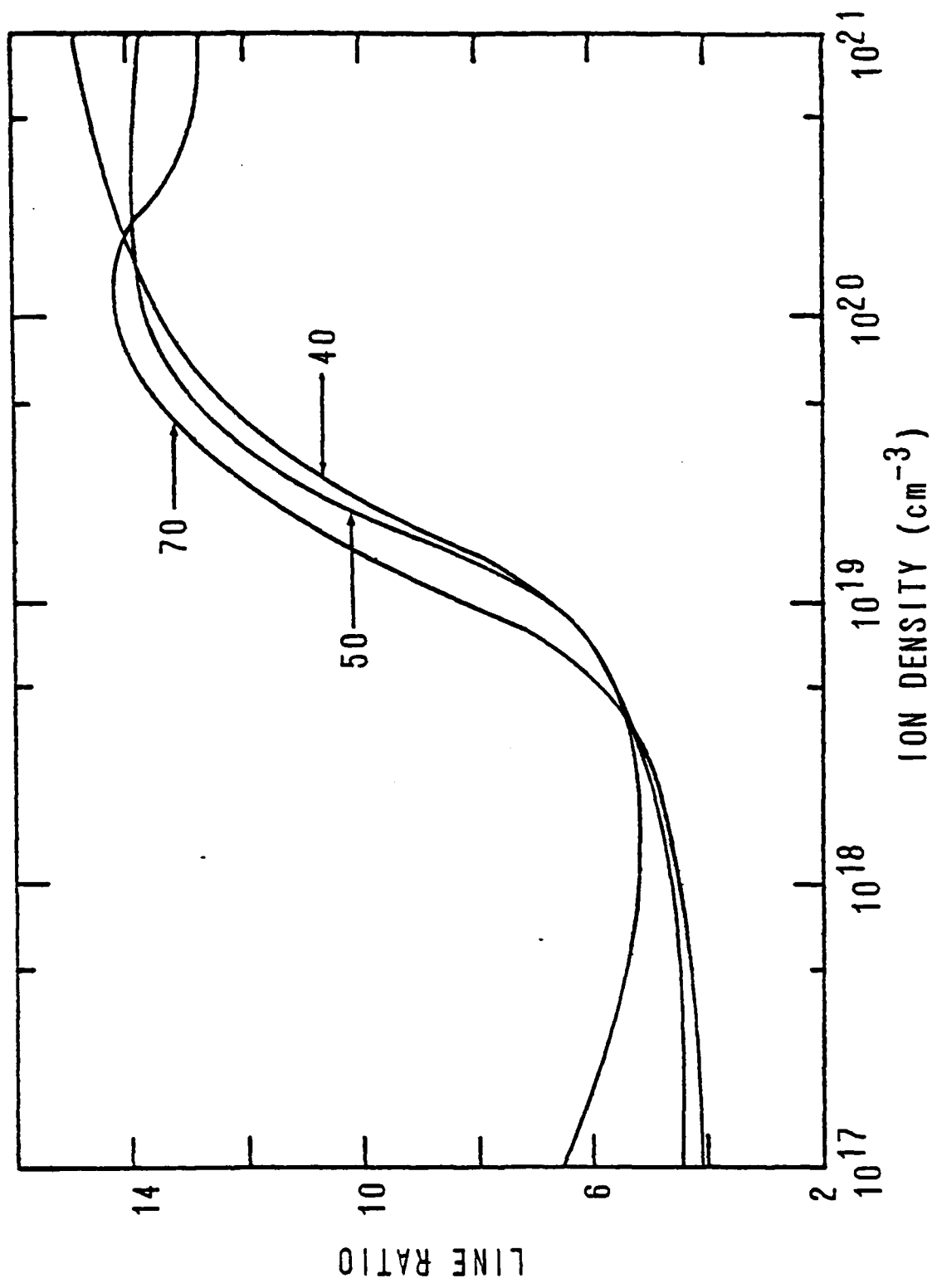


Fig. 11

C-50

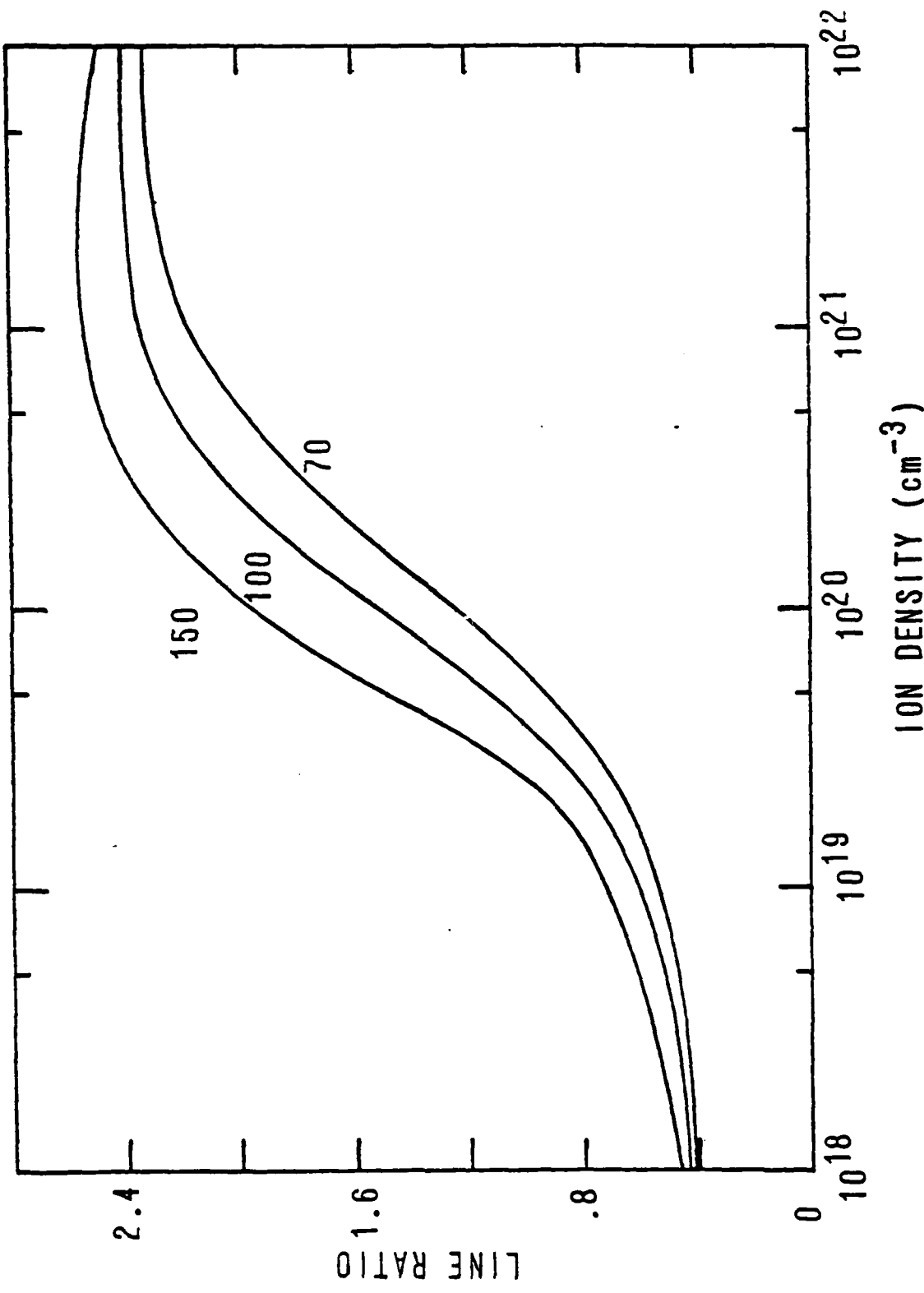


Fig. 12

C-51

Fig. 13

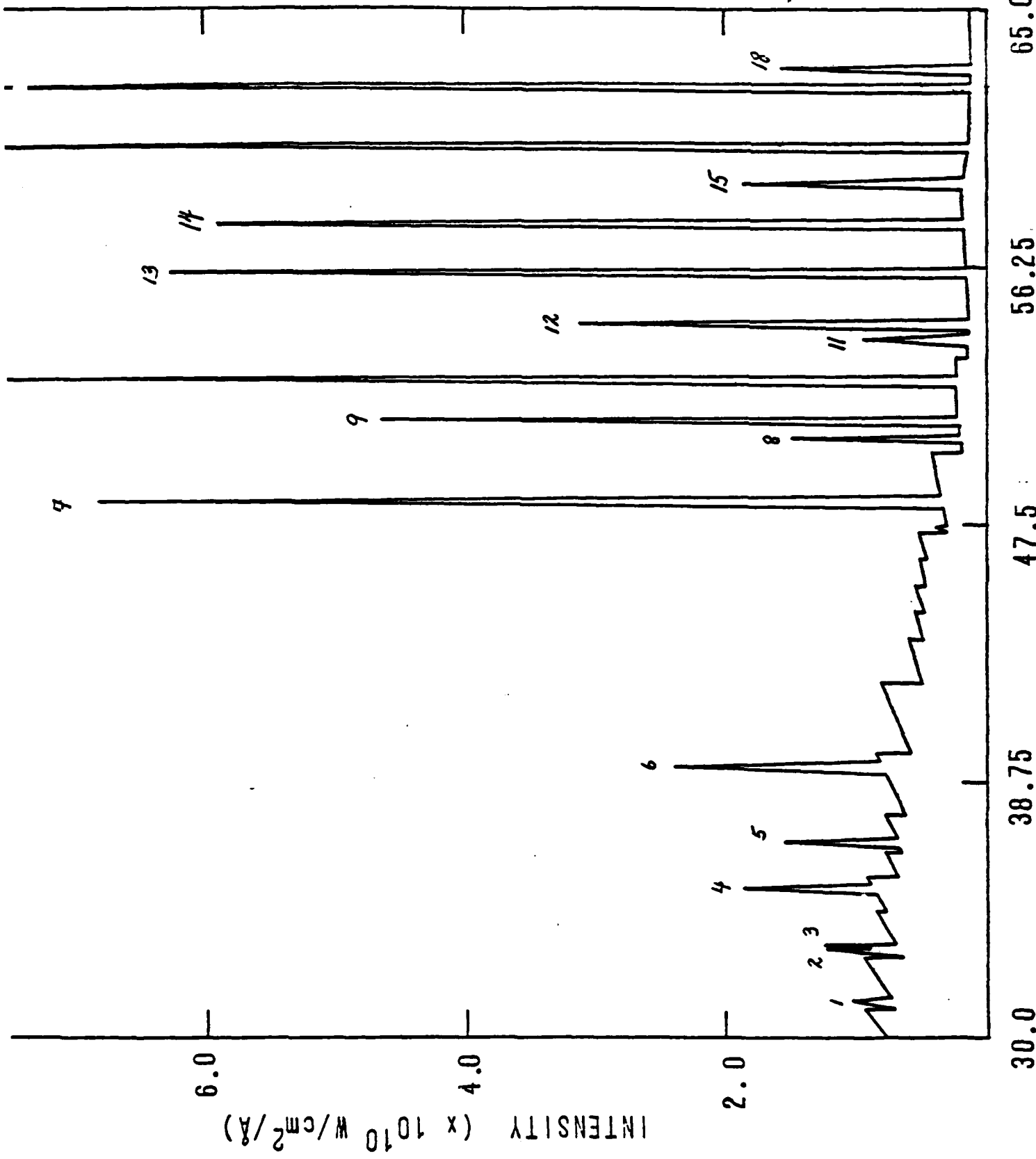


Fig. 14

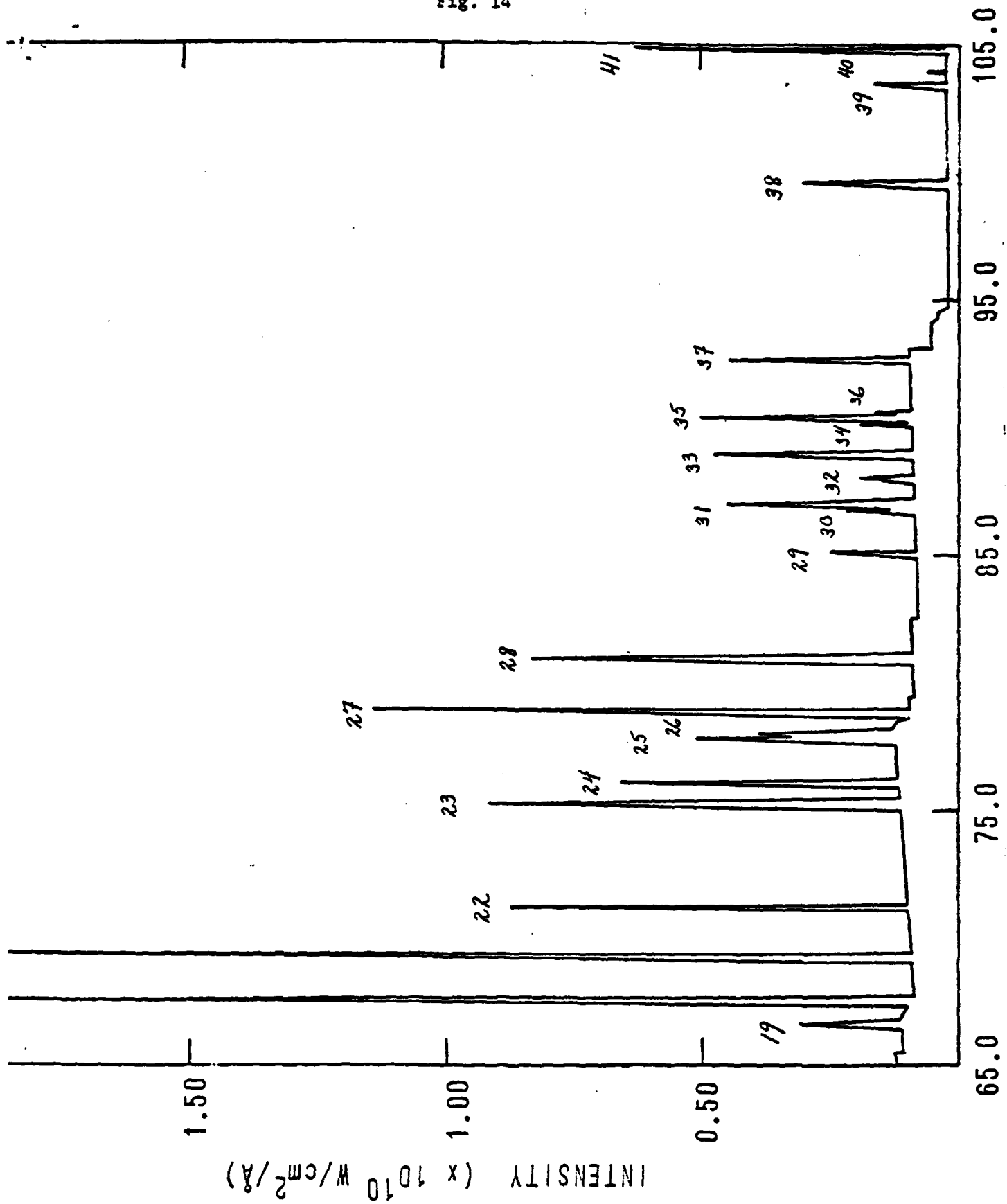
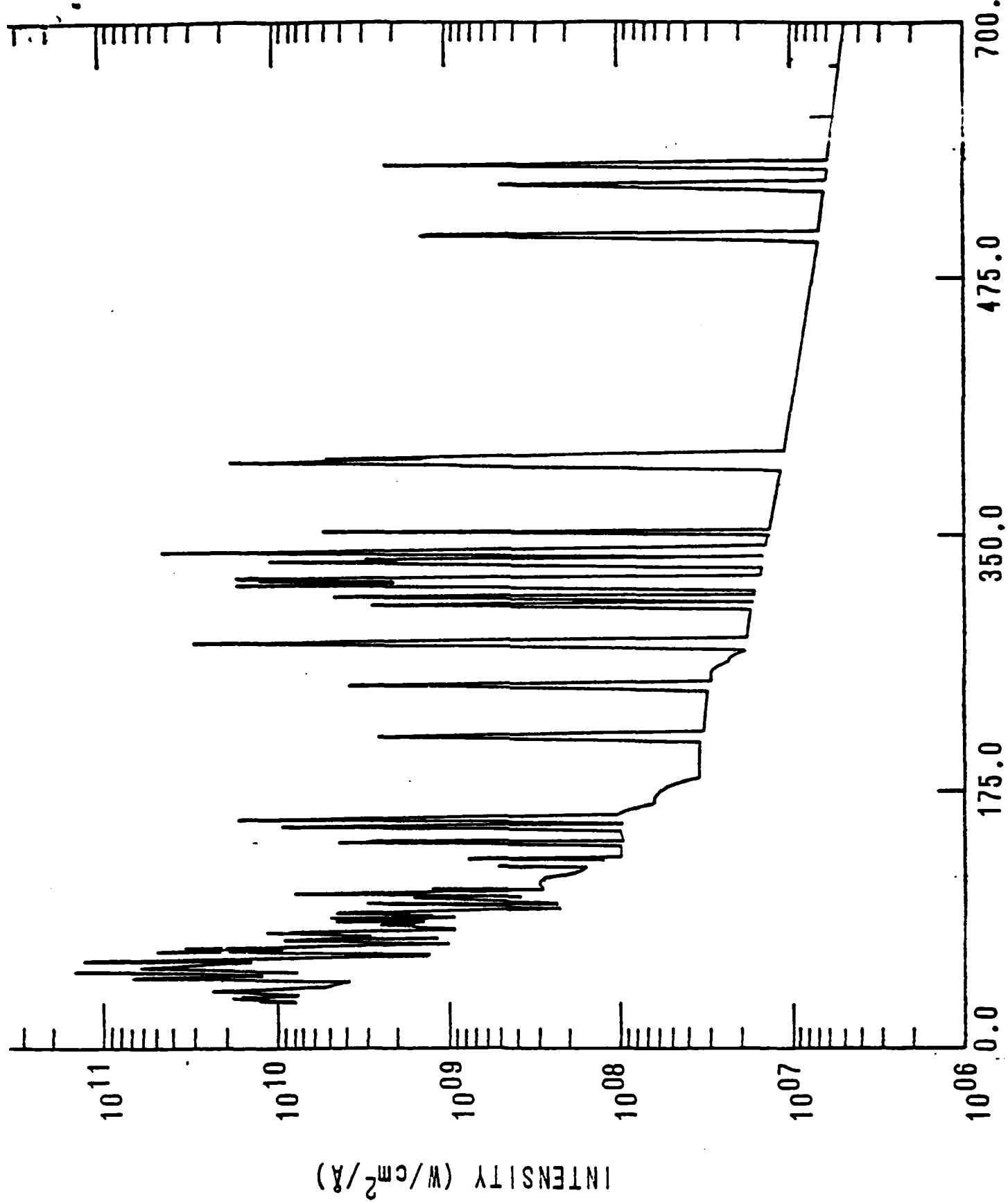


Fig. 15



APPENDIX D

Ms. Miriam Gersten  
Maxwell Laboratories  
9244 Balboa Avenue  
San Diego, California 92123

Dear Miriam:

I've enclosed a brief calculation that compares the optimum radiation emission one could expect from a boron plasma radiating in the K-shell and an aluminum plasma radiating in the L-shell. The information sources are:

Boron - "Systematic Trends in the Radiative Emission Rates for Low- and Medium-Z Elements in High-Temperature Plasmas", J. Davis and V. L. Jacobs (to be published in JQSRT).

Aluminum - "Soft X-ray and XUV Production from High Density, High-Temperature Aluminum Plasmas", D. Duston and J. Davis (submitted for publication).

The boron K-shell line emission peaks at 80 eV and the power coefficient there is  $1.3 \times 10^{-28}$  watt  $\cdot$  cm<sup>3</sup>.

The aluminum L-shell line emission peaks at 120 eV and the power coefficient is  $2 \times 10^{-27}$  watt  $\cdot$  cm<sup>3</sup>.

For equal radiation output as an aluminum plasma at  $10^{19}$  ions/cm<sup>3</sup> the following boron density is required:

$$(1.3 \times 10^{-28}) N_e N_i (\text{boron}) = (2 \times 10^{-27}) N_e^2 N_i^2 (\text{aluminum})$$

for boron  $N_e \approx 4.5 N_i$  in the K-shell; for aluminum  $N_e \approx 10 N_i$  in the L-shell (lithiumlike)

Hence,

$$N_i (\text{boron}) = \left[ \frac{(2 \times 10^{-27}) (10) N_i^2 (\text{aluminum})}{(1.3 \times 10^{-28}) (4.5)} \right]^{\frac{1}{2}}$$

or,

$$N_i (\text{boron}) = 5.84 N_i (\text{aluminum})$$

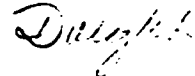
for equal line emission.

There are 3 contingencies, however:

1. Both calculations are done "optically thin"; we expect the attenuation due to opacity to affect both plasmas equally though.
2. Continuum photons are not included; our best guess indicates that there will be more Al L-shell continuum than B K-shell, though.
3. If your Al plasma was cooler than 120 eV, the L-shell would not be radiating optimally, and it's possible your boron plasma emission could be comparable.

The conclusion is, the lower-Z stuff shouldn't produce XUV from the K-shell as efficiently as medium-Z does from the L-shell.

Sincerely,



Dwight Duson

Science Applications, Inc

**APPENDIX E**

## DIRECT SOLUTION OF THE EQUATION OF TRANSFER USING FREQUENCY- AND ANGLE-AVERAGED PHOTON ESCAPE PROBABILITIES, WITH APPLICATION TO A MULTISTAGE, MULTILEVEL ALUMINUM PLASMA

J. P. APRUESE,† J. DAVIS, D. DUSTON,† and K. G. WHITNEY‡

Naval Research Laboratory, Plasma Radiation Group, Washington, DC 20375, U.S.A.

(Received 17 August 1979)

**Abstract**—A formalism is developed which permits direct steady-state solution of the transfer equation using escape probabilities averaged over angle and frequency. A matrix of probability-based coupling coefficients, which are related to the kernel function  $K_{ij}$ , is used to obtain the source function for a Doppler profile in plane-parallel geometry. Comparison is made with exact solutions, establishing the high accuracy of the technique. The method is extendable to different physical situations by simply modifying the coupling coefficients. As an example of a more realistic application of the formalism, we have solved for the ionization-excitation state of a planar aluminum plasma at 600 eV in collisional-radiative equilibrium. The results agree well with those obtained from the conventional multifrequency-multiangle formalism. Additionally, we have used the technique to gauge the effects of transport of lines connecting excited states with each other.

### I. INTRODUCTION

In the literature of radiative transfer theory, much attention has been devoted to photon escape-probability concepts as a means of aiding in the interpretation of detailed solutions to the transfer equation in astrophysical and laboratory contexts. In this paper, we develop a formalism which permits utilization of such concepts to obtain direct solutions of the steady-state source function. When applied to a plane-parallel, Doppler-broadened medium, the technique eliminates entirely the need for either frequency or angle integration, while yielding generally excellent agreement with previous results obtained by Avrett and Hummer.<sup>1</sup>

### 2. MULTICELL RADIATIVE COUPLING EQUATIONS

If a medium which is finite in extent in at least one direction is divided into a number  $N$  of smaller regions, line photons emitted in each region will have a finite probability of being absorbed in any of the other  $N - 1$  regions, as well as being reabsorbed in the local region or escaping entirely from the medium. Let  $C_{ij}$  be the probability that a line photon emitted in geometrical region  $i$  traverses the distance between regions  $i$  and  $j$  and is absorbed in region  $j$ .  $N_{ui}$  will refer to the total upper level population of region  $i$ , and  $A_{ui}$  stands for the spontaneous transition probability ( $\text{sec}^{-1}$ ) for the line in question. In each region  $i$ ,  $W_i$  and  $D_i$  will stand for the total collisional population and depopulation rates, respectively, of the upper level ( $N_{ui}$ ). The above concepts and notation clearly imply the following equation for the rate of change of the line upper level population in region  $i$ :

$$\frac{dN_{ui}}{dt} = N_{ui} W_i + \sum_{j=1}^N N_{uj} A_{uj} C_{ji} - N_{ui} (A_{ui} + D_i). \quad (1)$$

The first two terms on the r.h.s. account for local collisional population of the upper level and radiative population of the level by photons emitted from all the cells  $j$  into cell  $i$ , respectively. The final term is the sum of spontaneous and collisional depopulation of the upper level. In this paper, we will confine ourselves to the case where  $dN_{ui}/dt = 0$ , that is, utilization of Eq. (1) to obtain the steady state upper level population in each region, which is equivalent to finding the source function when the lower level population is known. For a large class of problems, such as those treated by Avrett and Hummer,<sup>1</sup> the ground state (lower level)

<sup>†</sup>Science Applications, Inc., McLean, VA 22102, U.S.A.  
<sup>‡</sup>Optical Sciences Division

population is much larger than that of the upper level and the absorption coefficient is known with high accuracy. In these cases, the steady-state version of Eq. (1) requires for its solution the inversion of one  $N \times N$  matrix—to solve  $N$  linear equations in  $N$  unknowns—once the  $C_{ji}$  are calculated from the absorption coefficients. When the absorption coefficient is not known *a priori*, the appropriate version of Eq. (1) must be set up for each level considered and populations for each level must be obtained iteratively using the  $C_{ji}$  calculated from the populations (hence, absorption coefficients) of the previous iteration.

Aside from the atomic constants, calculation of the  $C_{ji}$  from the absorption coefficients to permit solution of Eq. (1) forms the heart of the mathematical problem and is now detailed.

### 3 CALCULATION OF THE COUPLING CONSTANTS

For the case of plane-parallel geometry and Doppler profile with a spatially constant Doppler width, it has proven possible to develop very fast and extremely accurate algorithms for obtaining the  $C_{ji}$ , primarily because of the vast amount of effort by other workers which has been devoted to probability concepts for this case.

Consider a line photon emitted at a point in cell  $j$ , in the direction of cell  $i$ , in the medium. The probability  $P_{ji}$  that the photon is absorbed in cell  $i$  is given by

$$P_{ji} = \bar{P}_e(\tau_{ji}) - \bar{P}_e(\tau_{ji} + \Delta\tau_i). \quad (2)$$

where  $P_e(\tau)$  is the angle-averaged probability that a photon transverses an optical depth  $\tau$  without being absorbed or scattered. In Eq. (2),  $\tau_{ji}$  is the line-center optical depth from cell  $j$  to the boundary of cell  $i$  closest to cell  $j$  and  $\Delta\tau_i$  is the optical depth of cell  $i$  itself. The practicality of the method here described is obviously dependent upon having an efficient technique for obtaining the  $\bar{P}_e$ 's. Holstein<sup>2</sup> obtained an expression for the monodirectional escape probability  $P_e$  valid for completely redistributed Doppler-profile line photons at large optical depths. We have numerically calculated the integral

$$\bar{P}_e(\tau_0) = \int_0^1 P_e\left(\frac{\tau_0}{\mu}\right) d\mu \quad (3)$$

for a large range of optical depths and have adopted the following algorithm to obtain  $\bar{P}_e$  quickly and accurately.

(a) At  $\tau_0 \leq 3$ , a cubic spline polynomial has been fitted to the exact result at 20 points roughly equally spaced from  $\tau_0 = 0$  to  $\tau_0 = 3$ .

(b) For  $\tau_0 > 3$ , the following analytic expression is accurate to better than 7% for  $\tau_0 < 5$  and 4% for  $5 \leq \tau_0 \leq 3 \times 10^4$ :

$$\bar{P}_e(\tau_0) = \frac{0.286}{\tau_0 \sqrt{(\ln(1.95 \tau_0))}}$$

At this point, it should be noted that in calculating the  $C_{ji}$  coupling cells of finite width,  $\bar{P}_e$  must be averaged over the cell originating the photons. This is especially important when the originating and receiving cells are adjacent since  $\bar{P}_e$  can vary by an order of magnitude or more, in some cases, from the front to the back of the originating cell. This averaging process is easily accomplished by analytically integrating the above expressions across the originating cell  $j$  so that

$$C_{ji} = \frac{1}{2(\Delta\tau)_j} \left\{ \int_{\tau_{ji}}^{\tau_{ji} + \Delta\tau_i} \bar{P}_e(\tau) d\tau - \int_{\tau_{ji} - \Delta\tau_i}^{\tau_{ji} + \Delta\tau_i + \Delta\tau_{ji}} \bar{P}_e(\tau) d\tau \right\}. \quad (4)$$

In Eq. (4),  $(\Delta\tau)_j$  and  $(\Delta\tau)_i$  are the line-center perpendicular optical depths of cells  $j$  and  $i$  and  $\tau_{ji}$  is the optical depth between cells  $j$  and  $i$ , measured between the two closest boundaries. The factor of 1/2 in Eq. (4) accounts for the assumed equal probability of photon emission in either direction from cell  $j$ .

## 4. RELATION TO THE EXACT TRANSFER EQUATION

Avrett and Hummer<sup>1</sup> have written the formal solution for the source function  $S(\tau)$  in a plane-parallel atmosphere of optical depth  $T$  as

$$S(\tau) = (1 - P_Q) \int_0^T K_1(t - \tau) S(t) dt + P_Q B, \quad (5)$$

where  $B$  is the Planck function for the local electron temperature,  $P_Q$  is the "quenching parameter", or probability per scattering that the photon is lost from the line and  $K_1$  is the kernel function. In Ref. 1, Avrett and Hummer developed a useful asymptotic expansion for the Doppler kernel function and showed that, for large  $\tau$  (measured at line center),

$$K_1(\tau) \sim \frac{1}{4\tau^2 \sqrt{(\pi \ln \tau)}}. \quad (6)$$

Inspection of Eq. (5) reveals that  $K_1(\tau)$  is the analog of the discrete probability-based coupling coefficients which are used in the present treatment.  $K_1(\tau)$  couples the regions of the medium together and, since the integral is carried out over  $\tau$ , it is, in analogy with Eqs. (1) and (2),

$$K_1(\tau_0) = -\frac{1}{2} \left. \frac{d\bar{P}_e}{d\tau} \right|_{\tau_0}. \quad (7)$$

The rate of change of the angle-averaged escape probability  $\bar{P}_e$  across optical path  $\tau_0$  determines the efficiency with which photons are absorbed per unit optical depth after crossing the path  $\tau_0$ .

The analytic expression

$$\bar{P}_e(\tau_0) = 0.286/\tau_0 \sqrt{[\ln(1.95 \tau_0)]}, \quad (8)$$

which we have used computationally in the calculations presented below should, when differentiated, approach Eq. (7) closely in the limit of large  $\tau$ .

Differentiating Eq. (8) yields, as  $\tau \rightarrow \infty$ ,

$$-\frac{1}{2} \frac{d\bar{P}_e}{d\tau_{\infty}} = \frac{1}{6.993 \tau^2 \sqrt{(\ln \tau)}}, \quad (9)$$

( $\tau$  measured at line center)

which differs by only 1.4% from the exact expression (6). For most cases of interest, nearly all of the coupling occurs within optical depths much smaller than  $3 \times 10^4$ , where Eq. (8) is usually accurate to better than 4%. Also, as seen below, errors of a few per cent in the coupling matrix do not result in large source function errors when the method is applied to specific media of finite optical depth.

## 5 COMPARISON WITH THE TWO-LEVEL-ATOM MODEL

To explore the computational viability of the approach detailed above, we have applied Eq. (1) to a range of plane-parallel media of varying optical depths and quenching parameters. The cases presented in Figs. 1 and 2 reflect comparisons of our approach with exact solutions obtained by Avrett and Hummer.<sup>1</sup> The physical interpretation of the solutions has been thoroughly discussed in Ref. 1 by Avrett and Hummer. Since the media are symmetric about the midplane, the calculation has been set up by establishing 25 or 75 cells in half the medium and coupling each cell "to itself" and to others across the symmetry plane, as well as by direct photon coupling within the same half of the medium. In each case, the cells are spaced logarithmically in optical depth ( $\Delta\tau/\tau \sim \text{constant}$ ) and the optical depths of the cells close to the boundary are less than unity to allow for the anticipated rapid change of the source function

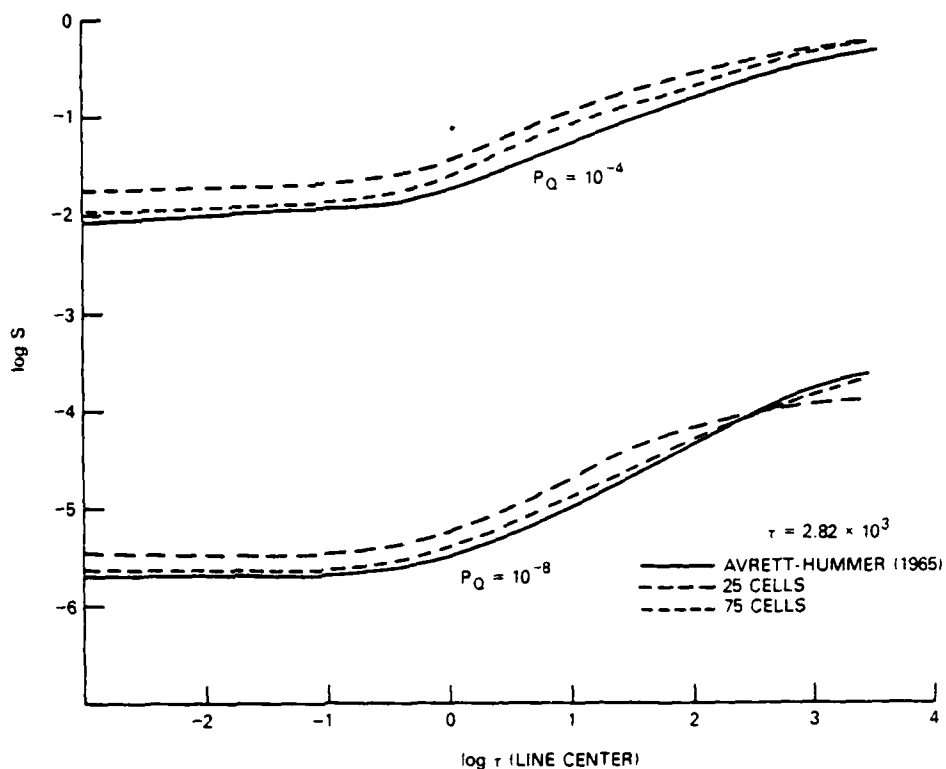


Fig. 1. The steady-state source function for a Doppler profile is shown for an optical depth of  $2.82 \times 10^3$  and a Planck function  $B = 1$ . Results obtained from the present treatment are shown along with the exact solutions obtained by Avrett and Hummer in Ref. 1. The optical depth is measured from the center of the plane-parallel medium to the edge and at line center. Quenching parameters of  $10^{-4}$  (effectively thick) and  $10^{-8}$  (effectively thin) are assumed in the curves shown.

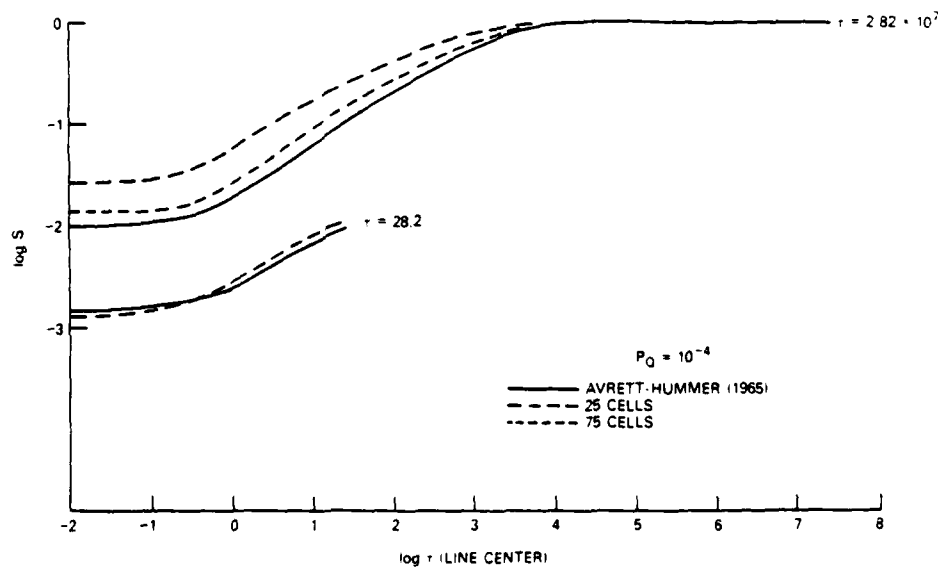


Fig. 2. As in Fig. 1, except that optical depths of 28.2 and  $2.82 \times 10^7$  are shown and only one quenching parameter,  $10^{-4}$ , is considered.

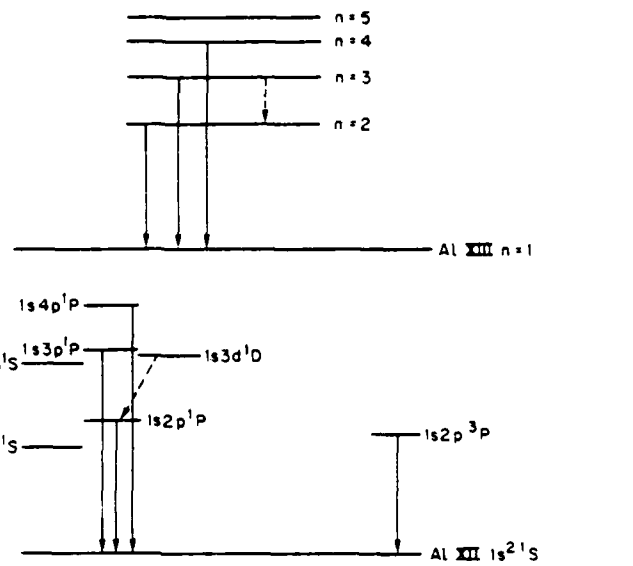


Fig. 3. The excited state structure of the Al (XII) and Al (XIII) species are indicated. Solid arrows illustrate line transported by both direct and probabilistic methods; ---, lines transported using the probabilistic formalism only.

near the edge of the medium. We have also computed results for 50 cells per half-slab, which are not plotted for reasons of clarity.

To obtain solutions within a few per cent of the exact values, only 25 cells need be used for optical depths of  $\sim 10^2$ , but 50–75 cells are necessary at  $\tau \sim 10^4$ . These considerations apply for both the effectively thick and the effectively thin cases. As is seen in Fig. 2, for  $\tau = 2.8 \times 10^7$ , the 25-cell calculation yields source functions a factor of 2.5 greater than the exact solution at small optical depths, but goes to the Planck function ( $B = 1$ ) at the correct optical depth. The 75-cell model yields source functions about 25% too high in the nonthermalized, effectively thin regions at this very high optical depth.

#### 6. APPLICATION TO AN ALUMINUM PLASMA

The method described here appears to hold considerable promise for computationally efficient modeling of laboratory plasmas. Detailed multi-angle, multi-frequency calculations have shown<sup>3</sup> that the ionization dynamics and energetics of high-temperature plasmas are significantly affected by the trapping of line and continuum radiation. Accurate simulation of such plasmas and computation of diagnostically useful line ratios requires that all optically thick lines be transported. Given these considerations, we have applied the method to determine the state of an optically thick aluminum plasma in collisional-radiative equilibrium. Specifically, we have chosen a planar plasma at a temperature of 600 eV, with a half-width of  $750 \mu$  and a total ion density of  $1 \times 10^{19}$  ions per  $\text{cm}^3$ . As a framework within which the technique is applied, we have used the multistage, multilevel aluminum model, which has been extensively described elsewhere.<sup>4</sup> The accompanying energy level diagram (Fig. 3) indicates the excited state structure and transported lines of the Al (XII) and Al (XIII) stages, which are dominant at our chosen temperature and density.<sup>†</sup> Additionally, the Al (XI)  $1s^2s-2p, -3s, -3p, -3d, -4d$ , and  $1s2p^2$  excited states are included, with transport of the satellite line  $1s^2p^2P - 1s2p^2D$ . This model has been extensively applied using direct methods to solve the radiative transport equation and the results will be thoroughly described for a range of plasma conditions in an upcoming paper. The salient features of the results for this particular plasma are now described in the separate sections below.

<sup>†</sup>In these calculations, photoionization has been neglected, as have radiative recombination transitions except for those onto the bare proton to form  $H\ n = 1$  and  $n = 2$ , onto  $H\ n = 1$  to form He  $1s^2S$  and  $1s2p^1P$ , and onto He  $1s^2S$  to form Li  $1s^2S$ .

(a) *Comparison of Voigt and Doppler profiles*

We have performed a separate calculation for the identical plasma directly solving the transport equation with Voigt profiles for each line whose widths are determined by the total lifetime of the respective upper levels. The calculation revealed very little difference in state populations from that observed using a pure Doppler profile. At this density and size, therefore, a Doppler profile is an adequate representation of the line opacity of the plasma. At higher ion densities, the increased wings of the Voigt profile coupled with higher optical depths causes a significant lowering of the excited state densities compared to that obtained with a Doppler profile.<sup>5</sup>

(b) *Effect of photon pumping*

The effects of radiative pumping of the excited states on the overall state of the plasma are perceived most readily by solving for the plasma state *ignoring* radiative transfer, that is, assuming that lines which are really optically thick are instead thin. This is done in our calculation as a means of providing an initial guess as a basis for iteration to the true optically thick state. In Figs. 4 and 5, we have plotted the level densities as a function of  $z$  for helium-like (XII) and hydrogen-like (XIII) aluminum, respectively. Both the assumed thin and true optically thick solutions are shown. The most obvious feature of Figs. 4 and 5 is that the excited state densities are raised well above their optically thin values by repeated line photon scatterings (re-excitations of the level). Relative to the ground state densities, the Al (XII)  $1s2p^1P$  population at plasma center is increased by a factor of 170 and that of the Al (XIII)  $n = 2$  state is raised by a factor of 68. These values are in reasonable agreement with the

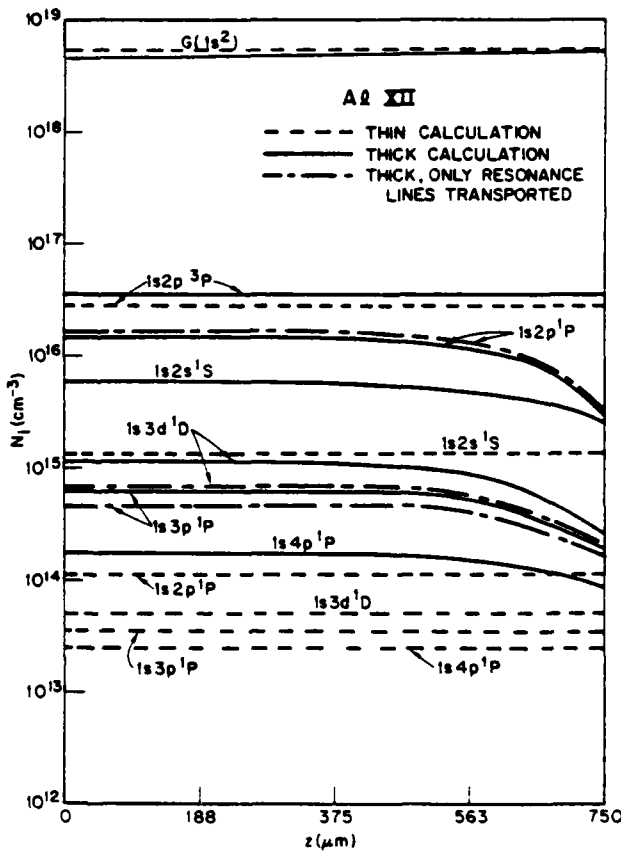


Fig. 4. Excited and ground state densities of Al (XII) are shown as functions of position in the plasma. Results are given for both thin (ignoring radiative transfer) and thick calculations. Also plotted are densities obtained when transport of excited state lines is neglected, when such densities differ appreciably from those of the full calculation.

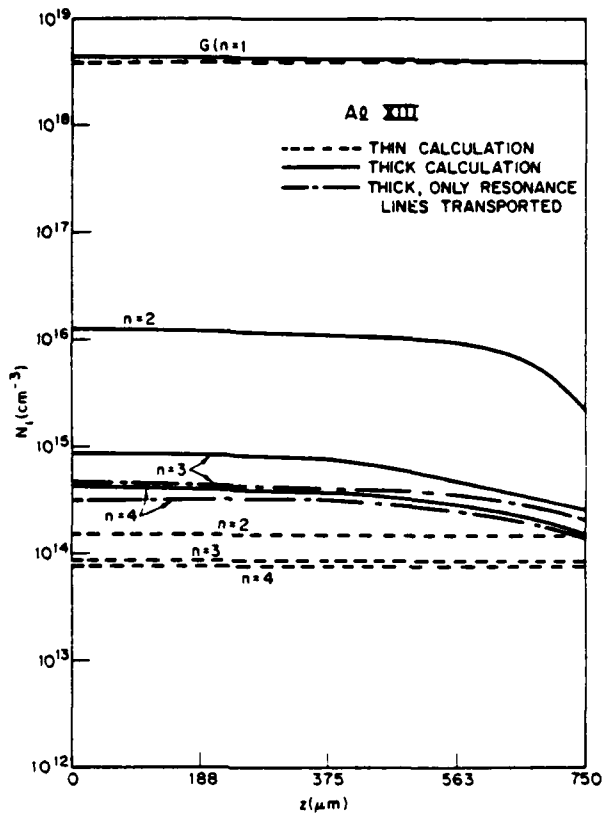


Fig. 5. As in Fig. 4, except that Al (XIII) is shown.

Table I. Table of line power outputs (W/cm<sup>3</sup>).

Al XIII			
Line	Thin lines (no transport)	Thick lines; only resonance lines are transported	Full transport
1-2	$5.87 \times 10^{11}$	$5.25 \times 10^{11}$	$7.12 \times 10^{11}$
1-5	$4.54 \times 10^{10}$	$2.36 \times 10^{10}$	$4.09 \times 10^{10}$
1-4	$1.00 \times 10^{10}$	$1.05 \times 10^{10}$	$1.20 \times 10^{10}$
2-3	$5.71 \times 10^3$	$2.59 \times 10^{10}$	$3.41 \times 10^{10}$

Al XII			
$1s^2 - 1s2p^5P$	$1.02 \times 10^{11}$	$1.74 \times 10^{11}$	$1.71 \times 10^{11}$
$1s^2 - 1s2p^1P$	$7.33 \times 10^{11}$	$4.34 \times 10^{11}$	$5.74 \times 10^{11}$
$1s^2 - 1s3p^1P$	$2.12 \times 10^{10}$	$4.12 \times 10^{10}$	$5.42 \times 10^{10}$
$1s^2 - 1s3p^1D$	$2.54 \times 10^{10}$	$1.35 \times 10^{10}$	$2.75 \times 10^{10}$
$1s2p^1P - 1s3d^1D$	$2.90 \times 10^3$	$2.06 \times 10^{10}$	$2.27 \times 10^{10}$

enhancement of excited state populations predicted by photon-escape theory arguments.<sup>6</sup> The table of line power outputs reveals that, at our chosen density of  $1 \times 10^{19}$ , the Al (XII)  $1s^2 - 1s2p^1P$  line, for instance, is effectively thin. That is, even though the line center optical depth happens to be 50 in this case, the emergent power is attenuated only slightly from the optically thin value. Most of the line photons, therefore, escape the plasma after many scatterings. For the effectively thin case,  $N_s$ , the number of scatterings, is equal to  $P_e^{-1}$ , where  $P_e$  is the mean photon escape probability for the plasma. To produce 170 scatterings for this line requires a  $P_e$  of about 1/170 or, as revealed by Eq. (3) and the subsequent approximate expressions, an optical depth of 25. This optical depth is exactly halfway between the surface and center of the plasma, confirming the usefulness of the mean escape probability concept. Similarly, good agreement is seen for the  $1 \rightarrow 2$  line of Al (XIII).

Figures 4 and 5 also illustrate spatial gradients in certain of the excited states of this plasma, which is of course of uniform temperature and total ion density. The gradients appear in the excited states which are controlled primarily by radiative pumping. This pumping occurs either directly to the excited state in question or to an adjoining state which is strongly collisionally coupled to the state. The  $1s2p^3P$  state of Al (XII) is so strongly controlled by collisions that no significant spatial gradient appears. The gradients in the radiatively-controlled excited states are a result of the lack of pumping radiation incident on the outer edge of the plasma. This results in a lowered excited state density at the outer boundary, hence a lowered inward line photon flux emitted near the outer boundary. The interior of the plasma ( $\tau \gg 1$ ) can thus sense the boundary of the plasma and the result is the spatial profiles of Figs. 4 and 5. These effects have been discussed in detail elsewhere.<sup>7,8</sup>

#### (c) Effects of excited state-to-excited state photo-pumping.

Also indicated in the power output table and plotted in Figs. 4 and 5 are the effects of photon-pumping by lines connecting excited states. This is of particular interest since the transport of such lines is usually neglected. The optical depths of such lines are strongly dependent on photon pumping of their lower levels from the ground state. Thus, they are not easily estimable and may vary extremely sensitively with temperature, density and plasma size. We plan a detailed study of these effects, which will be subsequently reported. We confine our remarks here to the specific plasma discussed above. In the particular plasma under consideration, the Al (XII)  $1s2p^1P - 1s3d^1D$  and Al (XIII)  $n = 2 \rightarrow n = 3$  lines are the only excited state lines with appreciable optical depths (0.61 and 0.38 at line center, respectively). The principal effect of neglecting transport of these lines is to underestimate, by about a factor of 2, the populations of the Al (XIII)  $n = 3$  and Al (XII)  $1s3d^1D$  states. The  $n = 2$  level populations, which depend primarily on pumping from the ground state, are not significantly affected. Nor are the  $n = 4$  levels substantially increased, since lines arising from  $n = 2$  and  $n = 3$  pumping  $n = 4$  are optically thin in both species. The optical depths of the above mentioned  $2 \rightarrow 3$  lines imply that about one scattering will follow collisional excitation of the lines, resulting in the doubling of the upper level populations when the transport effect is accounted for. The power output of the Al (XIII)  $1 \rightarrow 3$  line increases by 43%, rather than doubling, because near the surface of the plasma the  $n = 3$  level's population only increases by 25%, since the pumping effects are not as large at the boundary. The level populations near the plasma edge are, of course, more important than those in the interior in determining power output. The calculated outputs of the  $2 \rightarrow 3$  lines in both Al (XII) and Al (XIII) decrease when the lines are transported because of reabsorption and quenching. The optically thick calculation, however, yields a vastly greater output in these  $2 \rightarrow 3$  lines than that obtained when all lines (including resonance lines) are assumed thin. This is, of course, due to resonance pumping of the  $n = 3$  level. It is thus seen that two-level-atom scattering theory<sup>6</sup> gives good results for  $1 \rightarrow 2$  and  $1 \rightarrow 4$  lines in this specific case but that the  $1 \rightarrow 3$  line in Al (XIII) is significantly altered in output by radiative pumping from  $n = 2$ .

#### (d) Advantages and limitations of the formalism

No significant differences were observed in the results obtained using conventional multi-frequency, multiangle transport compared to those yielded by the present method. Since our formalism eliminates frequency- and angle-integration, it is quite advantageous numerically. A

further advantage of the coupling constant technique was achieved specifically in its use in a multistage, multilevel model. As the excited state densities build up during the "time-stepping" iteration scheme,<sup>9</sup> the ground states change very little over 5-10 steps. Thus, the coupling constants, which depend on the ground state densities *only* for the thick resonance lines, need be updated for these lines (the vast majority of lines transported) only every 5-10 steps.

Two major limitations affect the application of the present scheme. First, efficient numerical algorithms for the cell-to-cell coupling constants have been obtained only for the case of a spatially constant line Doppler width. It is far from obvious that similar algorithms can be obtained to apply to the general case, where gradients of varying magnitudes and directions are conceivable. Second, the emitted radiation cannot be resolved in angle. This second limitation can be mitigated for the steady state case by using a detailed multi-ray procedure to compute the angular distribution of radiation once the excited state densities are determined by the more efficient coupling method. However, for a time dependent calculation calling a ray-tracing scheme every timestep to obtain angular resolution would clearly be as expensive as using the multi-frequency, multi-angle technique to directly compute the state of the plasma.

#### SUMMARY AND CONCLUSIONS

An efficient and readily adaptable technique for radiative transfer calculations has been developed which eliminates the need for angle-and-frequency integrations. A specific numerical algorithm has been developed for a Doppler profile in plane-parallel geometry and applied in a detailed analysis of multilevel coupling in a highly ionized aluminum plasma. Extension of the method to other geometries and line profiles (e.g. Voigt profiles) can be achieved by obtaining expressions for cell-to-cell photon escape and absorption probabilities for these cases. The numerical consequences of this additional physics will appear solely in the use of different coupling coefficients. Use of the technique has made possible calculations which have revealed in detail the effects of excited-state-line transport on line power outputs and level populations in an aluminum plasma. In addition, the uses and limitations of an even simpler one-cell scattering theory approach have been assessed.

*Note added in proof:* The 20-point cubic spline fit to  $\tilde{P}_c(\tau_0)$  for  $\tau_0 \leq 3$  is extremely accurate for both  $\tilde{P}_c$  and its gradient. However, a somewhat less time-consuming approximation to  $\tilde{P}_c(\tau_0)$  for  $\tau_0 \leq 3$  is given by

$$\tilde{P}_c(\tau_0) = \frac{1}{1 + 1.861607\tau_0 - 0.817393\tau_0^2}$$

This expression differs from the exact  $P_c$  by a maximum of 7% for  $0 \leq \tau_0 \leq 3$ . The gradient of  $\tilde{P}_c$ , however, is not well represented for  $\tau_0 \leq 0.5$ . Despite this fact, use of the above simplified expression yields results which are everywhere within a few per cent of the 20-point spline results for the Avrett-Hummer cases which are illustrated in Figs. 1 and 2. Both the above expression and the one given for  $\tau > 3$  in Section 3 are analytically integrable for use in Eq. (4), and are equal at the joining point  $\tau_0 = 3$  to several significant figures.

*Acknowledgement*—This work was supported in part by the Defense Nuclear Agency.

#### REFERENCES

1. E. H. Avrett and D. G. Hummer, *MNRAS* **130**, 295 (1965).
2. T. Holstein, *Phys. Rev.* **72**, 1212 (1947).
3. J. Davis, K. G. Whitney, and J. P. Apruzese, *JQSRT* **20**, 353 (1978).
4. J. Davis, and K. G. Whitney, *J. Appl. Phys.* **47**, 1426 (1976).
5. J. P. Apruzese, J. Davis, and K. G. Whitney, *JQSRT* **17**, 557 (1977).
6. J. P. Apruzese, J. Davis, and K. G. Whitney, *J. Phys. B* **11**, L643 (1978).
7. J. P. Apruzese, J. Davis, and K. G. Whitney, *J. Appl. Phys.* **47**, 4433 (1976).
8. J. P. Apruzese, J. Davis, and K. G. Whitney, *J. Appl. Phys.* **48**, 667 (1977).
9. K. G. Whitney, J. Davis, and J. P. Apruzese, *Cooperative Effects in Matter and Radiation* (Edited by C. M. Bowden, D. W. Howgate, and H. R. Robl), p. 115. Plenum Press, New York (1977).